Microsystem Design and Package Integration Concepts for Pipeline and Downhole Monitoring

by

Neeharika Vellaluru

A dissertation submitted in partial fulfillment
of the requirements for the degree of
Doctor of Philosophy
(Electrical and Computer Engineering)
in the University of Michigan
2020

Doctoral Committee:

Professor Yogesh B. Gianchandani, Co-Chair
Associate Professor Tao Li, Co-Chair
Professor Wei Lu
Associate Professor Becky Peterson

सिद्धिर्भवति कर्मजा

Neeharika Vellaluru

vneehu@umich.edu

ORCID iD: 0000-0003-0041-3430

© Neeharika Vellaluru 2020

To

My dear parents, for their unconditional love and support

and to

all my teachers from grade school to grad school

ACKNOWLEDGEMENTS

I would like to acknowledge my research advisor, Professor Yogesh Gianchandani for his support and guidance throughout my doctoral study at the University of Michigan, Ann Arbor. I thank him for providing me with the opportunity to work on interesting projects and driving me towards achieving excellence. I am grateful to my co-advisor, Professor Tao Li for his enthusiasm in sharing his knowledge and expertise, and for his constant guidance and encouragement over the many years. I would also like to acknowledge the other committee members, Prof. Wei Lu and Prof. Becky Peterson, for their constructive comments and valuable suggestions for this dissertation.

Some fabrication and characterization work described in this dissertation was performed at the Lurie Nanofabrication Facility (LNF) operated by the Solid-State Electronics Laboratory (SSEL) at the University of Michigan. The pressure sensors and the packaging effort in this work were developed and led by Dr. Alexander Benken. The research inputs provided by him have been of immense help to me. The software in this research was partially developed by Mr. Partha Dutta. The field tests were performed by researchers from Total (Pau, France) in the Democratic Republic of Congo (Africa). I sincerely appreciate all the researchers involved for their assistance in these tests. I would also like to thank all the staff members at the University of Michigan, whose timely help made my research progress smoothly.

Over the course of my studies at the University of Michigan, I had the pleasure of having great friends and colleagues. I would like to extend my gratitude to former and current members of Prof. Gianchandani's research group – Alex, Andy, Daniel, Declan, Jiqing, Johnny, Leo, Partha, Qisen, Ramprasad, Scott, Shiang, Tsenguun, Venkat, Weilin, Yu, Yushu, Yutao, Zeyu, and others. I would also like to express my sincere thanks to my friends – Krupa, Mahesh, Kiran, Bhavana, Isha, Neha, Sajal, Pallav, Mayur, and many others. Their warm encouragement and support helped me get through many difficult times in my Ph.D. journey.

The support of my parents, Mr. V. Venkatesh and Mrs. V. Sharada has been the driving force behind my quest for knowledge. I sincerely thank them for encouraging me to reach every milestone in my life. I am thankful for the love and support of my husband Santosh, through all the trying and happy times. I am looking forward to his company in this journey of life.

TABLE OF CONTENTS

Dedication ii
Acknowledgements iii
List of Figures vii
List of Tables x
Abstract xii

Chapter 1: Introduction 1
1.1 Background and Motivation 1
1.2 Existing Microbattery Designs and Wireless Power Transfer Methods 6
1.3 Wireless Communication Methods for Microsystems 12
1.4 Requirements of System Integration and Packaging 13
1.5 Previous Generations of Environmental Loggig Microsystem (ELM) 16
1.6 Goals, Tasks, and Challenges 17
1.7 Organization of Dissertation 20

Chapter 2: Environmental Logging Microsystem for Pipeline Monitoring 22
2.1 System Hardware 24
2.2 System Software 33
2.3 System Integration and Fabrication 45
2.4 Experimental Results 49
2.5 Discussion and Summary 58

Chapter 3: Environmental Logging Microsystem for Downhole Monitoring 60
3.1 System Hardware 62
3.2 System Software 66
3.3 System Integration and Fabrication 71
3.4 Experimental Results 75
3.5 Discussion and Summary 78

Chapter 4: Flow-Compatible Package for ELM for Downhole Monitoring 80
4.1 Package Design and Fabrication 82
4.2 Packaged ELM Test Results 84
4.3 Discussion and Summary 89

Chapter 5: High Capacity Rechargeable Nickel-Zinc Microbatteries 91
5.1 Nickel-Zinc Battery Chemistry 93
5.2 Microbattery Design 94
5.3 Microbattery Fabrication 95
5.4 Experimental Results 99
5.5 Discussion and Summary 102

Chapter 6: Conclusions and Future Work 105
6.1 Summary and Major Contributions 105
6.2 Future Work 110

Appendix A 113
References 116

LIST OF FIGURES

Figure 1.1: Schematic of a typical autonomous microsystem……………………………………. 1

Figure 1.2: Deployment of smart pig in a pipeline [Mar15]………………………………………4

Figure 1.3: Deployment of autonomous microsystems in a wellbore [Sui17]…………………… 5

Figure 1.4: Ragone plot indicating the various power technologies (adapted from [Pik13])……..7

Figure 1.5: Microbattery design. Nickel scaffold was used as the current collector (blue). Manganese oxide was used as the cathode (red) and lithium as the anode (yellow) [Pik13]……..8

Figure 1.6: Packaged system (a) ELM1; (b) ELM2; and (c) ELM3 [Ma16, Sui17]……………. 16

Figure 2.1: ELM6 block diagram…………………………………………………………...25

Figure 2.2: Circuit schematic for ELM6………………………………………………………26

Figure 2.3: Transmitter and receiver kits for wireless power transfer [STM17]………………...28

Figure 2.4: Optical image of the pressure sensor…………………………………………...32

Figure 2.5: Overall system representation for ELM6…………………………………………33

Figure 2.6: Bluetooth external unit hardware [Ras20]………………………………………...33

Figure 2.7: Typical operation flowchart for ELM6……………………………………………... 34

Figure 2.8: S-MCU state diagram for ELM6…………………………………………………35

Figure 2.9: Diagram of sub-states for state A5, detection state………………………………….37

Figure 2.10: B-MCU State Diagram for ELM6…………………………………………………39

Figure 2.11: Graphical user interface of Bluetooth external unit……………………………….. 44

Figure 2.12: Screenshot of interface during communication with ELM6. (a) The serial number of the system along with BLE connection status and system message are displayed in Section (2). (b) The list of available BLE devices nearby is displayed after scanning; unrecognized devices are displayed as "None"……………………………………………………………………45

Figure 2.13: Layout of the foldable polyimide PCB (L×W: 43.0 mm ×14.2 mm)………………46

Figure 2.14: (a) Design of flexible PCB stack; (b) folded ELM2 PCB packaged in ceramic tube [Ma16]; (c) unfolded ELM3 PCB packaged in polymer mold [Sui17]…………………………47

Figure 2.15: Photos of the manufactured ELM6 flexible PCB: (a) top and (b) bottom view…... 48

Figure 2.16: ELM6 battery charging (a) circuit and (b) OCV plot………………………………51

Figure 2.17: (a) Transient current consumption of B-MCU during BLE operation (b) Transient current measurement circuit (c) Magnified view during BLE advertising (View 1) (d) Magnified view during BLE handshaking (e) Magnified view during BLE data transfer (View 3)……….. 53

Figure 2.18: (a) Temperature (ELM Temperature) and capacitance (Pressure Sensor and Ref Cap); (b) Acceleration; and (c) Magnetic field data recorded by ELM6 during the room temperature test…………………………………………………………………………..54

Figure 2.19: (a) Temperature and capacitance; (b) Acceleration; and (c) Magnetic field data recorded by ELM6 during the system lifetime test……………………………………………55

Figure 2.20: (a) Temperature (ELM Temperature) and capacitance (Pressure Sensor and Ref Cap) data recorded by ELM6 during pressure test; (b) temperature data and interpreted pressure data recorded by ELM6, and the tool pressure data during pressure test……………………….. 56

Figure 2.21: Temperature data recorded by ELM6 during HT test…………………………... 57

Figure 2.22: (a) Temperature (ELM Temperature) and capacitance (Pressure Sensor and Ref Cap) data recorded by ELM6; (b) temperature data recorded by ELM, interpreted pressure data recorded by ELM, and the tool pressure data…………………………………………………… 58

Figure 3.1: ELM7 block diagram……………………………………………………………...62

Figure 3.2: The circuit schematic of ELM7…………………………………………………...63

Figure 3.3: (a) Transmitter kit and (b) receiver coil and chip for wireless charging of ELM7…. 64

Figure 3.4: Tadiran Model TLI-1020A packaged with quick connect connector………………. 65

Figure 3.5: Typical operational flowchart for ELM7…………………………………………… 66

Figure 3.6: ELM7 state machine diagram……………………………………………………… 67

Figure 3.7: Diagram of sub-states for state 10, detection state…………………………………. 69

Figure 3.8: Graphical user interface of Bluetooth external unit………………………………… 70

Figure 3.9: Screenshot of interface during communication with ELM7. (a) The serial number of the system along with BLE connection status and system message are displayed in Section (2). (b) The list of available BLE devices nearby is displayed after scanning; unrecognized devices are displayed as “None”…………………………………………………………………….71

Figure 3.10: Layout of the ELM7 PCB (diameter: 26.7 mm)…………………………………... 72

Figure 3.11: Photos of the manufactured ELM7 PCB: (a) top and (b) bottom view…………….72

Figure 3.12: Photo of TLI-1020A battery connected to ELM7 PCB…………………………… 74

Figure 3.13: ELM7 battery charging (a) circuit and (b) OCV plot………………………………76

Figure 3.14: Detection mode current variation with temperature……………………………...76

Figure 3.15: Temperature data recorded by the full ELM7 system……………………………...77

Figure 3.16: Temperature data recorded by ELM7 with battery at room temperature…………..77

Figure 4.1: Design of ELM7 molded Viton package with system components………………… 83

Figure 4.2: Photos of (a) injection molded Viton domed cylindrical tube and tube cap; (b) ELM7 PCB and battery secured inside a high temperature thermoplastic bag filled with non-conductive oil; (c) fully packaged ELM7 systems………………………………………………………….. 84

Figure 4.3: Laboratory testing of fully packaged ELM7 system at HPHT for (a) 96-hour duration, (b) enhanced view of full test at maximum pressure and temperature, and (c) enhanced view of test showing interpreted microsystem pressure using calibration equation as given in (4.1)…... 86

Figure 4.4: Photos of a packaged microsystem inside a wireline basket captured by Total S.A. during field tests in an operational oil well and fully packaged microsystems (inset)…………. 87

Figure 4.5: Results from downhole functional oil well test. (a) Capacitance (C_P and C_R) and temperature (T_{sys}) recorded by the system. (b) Pressure (P_{tool}) and temperature (T_{tool}) reported by a commercial pressure and temperature gauge at a well depth of 1290 m, and the interpreted pressure (P_{sys}) and system temperature (T_{sys}) based on data recorded by the system……………88

Figure 4.6: Results from downhole functional oil well test. (a) Acceleration and (b) Magnetic field in X, Y, and Z axes data recorded by the system………………………………………….. 88

Figure 5.1: Representation of Ni-Zn battery reactions………………………………………….. 94

Figure 5.2: Design of microbattery for batch mode fabrication (3×3 array illustrated)………… 95

Figure 5.3: Fabrication process flow for an array of Ni-Zn microbatteries…………………….. 96

Figure 5.4: Photos of (a) µEDM cavities in Ni foil (b) µEDM recesses in Zn foil……………... 97

Figure 5.5: Photo of perforations in acrylic adhesive tape……………………………………… 98

Figure 5.6: Photo of an array of fabricated microbatteries after singulation…………………….99

Figure 5.7: Measured capacity by cycle number for three different battery samples…………..100

Figure 5.8: Measured charge/discharge curves for the 6th cycle of B2 tested immediately after fabrication……………………………………………………………………………………… 101

Figure 5.9: Discharge voltage curves at various discharge currents……………………………101

Figure 6.1: (a) Overall package design including batteries, connector foils, and 3D printed shell. (b) Top-down view of the overall package…………………………………………………..112

Figure 6.2: (a) Model of the 3D printed package shell; (b) cut-off view (AA') indicating the design features in the 3D printed package shell……………………………………………….. 112

Figure A.1: Schematic drawing of the basic setup of µEDM unit [Tak02]…………………….114

List of Tables

Table 1.1: Comparison of various wireless power transfer methods [Lu16] 11
Table 1.2: Comparison of communication methods [Sui17]...13
Table 1.3: Summary of previous generations of ELM [Sui17] 17
Table 1.4: Design targets of this dissertation 19
Table 2.1: Major system components 26
Table 2.2: Comparison of MCUs for S-MCU 29
Table 2.3: Comparison of MCUs for B-MCU...30
Table 2.4: B-MCU energy modes, current consumption, and functions....................................30
Table 2.5: Comparison of communication protocols...31
Table 2.6: List of sections with their functions on the GUI 45
Table 2.7: Major components of ELM6 flexible PCB 48
Table 2.8: Overall design parameters of ELM6 49
Table 3.1: Major system components 63
Table 3.2: List of sections with their functions on the GUI 70
Table 3.3: Major components of ELM7 PCB...73
Table 3.4: Overall design parameters of ELM7 74
Table 4.1: Size and density information of ELM7 packaged system components.......................83
Table 4.2: Design and performance parameters of the ELM7 system..89
Table 5.1: Design Specifications of Ni-Zn microbatteries...95
Table 5.2: Specifications of Ni-Zn microbatteries..102
Table 5.3: Comparison of this work with other published work on Ni-Zn microbatteries in literature...103
Table 6.1: Summary of all the generations of ELM 108

ABSTRACT

Autonomous microsystems capable of sensing temperature, pressure, and inertial parameters are needed for many applications, including pipeline integrity monitoring and data collection in downhole environments for oil and gas exploration. A representative microsystem is comprised of sensing elements, micro-controller and interface electronics, communication module, a power source, power management and charging elements, and package. Small diameter pipelines limit microsystem size to centimeter scale and consequently limit available volume for power sources, necessitating low power consumption and compact system design with fully integrated sensing functionality. High temperature and pressure downhole environments cause numerous challenges in microsystem design, requiring that all system components be designed in tandem to operate seamlessly together. Two of the most critical microsystem aspects are the power source and system package, as these are shared resources for other components such as communication, control, and sensing.

This dissertation focuses on investigating critical elements of system design and package integration for environmental sensing autonomous microsystems, specifically for pipeline monitoring and downhole monitoring applications. The research goals are to investigate 1) system level design compromises, relationships between the building blocks, and overall performance limits under deployment conditions – including those at elevated temperatures and pressures, 2) an integration approach within a package that permits deployment, retrieval, and reusability of downhole sensing systems, and 3) a scalable fabrication method for incorporating microbatteries within autonomous microsystems.

System level design compromises and overall performance limits were investigated for environmental logging microsystems (ELM6 and ELM7) for pipeline and downhole monitoring, respectively. The systems used resonant inductive charging and Bluetooth low energy (BLE) protocol for communication. They were designed to accommodate up to 70 MPa pressure. The ELM6 had a standby current of 8 µA at room temperature (RT) which permitted a lifetime of 10 days using a 9 mAh lithium ion microbattery.

The ELM7 microsystem was intended for downhole monitoring at temperatures and pressures up to 85°C and 35 MPa, while maintaining an overall volume of <25 cm^3 and density <1.2 g/cc. The package integration approach must protect the electronics from the harsh environment while permitting transfer of external pressure and temperature to the sensors during deployments; between deployments it must allow wireless charging and wireless communication, and in certain situations it must also allow the removal of the package and reusability of the system hardware. The ELM7 was successfully tested up to 85°C at pressures up to 41.5 MPa and up to 160°C for all elements excluding the battery in laboratory conditions. Field trials of these packaged systems were successfully completed by repeated deployment in an operational oil well to a depth of 1,290 m, during which data was successfully logged.

A scalable fabrication method for rechargeable nickel-zinc micro batteries was demonstrated. The fabricated batteries had a footprint of ≈0.048 cm^2, nominal voltage of 1.7 V, and energy density of 2.28 mWh/cm^2.

Systems capable of sensing temperature, pressure, and inertial data, permitting resonant inductive charging and BLE communication, and consuming low power within a small form factor for pipeline and downhole monitoring applications were successfully investigated, designed, and demonstrated in both laboratory and field conditions.

CHAPTER 1: Introduction

1.1 Background and Motivation

Microsystems are miniaturized functional systems that consist of integrated microsensors and microactuators based on micro electromechanical systems (MEMS) technology, interface microelectronics, and packaging technologies [Gia07]. Small size, diverse functionality, and low cost are the prominent advantages of microsystems, enabling their applications in medical, consumer, industrial, and environmental monitoring [Gia07, Tum01, War01, Wis09].

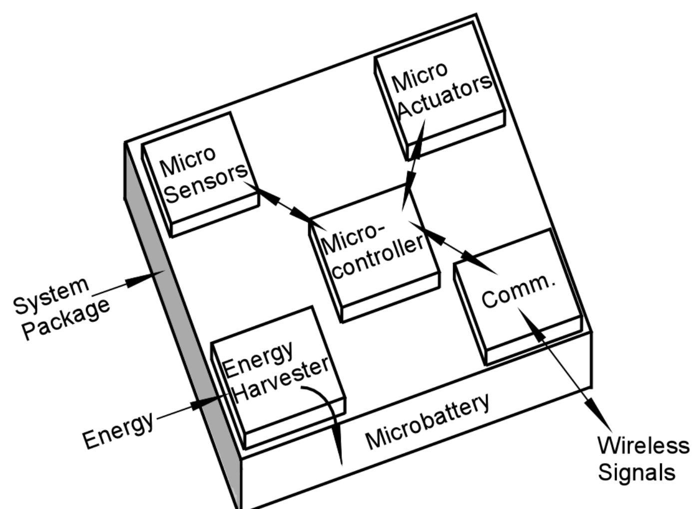

Figure 1.1: Schematic of a typical autonomous microsystem.

A typical microsystem consists of MEMS sensors and/or actuators, a micro-controller, a communication module, a power source module, and system package (Figure 1.1). A critical aspect of the autonomous microsystem architecture is wireless communication. Wireless interrogation is the preferred method of data retrieval to preserve packaging integrity. RF communication is a common method [Cho17, Smi07, Sus05], as well as optical communication [Cho17]. RF communication is preferred over optical as it is not limited by line of sight and

low-power radio transceivers are available with data-rates and ranges scalable according to the application. The system package provides physical, mechanical, and chemical protection from the target environment. In addition, it also contains elements specific to the application to enable the interaction of the microsystem components with the environment through mechanical, electrical, thermal, chemical or optical interfaces. The power source module is used to power the entire microsystem. It consists of a battery and an optional energy harvester. The battery can be primary or secondary depending on the application. Typical operation of the battery in a microsystem is to provide energy over short periods of time when needed, such as during sensing or RF communication. For most applications, it may be necessary to recharge the system battery when long term operation is required [Fai16]. In these cases, an energy harvester is necessary to recharge the battery. *The environment generally has the greatest impact through the power source and encapsulation of the microsystem, as these are shared resources for other microsystem blocks like communication, control, and sensing*.

Autonomous microsystems are designed to be deployed in an environment of interest for data collection. One area of active interest is pipeline integrity monitoring along its length. Another important role for these systems is in downhole monitoring for oil extraction and production. By injecting these systems into the boreholes and hydraulic fractures and then retrieving them after a certain length of time, geophysical conditions in the area of interest can be obtained. Challenges in system design include potentially high environmental temperature and pressure, a miniaturized size, and robust packaging.

This work focuses on investigating critical elements of system design and package integration for environmental sensing autonomous microsystems, specifically for pipeline monitoring and downhole monitoring applications.

1.1.1 Pipeline Monitoring Applications

Pipeline systems are responsible for transporting vital materials such as water, oil, gas etc. They are the most economical and practical transportation method with oil pipelines transporting roughly two-thirds of the petroleum shipped in the United States [Tre01]. Pipelines are subject to several degradation factors, including construction defects, aging-related issues, and environment related threats [Can15]. Leakage of oil and gas from pipelines can not only cause significant economic losses but also pose a significant threat to the environment and life. Therefore, it is of great importance that effective pipeline integrity management methods be implemented to prevent such accidents.

Leaks alter the normal pressure in the pipe; therefore, monitoring internal pipe pressure can potentially help identify the leak [Sad14]. A slow leak changes its surrounding temperature profile and might not have a major effect on the internal pressure of the pipe. Hence temperature measurements of a pipe can also provide useful data in pipeline monitoring. It is also necessary to know the exact location of the leak and inertial sensors are useful for this purpose. There are multiple methods used to detect and locate leaks in pipelines [Liu12]. Pure Technologies Ltd. have developed a free-swimming spherical device called SmartBall™ to detect and locate leaks; however, they have an exterior diameter of >Φ100 mm, rendering them unsuitable for small diameter pipelines [Fle08].

Smart pipeline inspection gauges, referred to as 'smart pigs', are commonly used to inspect a pipeline (Figure 1.2). They consist of various sensors, electronics and control circuitry, and power source and their size may vary based on the diameter of the pipeline [Kup05]. Depending on the sensors employed, they are used to gather various types of information in the pipeline such as temperature, pressure, pipe corrosion/metal loss, cracks, leaks, diameter, bends, and curvature [Can15]. They are designed to travel in the interior of the pipeline, usually while the line is in

service. Smart pigs are not suitable for pipelines with a diameter of less than 2 inches (5.08 cm) [Fle15]. Another drawback is the risk of pigs becoming lodged in the pipeline, which can interrupt or stop product flow [Fun06]. Microsystems capable of sensing pressure, temperature, and inertial parameters can be incorporated into smart pigs or used independently.

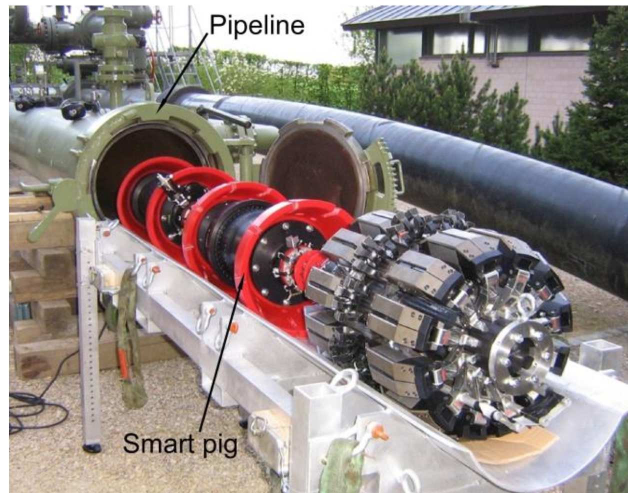

Figure 1.2: Deployment of smart pig in a pipeline [Mar15].

1.1.2 Downhole Monitoring Applications

Application of autonomous microsystems are of commercial interest for use in oil and gas exploration. In hydrofracturing processes, acquisition of well monitoring data such as temperature, pressure, resistivity, and chemical concentration are necessary for increasing well efficiency, extending well life, increasing safety, and lowering the operational cost [Cha12, Fin10, Wod11, Yu12]. Traditional means of well monitoring involve long, electrically conductive cables which are lowered into the wellbore (called wireline monitoring) [Ell07]. Despite widespread use in the oil and gas industry, wireline monitoring data can only be collected near the wireline in the vertical segment of the wellbore. This leaves a need for data collection in horizontal wellbores and fractures, as well as deep into the reservoir.

Autonomous microsystems have no need for cable tethers, providing a distinct advantage in being able to collect data throughout the entire wellbore and show a promising trend in

miniaturization to eventually provide data from directly inside fractures. Figure 1.3 illustrates a potential application scenario in which a large number of autonomous microsystems can be flowed into the wellbore using a fluid medium. There has been very limited work reported on microsystems for downhole environmental monitoring. The University of Tulsa and Saudi Aramco have developed a research prototype using customized electronic chips encapsulated in a Φ7.5 mm polymer sphere to monitor temperature and pressure in downhole environments [Yu12, Shi15]. The system was successfully operated in a wellbore for 1 hour at temperature up to 88°C and pressure up to 50 MPa. However, its small size may limit battery lifetime and a high density may limit recovery rate. OpenField™ Technology have developed a pressure and temperature monitoring microsystem encased in a Φ50.8 mm spherical titanium shell that can flow in well pipes for downhole monitoring [Ope13]. However, its large size may prevent it from being used in smaller wellbores. For applications in the oil well logging, systems built with commercial electronics that can achieve similar functions are of great interest.

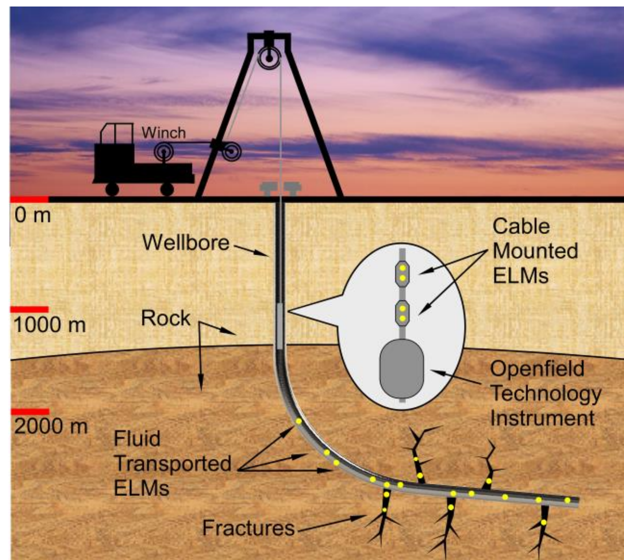

Figure 1.3: Deployment of autonomous microsystems in a wellbore [Sui17].

Motivated by pipeline needs for pipeline leak detection and location, and wellbore needs for data collection in horizontal wellbores and fractures, this work focuses on investigating critical

elements of system design and package integration for environmental sensing autonomous microsystems, specifically for pipeline monitoring and downhole monitoring applications.

Pipeline and downhole applications have different environment conditions and requirements, and these affect the system configuration needed for the application. Oil and gas pipelines have a maximum temperature of around 60°C and a maximum pressure of around 10 MPa [Ken93]. Hence, for monitoring oil and gas pipelines, the system should achieve temperature logging up to 60°C and pressure logging up to 10 MPa. For oil reservoirs that are typically 0.6-6 kilometers deep underground, the upper limit for the typical downhole environment temperature is ≥75ºC and pressure is ≥15 MPa [Cha12]. Therefore, for downhole monitoring, the system design is chosen to provide an upper limit of ≥75ºC for temperature and ≥15 MPa for pressure logging. Both pipeline and downhole monitoring can sometimes benefit from the geolocation of the system. Hence, inertial sensors are needed for both applications. For pipeline application, the system size is restricted to centimeter scale to permit monitoring of small diameter pipelines. For downhole application, the system size is restricted to centimeter scale, limited by the size of the well bore. The packaging requirements are different for systems in the two applications due to the differences in deploying environment conditions. For both applications, between deployments, the systems should be able to accommodate wirelessly recharging of the battery as well as wireless communication with the external user.

1.2 Existing Microbattery Designs and Wireless Power Transfer Methods

1.2.1 Power Source Requirements

Microbattery requirements are heavily dependent on the desired application. If the system will only be single-use, primary batteries are permitted; however, if it to be re-used, secondary (rechargeable batteries) may be required it is to be re-used numerous times. The battery can also

be used in conjunction with an energy harvester to serve as an energy buffer. An ideal microbattery may need to meet many requirements, such as small size, high energy density, high charging and discharging current, low self-discharge, long cycle-life, good mechanical and electrochemical stability, and good safety.

A Ragone plot is used to compare the energy and power densities of different power technologies. The Ragone plot in Figure 1.4 compares some of the secondary battery chemistries with other power technologies like super-capacitors and fuel cells. Super-capacitors have high power density but low energy density whereas fuel cells have high energy density but low power density. The various battery chemistries have varying range of energy and power densities for powering various microsystems.

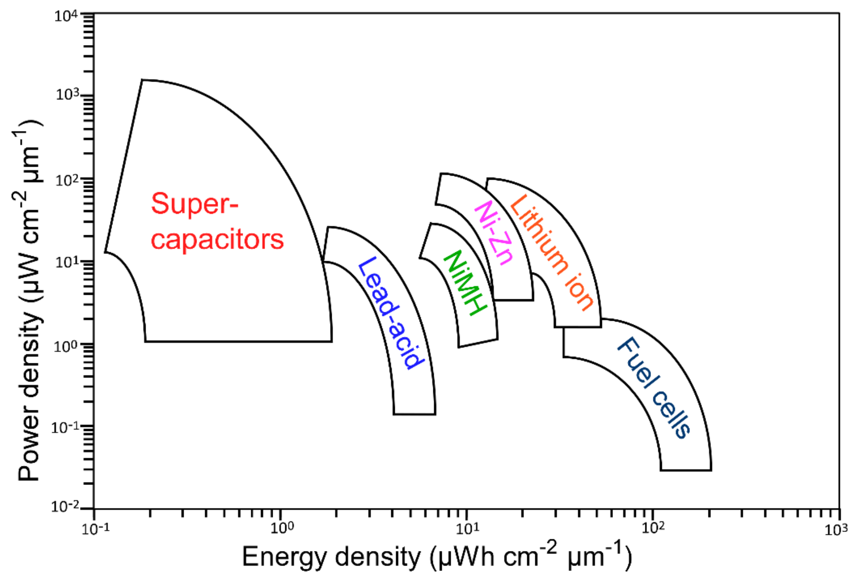

Figure 1.4: Ragone plot indicating the various power technologies (adapted from [Pik13]).

1.2.2 Battery Chemistry

There are various primary (non-rechargeable) battery chemistries including primary zinc-manganese dioxide (Zn-MnO_2), lithium-manganese oxide (Li-MnO), zinc-air (Zn-air), and silver oxide (Ag_2O). Secondary (rechargeable) battery chemistries include lithium-ion (Li-ion), nickel-zinc (Ni-Zn), nickel-metal hydride (NiMH), sodium-sulfur (Na-S), and silver-zinc (Ag-Zn).

Zn-MnO_2 (commonly known as alkaline) is one of the most popular primary battery chemistries. They use Zn as the negative electrode, MnO_2 as the positive electrode and potassium hydroxide (KOH) as the alkaline electrolyte. They have a nominal voltage of 1.5 V. One research group has demonstrated a printed, flexible array of Zn-MnO_2 microbatteries by stencil-printing the Zn and MnO_2 electrodes on fibrous substrates [Gai13]. Cellulose-based material soaked with KOH was used as the separator and silver-based inks were used for current collectors. The batteries had an areal capacity of 0.8 mAh/cm^2.

Lithium primary batteries use metallic lithium as the anode and several different materials for the cathode. The most frequently used cathode material is MnO, which delivers a cell voltage of 3 V. One research group fabricated Li-MnO primary cells by electrodepositing high capacity electrolytic materials on an interdigitated 3D nanoporous bicontinuous architecture (Figure 1.5) [Pik13]. The microbatteries had a capacity density of up to 29.5 µAh/cm^{2}µm.

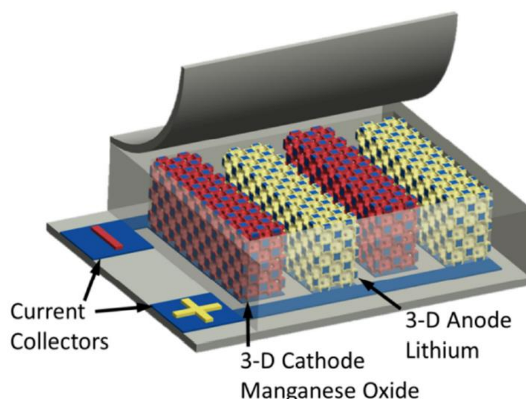

Figure 1.5: Microbattery design. Nickel scaffold was used as the current collector (blue). Manganese oxide was used as the cathode (red) and lithium as the anode (yellow) [Pik13].

Zn-air batteries are metal-air batteries that employ metallic zinc particles as the anode and an aqueous liquid electrolyte. For this type of battery, oxygen from the surrounding air is reduced at a catalyst inside the battery. These batteries have a typical voltage of 1.4 V. One research group developed a 3D Zn-air microbattery with a high surface area micromachined metallic scaffold

which supported the electrodeposited Zn anode. They used a commercially available air cathode and 7 M aqueous KOH solution as the electrolyte [Arm11]. These microbatteries had a capacity of 2.5 mAh/cm^2.

Li-ion batteries are popular secondary batteries since lithium is the lightest and the most electropositive element, producing the highest specific capacity suitable for the application. They use a variety of materials for the anode, cathode, and electrolyte. The research in [Nat05] led to 3D thin film Li-ion microbatteries using nickel as cathode current collector, molybdenum oxysulphide as cathode, hybrid polymer electrolyte, and lithiated graphite as the anode, as well as an anode current collector. The electrodes, electrolyte and current collectors were deposited conformally and sequentially on a perforated substrate made of silicon or glass. The 3D cells exhibited a capacity of 2 mAh/cm^2 and could be cycled 200 times. Another group used 3D printing to fabricate 3D interdigitated microbatteries composed of high-aspect ratio anode and cathode micro-arrays [Sun13]. They used $Li_4Ti_5O_{12}$ (LTO) as the anode $LiFePO_4$ (LFP) as the cathode, and 1 M $LiClO_4$ (in 1:1 ratio of EC: DMC by volume) as the electrolyte. The batteries had a capacity of 1.5 mAh/cm^2 and were demonstrated to work up to 30 cycles.

NiMH batteries use nickel oxyhydroxide (NiOOH) as the cathode, metal hydride (MH) as the anode, and an alkaline electrolyte. They have a typical voltage of 1.2 V.

Ni-Zn is another commonly used rechargeable battery chemistry and is expected to soon replace both NiMH and Li-ion [Par17], as it is safer to operate, has high specific capacity and power, and Zn is globally available and inexpensive. Although Li-ion batteries are appealing in terms of energy density, cyclability and high-temperature performance, Ni-Zn batteries have benefits like high power density and good cyclability. Additionally, Ni-Zn batteries utilize low-cost materials that are easy to handle and are more environmentally benign.

1.2.3 Wireless Power Transfer Methods

Wireless power transfer is attractive for its ability to charge the microsystem through a fully sealed package. The wireless charging methods for microsystems are broadly classified into non-radiative (near-field and mid-field) and radiative (far-field) methods based on the distance between the transmitter and the receiver [Lu16]. There are three commonly used non-radiative charging methods: capacitive coupling, inductive coupling, and magnetic resonance coupling. The radiative charging methods mainly consist of RF/microwave charging and optical charging. Acoustic charging is a relatively new wireless charging method that is being used for some applications [Roe13].

Capacitive coupling uses electrodes, such as metal plates to transfer energy by electric field [Kli11]. The transmitter and receiver electrodes form the capacitor electrodes with the intermediate medium as the dielectric. Capacitive coupling requires very large voltages on the electrodes to transmit significant amount of power, typically limiting it to low-power applications.

Inductive coupling is based on magnetic field induction which transfers power between a transmitter and receiver coil. It is the most widely used wireless power transfer technology, having been extensively commercialized. This is due to its ease of implementation, convenient operation, high efficiency over short distances, and good safety [Lu16].

Magnetic/inductive resonance coupling is based on power transfer between two resonant coils through varying or oscillating magnetic fields. Due to the property of resonance, it has the advantage of immunity to neighboring environment and is not limited to line-of-sight transfer requirements; however, proper alignment of the charger and charging device is necessary to ensure good coupling and achieve adequate charging efficiency [Lu16]. Qi is an international wireless charging standard developed by the Wireless Power Consortium (WPC) that uses magnetic resonance coupling.

RF/microwave charging uses RF and microwaves as the energy delivery medium [Lu16]. Due to the safety issues of RF exposure [Bra09], it is only suitable for applications with up to 10 mW power consumption. RF charging has been used to supply energy to wireless sensor nodes in an outdoor environment in [Kuh15].

Optical energy transfer is a high-power long-range method that uses light to transmit energy from an optical power source to the receiver and has been highly commercialized. The receiver uses a miniature photovoltaic cell to convert transmitted light into electrical power. Wi-Charge is a company developing products for far-field wireless power transfer using focused infrared beams [Cha18].

Acoustic charging uses sound waves to wirelessly transfer energy between the transmitter and the receiver [Roe13]. In contrast with electromagnetic (EM) field based wireless energy transfer approaches, acoustic energy transfer (AET) uses lower propagation speed for waves in air. Therefore, the sound waves have a smaller wavelength for a given frequency than the EM waves; for a given directionality of the transmitter, they permit a size reduction of several orders of magnitude of the transmitter and receiver (compared to EM power transfer) [Den10]. AET has been primarily used to charge implants in biomedical applications [Bas16]. Table 1.1 compares and summarizes these wireless power transfer methods.

Table 1.1: Comparison of various wireless power transfer methods [Lu16]

Wireless Charging Method	**Operating Frequency Range**	**Effective Charging Distance**	**Directivity**	**Comments**
Capacitive coupling	kHz – MHz	< few cm	Low	Low power due to limitation on electrode voltage
Inductive coupling	Hz – MHz	< few cm		Requires proper positioning of coils
Inductive/ magnetic resonance coupling	kHz – GHz	< few cm		Immunity to neighboring environment
RF/microwave	GHz	< few km	High	Low power due to safety issue
Optical	≥THz	< few m		Requires line-of-sight
Acoustic	<10 MHz	< few m	High	No EM wave interference

1.3 Wireless Communication Methods for Microsystems

The communication method is an important factor in a sensor system for system control and data transfer to an external unit. The communication module typically consumes more energy compared to other modules [Hea08]. To conserve power, the module is placed in sleep mode if the system is not performing any active communication function. However, if the system needs to wake up from the sleep mode frequently, placing it in sleep mode is not optimal, as the transition to and from sleep mode can also consume substantial energy [Aky02]. For downhole monitoring application, the ELM will be deployed in an environment that is filled with highly saline brine solution. This results in high attenuation of electromagnetic waves during transmission, preventing the system to communicate directly with the external unit on the ground [Ser15]. Therefore, communication is limited to before deployment and after retrieval.

There are three types of wireless communication methods widely used in sensing microsystems: optical, active RF, and passive RF. Wireless optical communication uses a transmitter, such as an LED or laser diode, free space as the channel for light transmission, and a photodiode receiver. Wireless optical communication has been demonstrated using a laser diode and an avalanche photodiode over a 20 m long underwater channel [She16]. Compared to RF communication, optical communication is easier to implement with smaller and lighter components. One major constraint is that optical communication requires dark environment as the ambient light contributes to high white noise.

RF communication uses radio-frequency electromagnetic waves to send signals between a transmitting device and a receiver. RF communication is ideal for wireless sensing microsystems, as unlike optical communication, it is not limited to line-of-sight. It can be implemented by low-power radio transceivers with data-rates and ranges scalable according to application. There are several frequency bands in which RF devices operate, enabling different applications [ISM18].

Active RF communication systems have their own transmitter and an integrated power source. This form of RF communication is widely used in wireless communication networks where devices share a lot of data with each other frequently or systems that need to be tracked over long distances. Some popular protocols supported by such systems include Bluetooth, Bluetooth low energy (BLE), ZigBee, and Wi-Fi [Blu15, WiF15, Zig15].

Passive RF communication systems have an external transponder that sends radio signal to a receiving electronic microsystem. This microsystem uses the transmitted signal to power on and reflect energy back to the reader. Passive RF systems use tags and do not require integrated power sources. They have moderate communication speed and shorter range compared to active RF systems. One example for passive RF communication is RFID module. Table 1.2 provides a comparison of the different communication methods.

Table 1.2: Comparison of communication methods [Sui17]

Communication Method		Read Range	Data Rate	Power Consumption
Optical		Usually < 1 m	Few kb/s	High
Passive RF: RFID		<5 m	Few kb/s	Low
Active RF	Bluetooth	<10 m	1-3 Mb/s	High
	BLE	< 100 m	1-2 Mb/s	Medium
	ZigBee	< 300 m	20-250 kb/s	Medium
	Wi-Fi	20 m indoor	6-500 Mb/s	High

1.4 Requirements of System Integration and Packaging

Cost reduction is a major challenge facing the integration and packaging of microsystems with packaging representing up to 80% of a MEMS device's total cost [Gil05, Lau10, All03]. Although many of the MEMS packaging technologies are adapted from the integrated circuit (IC) industry, it is widely acknowledged that packaging MEMS devices and microsystems is much more difficult than packaging ICs [Naj03, Lee09]. This is because that, compared to most IC devices which are planar, stationary, solid, and purely working in electrical domain, most MEMS

devices have 3D structures, include moving parts, and require interaction with complex domains, such as physical (pressure, acceleration, fluidics), chemical (chemical species, concentrations, reactions) etc. Microelectronics packaging provides mechanical support, electrical connection, and protection to the integrated circuits (IC) from the external environment. In addition to the above requirements, the microsystems packaging must also permit exposure of the sensing or actuating elements to the surrounding environment [Hsu00]. Microsystem integration and packaging involve three major tasks: encapsulation of the transducer, interconnection between the transducer and sensing environment, and assembly of different chips and modules [Naj03]. Three-dimensional (3D) integration and packaging technologies where the bare dice or multi-chip modules (MCMs) are stacked along the z-axis can improve the compactness significantly [Al98].

The general requirements of a microsystem package are: (1) mechanical protection from the external environment; (2) resistance to chemicals in the target environment; (3) proper sealing from water or gas depending on the application; (4) application-specific selective sensor access to exterior environments [Ma16]. The packaging process is required to be low cost, small, reliable, easily manufacturable, and scalable. The general requirements of multi-chip module integration techniques are reliability, re-workability/reconfigurability, and modularity [Naj03]. Re-workability allows the individual units of the system to be disassembled after assembly and reassembled again without the loss of performance or yield. This significantly reduces the overall cost of microsystems [Naj03]. Modularity allows various chips to be assembled in a modular fashion such that one chip can be taken out and replaced with another without requiring new set of hardware. Cost can be further reduced if the integration technique permits reuse of the package.

1.4.1 Functional Packaging

Packages produced with MEMS technologies can provide additional benefits such as provide functions of certain system components like battery, antenna, and sensors, along with the traditional benefits such as environmental protection and selective environmental interface. These additional functions result in easier system integration, lower cost and/or increased compactness and thus enhance the overall system functionality [Jun03]. This is the concept of functional packaging.

Researchers from KAUST, Saudi Arabia have demonstrated a system with a functional package for large area environmental monitoring [Far17]. They used inkjet-printing to print sensors (temperature and H_2S) and an antenna on the outer walls of a 3D-printed cubic package (21 mm × 21 mm × 21 mm). The microelectronics developed on a 3D printed circuit board and battery were enclosed in the package. A humidity sensor was 3D printed and placed at the bottom of the package. Two types of sensing mechanisms were used: resistive sensing for detecting H_2S and temperature, and capacitive sensing for humidity detection. The corresponding changes in resistance and capacitance were processed by the integrated electronics and transmitted wirelessly using ZigBee.

Researchers have also demonstrated a 3D printed origami package for enclosing RF electronics [Kim15]. The package was 3D printed as a planar structure with smart shape-memory hinges that allowed origami folding to a 3D shape after heating. The system consisted of inkjet printed on-package patch antennas for RF signal reception (for harvesting or communication) at orthogonal orientations. The total system volume was reduced by hosting the antennas directly on the package instead of using monopole/dipole wire antennas stemming out of the package. Additionally, mechanical damage (e.g., breaking) of antennas could also be minimized since the antennas were a part of the package.

1.5 Previous Generations of Environmental Logging Microsystem (ELM)

Previous Environmental Logging Microsystems (ELM1, ELM2, and ELM3) were designed for a downhole monitoring application. The systems were capable of monitoring data in high-temperature, high-pressure and high-salinity subsurface environments, such as the wellbore of an oil well. These microsystems had data logging capabilities and were intended to be retrieved after data collection for interrogation by the client. The systems used optical methods for charging and communication. They consisted of the smallest suitable off-the-shelf electronic and battery components that were compatible with assembly on a flexible printed circuit board.

The ELM1 PCB was folded into a stack and placed in a stainless-steel package with a sapphire lid. A parylene layer was coated on the outer surface of the package for anti-corrosive protection. The ELM2 PCB was folded into a stack and encapsulated in a stainless-steel tube, which provided impact and abrasion tolerance. The tube was filled with a transparent polymer. The transparent nature of the epoxy allows the optical charging and communication of the system. The filler polymer material also transferred the external pressure to the pressure sensors with low attenuation. The ELM3 PCB was left unfolded and encapsulated in a transparent polymer mold for anti-corrosion protection. Photos of the packaged ELMs are shown in Figure 1.6. More details about the packaging technologies used previous generations of ELM can be found in [Ma16].

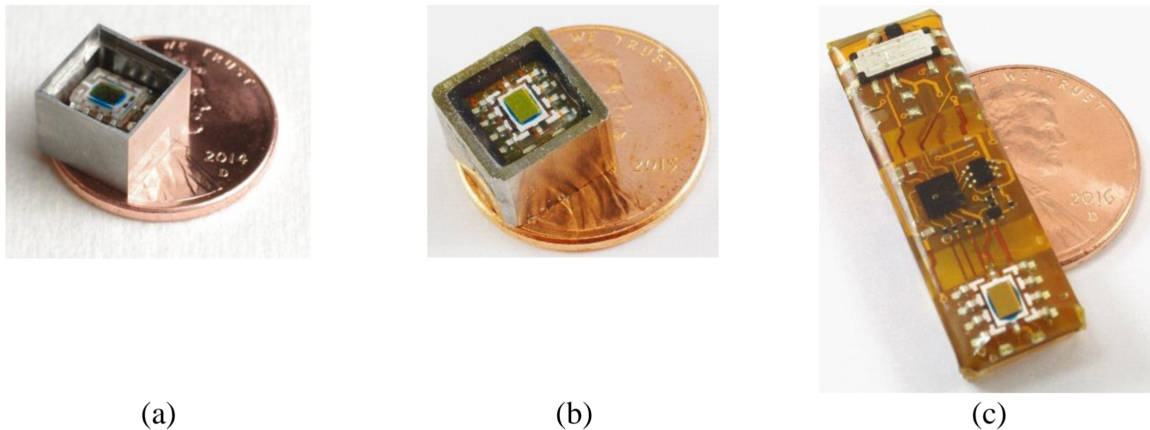

(a) (b) (c)

Figure 1.6: Packaged system (a) ELM1; (b) ELM2; and (c) ELM3 [Ma16, Sui17].

The features of the three generations of ELM are briefly summarized in Table 1.3 and more details can be found in [Sui17]. The ELM systems were not designed to be flow-compatible (e.g. density matched) and could only be deployed using a tethered modality.

Table 1.3: Summary of previous generations of ELM [Sui17]

Features	ELM1	ELM2	ELM3
P logging	No	Yes	Yes
P range (MPa / psi)	-	50 / 7200	50 / 7200
P resolution (kPa / psi)	-	2 / 0.3	2 / 0.3
T logging	Yes	Yes	Yes
T range (ºC)	-20 to 150	-20 to 150	-20 to 150
T resolution (ºC)	0.1	0.1	0.1
Communication	LED	LED	LED
Power switch & improved manufacturing	No	No	Present
Battery recharging	Optical	Optical	Optical
Max stored data points	1270	1270	1270
Lifetime: Days @125ºC	0.5	1	1
Designed PCB stack size (mm^3)	6.5×6.3×4.5	6.5 × 6.5 × 5.8	8.8 × 8.6 × 7.2
Package material	Stainless steel shell with sapphire lid	Stainless steel tube filled with polymer	Polymer mold
Packaged system size (mm^3)	8.9×8.9×6.85	9.5×9.5×6.5	29 × 8.8 × 3.0

1.6 Goals, Tasks, and Challenges

This dissertation is aimed at investigating critical elements of critical elements of system design and package integration for environmental sensing autonomous microsystems, specifically for pipeline monitoring and downhole monitoring applications.

The first goal is to investigate the system level design compromises, relationships between the building blocks, and overall performance limits under deployment conditions – including those at elevated temperatures and pressures for autonomous microsystems. This goal is achieved by developing: 1) an environmental logging microsystem (ELM6) for pipeline monitoring applications and 2) an environmental logging microsystem (ELM7) for downhole monitoring applications. For monitoring oil and gas pipelines, sensing targets include temperature monitoring up to 60°C and a preferred resolution of 0.5°C, pressure logging up to 10 MPa and a preferred resolution of 2 kPa, and inertial (accelerometer and magnetometer) data logging. The system size

is restricted to centimeter scale to permit monitoring of small diameter ($<\Phi 5$ cm) pipelines. The small system size reduces the available volume for power sources, necessitating low power consumption and compact system design with fully integrated sensing functionality. Between deployments, the system should be able to accommodate wireless recharging of the battery as well as wireless communication with the external user. For oil reservoirs that are typically 0.6-6 kilometers deep underground, the typical downhole environment can have upper limit of pressures and temperatures to be ≥15 MPa and ≥75°C, respectively [Cha12]. For downhole monitoring, the sensing targets include operating temperature with an upper limit of ≥75ºC and a preferred resolution of 0.1°C, operating pressure with an upper limit of ≥15 MPa and a preferred resolution of 0.5 kPa, and inertial data logging. The system size is restricted to centimeter scale, limited by the size of the well bore. Between deployments, the system should be able to accommodate wireless recharging of the battery as well as wireless communication with the external user. Additionally, the system should limit memory usage, operate at low power, and accommodate re-usability of the electronics should the battery become non-functional. Efforts toward these goals are described in Chapter 2 (ELM6) and Chapter 3 (ELM7).

The second goal is to investigate a package integration approach to permit deployment, retrieval, and reusability of the downhole sensing microsystems. The package integration approach must protect the electronics from the harsh environment while permitting transfer of external pressure and temperature to the sensors during deployments; between deployments it must allow wireless charging and wireless communication, and in certain situations it must also allow the removal of the package and reusability of the system hardware. These goals are achieved by designing the ELM7 electronics, power source, and sensors to fit within a flow-compatible package designed to operate within oil well bores. This requires the proper positioning of the

pressure sensor, wireless charging coil, and BLE MCU on the PCB. Efforts toward this goal are described in Chapter 4.

The third goal is to investigate a scalable fabrication method for incorporating microbatteries within autonomous microsystems. This goal is achieved by designing a batch mode fabrication process for microbatteries that have sufficient energy and power density for powering autonomous microsystems. The microbatteries should have a voltage of 1.7 V and a footprint ≤5 mm^2. Challenges are in the preparation and handling of battery materials, battery material integration, and process improvement; efforts describing solutions to meet these goals are described in Chapter 5.

The design targets of this dissertation are summarized in Table 1.4.

Table 1.4: Design targets of this dissertation

Goals	Tasks	Parameters	Targets
System level design compromises, relationships between building blocks, and overall performance limits under deployment conditions	Investigate ELM for pipeline monitoring	Upper limit of operating pressure	10 MPa (1450 psi)
		Upper limit of operating temperature	60°C
		System PCB stack diagonal	<Φ5 cm
	Investigate ELM for downhole monitoring	Upper limit of operating pressure	≥15 MPa (2175 psi)
		Upper limit of operating temperature	≥75°C
		System PCB diameter < Package diameter	
Package integration method to permit deployment, retrieval, and reusability of downhole sensing systems	Incorporate within flow-compatible package for ELM for downhole monitoring	Upper limit of operating pressure	≥15 MPa (2175 psi)
		Upper limit of operating temperature	≥75°C
		Packaged system volume	≤25 cm^3
		Packaged system density	≤1.2 g/cc
Scalable fabrication method for microbatteries	Investigate a batch mode process for fabrication of microbatteries	Capacity density	>1 mAh/cm^2
		Voltage	1.7 V
		Footprint	≤5 mm^2
		Energy density	>2 mWh/cm^2
		Average power density @ 1mA discharge	>25 mW/cm^2

1.7 Organization of Dissertation

This dissertation is arranged into six chapters. Chapter 1 introduces the topic, including microsystems for pipeline monitoring and downhole monitoring applications, existing microbattery designs, wireless power transfer methods and wireless communication methods for microsystems, microsystem integration and packaging, and previous generations of ELM.

Chapter 2 describes the work on the development of an environmental logging microsystem (ELM6) for pipeline monitoring application. The system used resonant inductive charging, BLE protocol for communication, and recorded data from temperature, pressure, and inertial sensors. The electronics of the system were integrated on a flexible polyimide PCB with a designed stack size of $15.4 \times 14.2 \times 11.2$ mm^3. The system was successfully tested up to 65°C and 12 MPa, had a standby current of 8 µA at room temperature (RT) which permitted a lifetime of 10 days at RT with sensor data recorded every 12 hours.

Chapter 3 describes the work on the development of an environmental logging microsystem (ELM7) for downhole monitoring application. The system used Qi protocol for wireless charging, BLE protocol for communication, and recorded data from temperature, pressure, and inertial sensors. The ELM7 was successfully tested up to 85°C and up to 160°C for all elements excluding the battery.

Chapter 4 describes the work on a package integration approach developed for downhole monitoring, maintaining a volume of <25 cm^3 and density <1.2 g/cc. The ELM7 microsystem was encapsulated in this package and successfully tested up to 85°C and 41.5 MPa for >4 days in laboratory conditions. Field trials of these packaged systems were successfully completed by repeated deployment in an operational oil well to a depth of 1,290 m, during which data was

successfully logged. These systems were retrieved and successfully interrogated at the end of deployment.

Chapter 5 describes a scalable fabrication method for batch mode fabrication of high capacity rechargeable nickel-zinc micro batteries. The fabricated batteries had a typical footprint of ≈0.048 cm^2, a nominal voltage of 1.7 V, a typical capacity of ≈63 μAh (corresponding to an energy density of 1.32 mAh/cm^2), and a maximum power of 1.45 mW with an average power density of 26.88 mW/cm^2. These batteries may provide sufficient power and energy density for millimeter-scale autonomous microsystems that are being developed for environment sensing applications.

Chapter 6 provides the conclusions from this dissertation, summarizes major contributions, and proposes future work for an environmental logging microsystem for downhole operation up to 125°C and a battery integration method for autonomous microsystems.

CHAPTER 2: Environmental Logging Microsystem for Pipeline Monitoring

As noted in Chapter 1, the first goal is to investigate the system level design compromises, relationships between the building blocks, and overall performance limits under deployment conditions. Toward that end, this chapter describes a wireless autonomous environmental logging microsystem (ELM6) developed for pipeline monitoring application.

Pipeline systems are responsible for transporting vital materials such as water, oil, and gas. Leakage of oil and gas from pipelines can not only cause significant economic losses but also pose a significant threat to the environment and life. Oil and gas pipelines have a maximum temperature of around 60°C and a maximum pressure of around 10 MPa [Ken93]. Leaks alter the pressure and temperature in the pipe [Sad14]. There are multiple methods used to detect and locate leaks in pipelines [Liu12]. Pure Technologies Ltd. have developed a free-swimming spherical device called SmartBall™ to detect and locate leaks; however, they have an exterior diameter of >Φ100 mm, rendering them unsuitable for small diameter pipelines [Fle08]. ‘Smart pigs’, consisting of various sensors and electronics are commonly used to detect and locate leaks in pipelines [Kup05]. They are designed to travel in the interior of the pipeline, usually while the line is in service. Smart pigs are not suitable for pipelines with a diameter of less than 2 inches (5.1 cm) [Fle15]. Another drawback is the risk of pigs becoming lodged in the pipeline, which can interrupt or stop product flow [Fun06].

Microsystems capable of sensing pressure, temperature and inertial parameters can be incorporated into smart pigs or used independently. In general, these microsystems can be used within factories where there is continuous flow processing. For monitoring oil and gas pipelines,

these systems should achieve temperature logging up to 60°C and a preferred resolution of 0.5°C, pressure logging up to 10 MPa and a preferred resolution of 2 kPa, and permit inertial data logging. The size of the systems should be restricted to centimeter scale to permit monitoring of small diameter pipelines. Between deployments, the systems should be able to accommodate wireless recharging of the battery as well as wireless communication with the external user.

Previous generations of ELM systems used for downhole monitoring all used an optical approach for wireless communication and charging. The optical communication allowed wireless system control and data readout by using an optical readout box. However, it required alignment between the system and the readout box, i.e., line-of-sight communication. Additionally, extended use of the systems resulted in dirty or roughened surfaces that compromised the transparency necessary for optical communication. These issues are not of significant concern for simple and short optical commands but can present a major challenge for transfer of large quantities of sensor data. It is, therefore, desirable to have radio frequency (RF) wireless communication capability, particularly for transfer of sensor data.

For the purpose of this work, it is beneficial to use a standard communication protocol to take advantage of the abundant technology base and readily available support infrastructure. The most widely used options for low power RF wireless communication protocols include BLE and Zigbee. These two options have similar power consumption (10 to 100 mW) [Ray15]. Although BLE has a shorter communication range that is about one third of Zigbee (77 m for BLE and 291 m for Zigbee) [Lin15] , it has a data rate that is four times of Zigbee (1 Mb/s for BLE and 250 kb/s for Zigbee) [Elk16]. Zigbee is more susceptible to interference in noisy environments [Ghe18]. Based on comparison of these options, BLE is selected as the wireless communication protocol

for implementation in the ELM6 system. BLE also allows easy interoperability with mobile phones and laptop computers without the need for additional hardware.

It is also beneficial to incorporate an industry-standard protocol for wireless charging into ELM6. The Qi protocol is the most widely used open interface standard that defines wireless power transfer using inductive / resonant inductive charging. Because of its operation in resonance mode, it has the advantage of immunity to environmental interference and does not require optical line-of-sight transfer, even though alignment of the charger and the device being charged is necessary to ensure good coupling and achieve the desired charging efficiency.

The ELM6, designed for temperature, pressure, and inertial data logging in pipeline environment used the smallest suitable off-the-shelf electronic and battery components that are compatible with assembly on a flexible printed circuit board. The designed system stack size was $15.4 \times 14.2 \times 11.2$ mm^3. The system was successfully tested at up to 65°C and 12 MPa. It had a standby current of 8 µA at room temperature and the system lifetime was >10 days when operated at room temperature with detection interval of 12 hours.

2.1 System Hardware

The block diagram of ELM6 is shown in Figure 2.1. The microsystem consists of two MCUs: Sensor-MCU (S-MCU) and BLE-MCU (B-MCU), a wireless power receiver kit, an external wireless power transmitter kit, a charging circuit, a battery and a mechanical switch, MEMS pressure sensor, an inertial measurement unit (IMU), and an external Bluetooth module. Sensor data is collected and stored in S-MCU during deployment, transferred from S-MCU to B-MCU using the Inter-Integrated Circuit (I^2C) bus before data readout, and wirelessly sent from the B-MCU to the external readout unit using the BLE protocol.

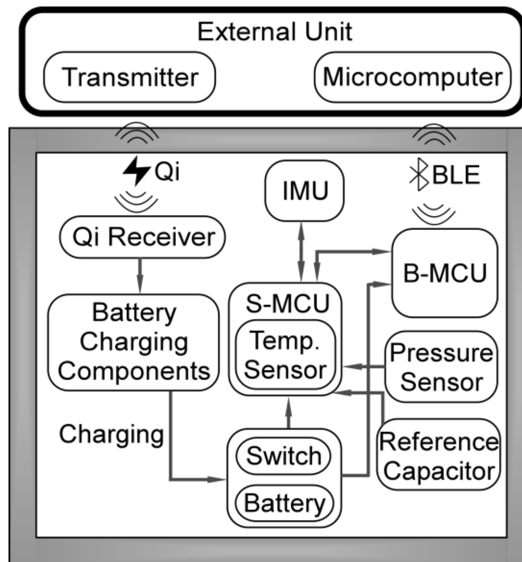

Figure 2.1: ELM6 block diagram.

The schematic of the system circuit for ELM6 is shown in Figure 2.2. A receiver kit and an external transmitter kit, along with charging components are used for wireless charging of the battery. The mechanical switch is used to conserve the battery power prior to packaging and deployment. The S-MCU is used to interface with the MEMS pressure sensor and the IMU; it also provides temperature sensing using an internal circuit. It uses the I^2C protocol for communication with the IMU. The IMU consists of an accelerometer and a magnetometer and can be used for geolocation monitoring of the system. A reference capacitor is included to compensate for the temperature dependency of the S-MCU capacitance sensing module.

The B-MCU is used for wireless communication with the Bluetooth external unit using the BLE protocol. The external unit/user communicates with the S-MCU via the B-MCU. The command to be sent to the S-MCU by the user is first sent to the B-MCU via the BLE protocol. The B-MCU then sends this command to the S-MCU using the I^2C protocol. During deployment, the sensor data is collected and stored in the S-MCU. This data is sent from the S-MCU to the B-MCU using the I^2C bus before data readout, and wirelessly sent from the B-MCU to the external readout unit using the BLE protocol.

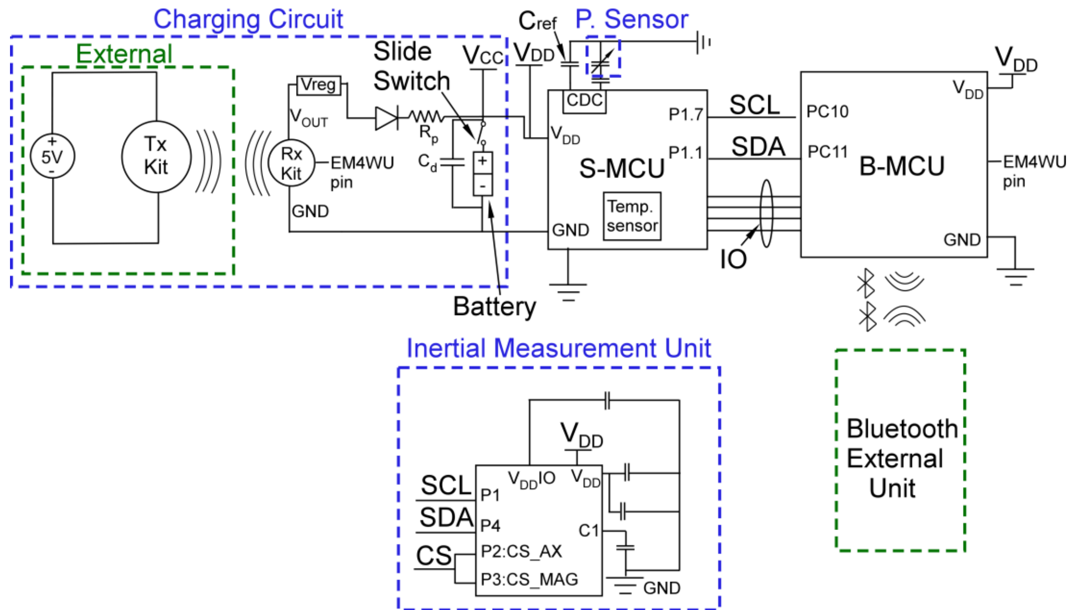

Figure 2.2: Circuit schematic for ELM6.

2.1.1 Component Selection

The general rules for selecting the components, listed in the sequence of preference, include small footprint, low power consumption, and integrated functionality. All components are commercially available from electronic element distributors such as Digi-Key Corporation. Table 2.1 summarizes the selected major components of the system circuit and their relevant features for the target application.

Table 2.1: Major system components

Component	Part No.	Footprint	Device Feature
Wireless charging transmitter kit	STMicro STEVAL-ISB038V1T	Φ20.0 mm	Follows Qi protocol
Wireless charging receiver kit	STMicro STEVAL-ISB038V1R	Φ11.0 mm	Follows Qi protocol
Battery	Seiko Instr. MS920SE	Φ9.5 mm	3 V, 9 mAh capacity for a cut-off voltage of 2.4 V
Mechanical slide switch	C&K PCM12SM	8.3 mm × 5.0 mm	Single pole double throw switch
S-MCU	Silicon Labs C8051F990	3.0 mm × 3.0 mm	0.8 μA sleep mode current, 80 μA active current, integrated temperature sensor
B-MCU	Silicon Labs BGM121	6.5 mm × 6.5 mm	2.5 μA deep sleep mode current, integrated antenna
IMU	STMicro LSM303C	2.0 mm × 2.0 mm	3-axis accelerometer, 3-axis magnetometer
Bluetooth external unit	RASPBERRY PI 3 STARTER KIT	167.6 mm × 124.5 mm	Raspberry Pi with integrated Bluetooth module

2.1.2 Charging Circuit Block

The charging circuit block includes an external transmitter kit (Tx kit) and a receiver kit (Rx kit) for wireless power transfer, Seiko Instruments MS920SE rechargeable lithium battery for energy storage, a decoupling capacitor (C_d), a voltage regulator to step down the voltage going into the battery, a rectifier diode to prevent the reverse flow of the charging current, a protection resistor R_p to limit the charging current, and a slide switch to avoid draining the battery during storage. A voltage value of 5 V is generated at the output of the Rx kit during wireless power transfer. This voltage is stepped down to 3.3 V by the voltage regulator. This results in a current flowing from the Rx kit, through the voltage regulator, rectifier diode, and the protection resistor, into the battery for charging.

The wireless power transfer is achieved by using a transmitter and a receiver kit (Figure 2.3) as detailed in Table 2.1. The kits support wireless power transfer of up to 1 W through a Φ11 mm coil on the receiver side and a Φ20 mm coil on the transmitter side. The chip used in the transmitter is STWBC-WA and the chip in the receiver is STWLC04. The STWLC04 receiver can deliver the output power in two modes: as a power supply with 5 V output voltage or as a constant current/constant voltage (CC/CV) battery charger with configurable charging current and voltage. It has been used as a power supply configured with 5 V output in this effort as the battery will be charged at a constant voltage.

The MS920SE battery uses silicon oxide as its anode and lithium manganese composite oxide as its cathode. This battery has a capacity of 11 mAh for a cut-off voltage of 2.2 V, 9 mAh capacity for a cut-off voltage of 2.4 V, and a form factor of Φ9.5 mm×2.7 mm. The specified operating temperature for the battery is -20°C to +60°C [Sei14]. A buffer capacitor of 330 μF is connected in parallel to the battery to accommodate any transient current need when the system operates in the active mode. A mechanical slide switch is added in series with the battery, which

can break the power during storage and eliminate the sleep mode current consumption. The system lifetime is thus greatly extended during storage.

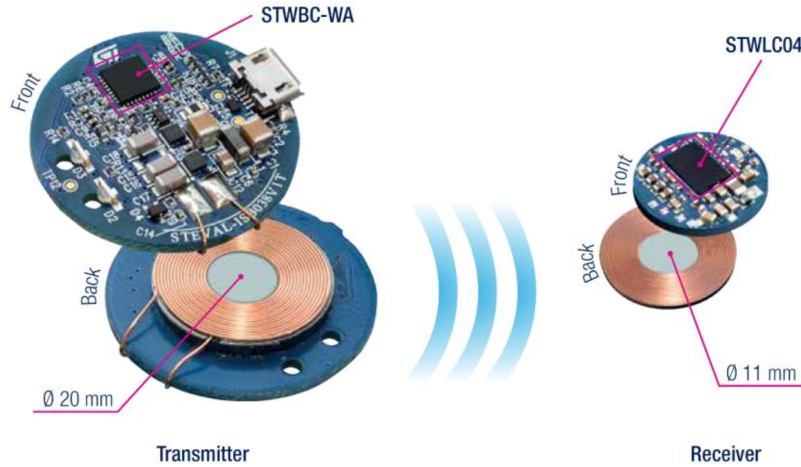

Figure 2.3: Transmitter and receiver kits for wireless power transfer [STM17].

2.1.3 Silicon Labs C8051F990 MCU

For this work, the C8051F990 low power MCU from Silicon Laboratories, Inc. [Sil11] is selected over other options for S-MCU. This MCU has an integrated temperature sensor, an integrated capacitive sensing module, a small footprint of 3×3 mm^2, and low power consumption (80 μA in the active mode and 0.8 μA in the sleep mode) at room temperature. This MCU was also used in the previous generations of ELM [Sui17]. Other MCUs that were considered then include Freescale KL03, Atmel Attiny20, and TI MSP430 series. Table 2.2 compares the key parameters of some of these MCUs [Sui17]. After the system is powered on, the S-MCU stays in the sleep mode until it is awakened into active mode and triggered into different operation states by the B-MCU through I^{2}C bus. In the detection state, temperature measurements are made using the internal temperature sensor, pressure measurements are made from the MEMS pressure sensor through the Capacitance-Digital-Converter (CDC) module, and inertial sensor measurements are made by the IMU and received using the I^{2}C bus. The measured sensor data is stored in the flash memory and is sent from the S-MCU to the B-MCU using the I^{2}C bus before data readout, and wirelessly sent from the B-MCU to the external readout unit using the BLE protocol.

Table 2.2: Comparison of MCUs for S-MCU

MCU Part Number	Si Labs C8051F990	Freescale KL03	Atmel ATtiny20
Operating Temp.	-40 to 85°C	-40 to 85°C WLCSP / -40 to 105°C QFN	-55 to 125°C
Current Consumption	Core current consumption: 82 µA at 32 kHz ADC current consumption: 370 µA (low power mode) Sleep mode current consumption: 0.6 µA	Run current consumption: 50 µA/MHz Standby current consumption as low as 2.2 µA	Active mode: 200 µA at 1 MHz Idle mode: 25µA at 1 MHz Power-down mode: < 0.1µA ADC: 200-400 µA
Footprint	3×3x0.55 mm^3	2.0x1.61x0.56 mm^3 / 3x3x0.65 mm^3	1.55x1.41x0.538 mm^3
Package	QFN20	WLCSP / QFN	12-WLCSP
Volt. Supply	1.8 - 3.6 V	1.7 - 3.6 V	1.8 - 5.5 V
Clock Sources	- Internal 24.5 MHz high power oscillator (300 µA) - Internal 22 MHz low power oscillator (100 µA) - Internal 16.4 kHz RT oscillator (< 1 µA) - External clock	- 48 MHz high accuracy internal clock - 8/2 MHz low power internal clock - 32 kHz to 40 kHz crystal oscillator - 1 kHz LPO clock	- Internal 128 kHz clock - Internal 8 MHz clock - External clock
Temperature Sensor	Yes	Yes	Yes
Memory	8 kB flash, 512-byte RAM	32 kB flash, 2kB RAM	2 kB flash, 128-byte RAM
ADC	12-bit	12-bit	10-bit
Capacitive Sensing	Yes (1 fF resolution, 45 or 500 pF max load)	No	No (capacitive touch sensing library available)
Unit Cost (for 1 pc / 5000 pcs)	$0.97 / <$0.89	$2.308 / $1.703	$1.50 / $0.655

2.1.4 Silicon Labs BGM121 MCU

For this work, the BGM121 MCU from Silicon Laboratories, Inc. [Sil19] is selected over other options for B-MCU. It has an integrated antenna and a reasonable footprint. Chips without integrated antenna must use commercial antenna or antenna implemented on PCB, typically requiring larger footprint. The BGM121 also has low standby current. It is manufactured by the same company as the S-MCU, allowing better compatibility between these chips. Table 2.3 compares the key parameters of BGM121 along with other MCUs that were considered.

Table 2.3: Comparison of MCUs for B-MCU

Chip	TI CC2650 MODA	SiLabs BGM121	Broadcom BCM20737
On-Chip Flash	128 kB	128-256 kB	No
On-Chip Data Bus	UART, I^2C	UART, I^2C, SPI	UART, I^2C
Integrated Antenna	Yes	Yes	No
Active Current	R_x: 6.2 mA T_x (0 dBm): 6.8 mA	R_x: 9.0 mA T_x (0 dBm): 8.2 mA	R_x: 9.8 mA T_x (0 dBm): 9.1 mA
Standby Current	1 µA	2.5 µA	12 µA
Footprint	16.9 × 11 mm^2	6.5 × 6.5 mm^2	5 × 5 mm^2

The selected B-MCU, i.e., SiLabs BGM121, can be operated in various energy modes. The energy mode to be used for depends on the desired system function and current consumption values. It is desirable to operate the B-MCU in the energy mode with lowest current consumption while meeting the function requirements. The B-MCU is, therefore, placed in the low power mode for most of the operation time when I^2C or BLE functions are not being used, including the entire period when the system is deployed. Active mode is required to operate the BLE radio and all the BLE functions; this mode is used during active BLE communication. The BLE radio is also off in the intervals between the advertising, connection, or data transfer events to further save power. The S-MCU is placed in deep sleep mode during this time. The energy modes with their functions are summarized in Table 2.4.

Table 2.4: B-MCU energy modes, current consumption, and functions

Energy Mode (EM)	Current at RT	Function
EM0: Active	63 µA /MHz	Needed while tasks are running on the processor and/or radio is receiving/transmitting
EM1: Sleep	32 µA /MHz	Needed if there are no tasks running and no radio communication, but some peripheral is active that needs this mode
EM2: Deep sleep	2.5 µA	This is the ideal mode for the device to be in to maintain working of the stack, when there is no need for higher energy modes
EM3: Stop	2.1 µA	The Bluetooth stack does not work in this mode. However, if there are no connections alive, and no advertisement/scanning is needed for a while, the device can be put into this mode to save energy
EM4: Low power/ Shutoff	0.04 µA	If the application does not need any operation for a while, the device can be put in either of these modes; nearly everything is shut down and to wake up the device from this state a reset is needed

2.1.5 *Selection of Communication Protocol for Data Transfer between S-MCU and B-MCU*

There are several standard protocols available for communication between the S-MCU and B-MCU, including Serial Peripheral Interface (SPI), Universal Asynchronous Receiver/Transmitter (UART), and I^2C. I^2C is chosen as the communication protocol. It requires only two wires for communication and is straightforward to implement. It also allows multiple masters and/or slaves on the communication bus, making it possible to add additional digital sensors/MCUs to the system in the future. The options are compared in Table 2.5.

Table 2.5: Comparison of communication protocols

Feature	SPI	UART	I^2C
Number of wires	4	2	2
Clock signal	Yes	No	Yes
Multiple masters/slaves	No/Yes	No/No	Yes/Yes
Data frame size	Continuous data streaming (no start and stop bits)	9 bits	8 bits
Advantages	Higher data transfer rate than I^2C (almost twice as fast)	Parity bit to allow for error checking	ACK/NACK bit gives status of transferred frames

2.1.6 *MEMS Pressure Sensor*

The capacitive MEMS pressure sensor was developed at the University of Michigan[1]. The sensing diaphragm is composed of a dielectric stack of SiO_2, Si_3N_4, and Al_2O_3 measuring 5 µm thick with an inter-electrode sensing gap of 450 nm. The sensing electrodes are composed of aluminum and insulated with Si_3N_4 to permit touch-mode operation. Sapphire has been selected as the substrate material due to its good thermal expansion coefficient match with the dielectric diaphragm. The sensors have a typical size of $1.8 \times 1.5 \times 0.5$ mm^3. They show a full-scale range of 0-70 MPa (0-10,000 psi) with an average response of 0.5 fF/kPa (3.3 fF/psi). A pressure resolution of 2 kPa (0.3 psi) is achieved when the C8051F990 capacitive sensing module is utilized (with a capacitance resolution of 1 fF/code). Figure 2.4 shows an optical image of the pressure sensor.

[1] Pressure sensor was developed by Dr. Alexander Benken [Ben19].

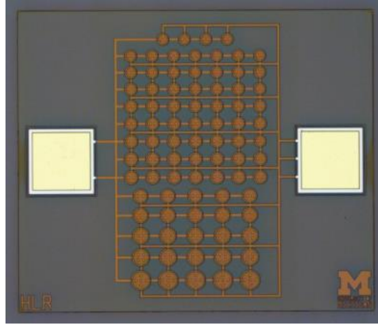
Figure 2.4: Optical image of the pressure sensor.

2.1.7 *Inertial Measurement Unit*

For this work, inertial sensing is achieved by integration of a 6-axis IMU, LSM303C, from STMicroelectronics [STM14]. This IMU includes a 3-axis accelerometer and a 3-axis magnetometer for the measurement of acceleration and rotation, respectively. These inertial parameters potentially can be used for coarse geolocation and tracking of the system in the pipeline environment. The IMU has a footprint of 2×2×1 mm^3, static current consumption of 6 µA and an active current consumption of 270 µA with both sensors on. The IMU supports both the SPI and I^2C protocols for digital communications with the MCU. In the detection state, inertial sensor measurements are made by the IMU and received by the S-MCU using I^2C bus. Gyroscopes, which represent another common sensor category for rotation measurement, were not selected because of much higher current consumption (usually >1 mA) [Huy09].

2.1.8 *Bluetooth External Unit*

A Bluetooth external unit is required at the user end for wireless communication (data and commands) with the B-MCU in ELM6. The overall system is represented in Figure 2.5. The external unit hardware is a Raspberry Pi™ (RPi) (Raspberry Pi Foundation, United Kingdom) with an integrated Bluetooth module (Figure 2.6) as detailed in Table 2.1.

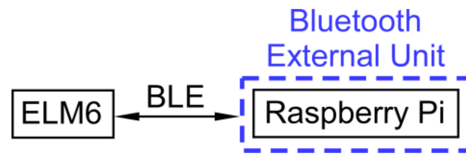

Figure 2.5: Overall system representation for ELM6.

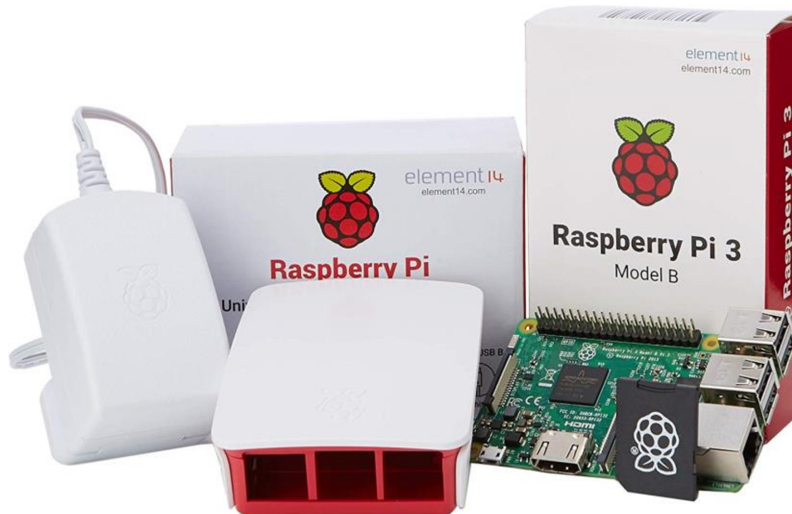

Figure 2.6: Bluetooth external unit hardware [Ras20].

2.2 System Software

The software for the system has been developed to permit low power operation and limit memory usage. The typical operation flowchart for the system is shown in Figure 2.7. This provides the basis for the development of the system software. The S-MCU and B-MCU are both initialized after power on. When the system is ready for deployment, S-MCU is placed in the detection state and B-MCU is placed in the lowest energy mode, i.e., low power/ shutoff state. B-MCU remains in the low power state throughout the deployment if not used. However, if the S-MCU flash memory becomes full, the B-MCU is woken up by the S-MCU, all the data stored in the S-MCU flash memory is transferred to the B-MCU via I^2C protocol, and the B-MCU is placed back in the low power state. At the end of the deployment, once the system is retrieved, it is charged and triggered out of the detection state by the user. When the data transfer is requested

by the user, S-MCU transfers sensor data to the B MCU through the I^2C bus. After data transfer, the S-MCU enters deep sleep. B-MCU reports the data to the user through the BLE link.

The software for the system includes two parts: software for S-MCU and software for B-MCU. The state diagrams for both the MCUs are described in detail in this section.

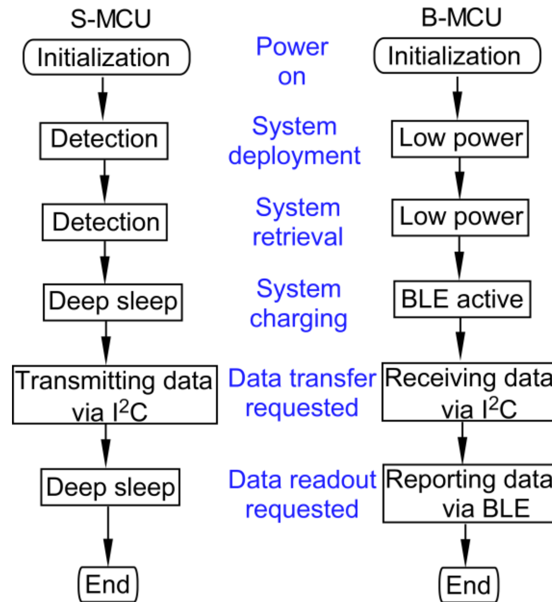

Figure 2.7: Typical operation flowchart for ELM6.

2.2.1 S-MCU Software State Diagram

The software state diagram for the S-MCU is shown in Figure 2.8. The user communicates various commands to S-MCU via B-MCU using BLE protocol, B-MCU sends these commands to the S-MCU through I^2C protocol, and S-MCU transitions to the required state and performs the function. The functions of individual states are explained below.

State A1, S-MCU power off state:

This is the state of the S-MCU when the battery voltage is very low, typically <2.4 V (V_L), to power the system. The system enters this state typically after operations. The S-MCU remains off in this state. Data is retained in the S-MCU flash memory without loss.

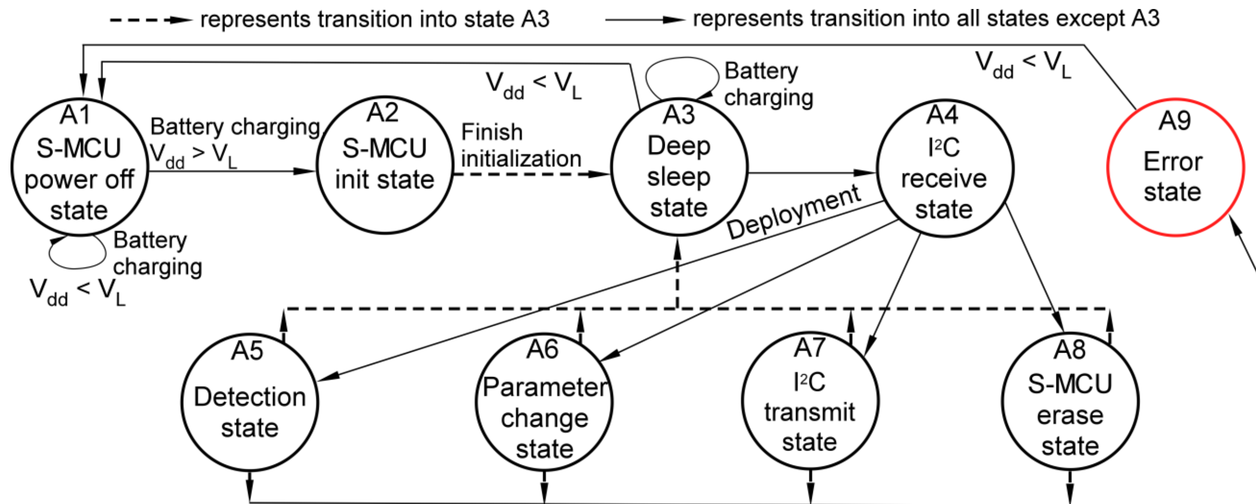

Figure 2.8: S-MCU state diagram for ELM6.

State A2, S-MCU init state:

This is a transient state during which the S-MCU turns on and all global constants and variables are initialized or restored from the flash memory. Registers of pertinent S-MCU peripherals, e.g. ADC, digital I/O, etc., are initialized for use in later operations.

State A3, Deep sleep state:

This is the state when the S-MCU is on but in the deep sleep mode to minimize power consumption. The system enters this state after finishing the initialization, or after finishing data collection or data transmission operations. This is also the state of the S-MCU during wireless battery charging operation.

State A4, I^2C receive state:

This is the state in which the S-MCU receives commands from B-MCU through I^2C protocol. When the user requires S-MCU to carry out a specific function, the user communicates this to B-MCU via BLE as the user cannot directly communicate with S-MCU. Following this, B-MCU wakes up S-MCU from deep sleep using port match functionality. A software-controlled value stored in a specific register specifies the value expected or normal logic value of a designated

S-MCU port. A port mismatch event occurs if the logic levels of the designated port's input pins no longer match the software- controlled value. Port match functionality uses this event is used to wake S-MCU from deep sleep. On waking up, S-MCU transitions to I^2C receive state and B-MCU transmits the command corresponding to the function required by the user via I^2C protocol. Depending on the command received, S-MCU can either transition to A5 (detection state), A6 (parameter change state), A7 (I2C transmit state), or A8 (S-MCU erase state).

State A5, Detection state:

This state performs the temperature, pressure, and inertial data measurement with a predefined schedule. This schedule can be reprogrammed by modifying the global constants in the software using parameter change state. Figure 2.9 shows the sub-states in this state. When the S-MCU transitions to this state, it enters the deep sleep mode (State A5.1) to conserve power and wakes up according to the predefined schedule to take sensor measurements. In the sensor measure state (State A5.2), the S-MCU stores temperature sensor data from the integrated temperature sensor, pressure sensor data from the MEMS pressure sensors through the CDC, and the inertial sensor data received from the IMU through I^2C protocol. For I^2C communication with the IMU, S-MCU is the master and IMU is the slave device. When the S-MCU flash memory becomes full in the detection state, all the sensor data stored in its flash is transferred to the B-MCU using I^2C communication (State A5.3) and the flash memory of S-MCU is erased (State A5.4) to open up space for new measurements. Following this, the S-MCU continues to measure sensor data (State A5.2) according to the predefined schedule.

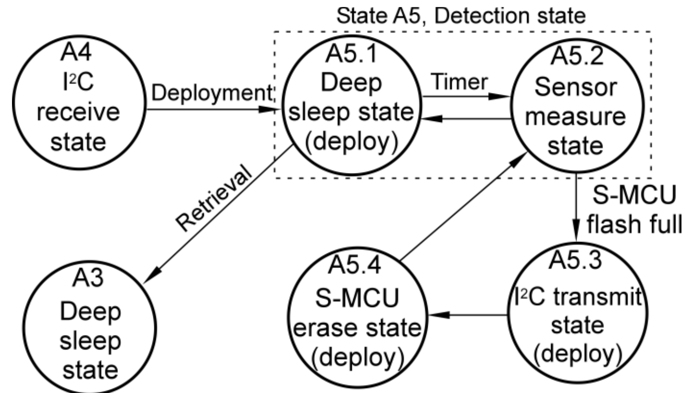

Figure 2.9: Diagram of sub-states for state A5, detection state.

State A6, Parameter change state:

This state allows the user to modify system operation parameters such as the measurement interval during detection. The measurement interval determines how frequently the system wakes up and takes measurements. Increasing the measurement interval would save system power but reduce the time resolution of the measurement. It also allows the user to select which sensor to be activated in the detection state, or to select both pressure sensor and IMU. The new parameters are entered into the Bluetooth external unit software interface by the user and transmitted to the B-MCU using BLE protocol. These parameters are then transmitted to the S-MCU by the B-MCU using I^2C communication.

State A7, I^2C transmit state:

This is the state in which the S-MCU transmits sensor data stored in its flash memory to the B-MCU using I^2C. The S-MCU is the master and the B-MCU is the slave for I^2C communication. In this state, the S-MCU transmits data packets along with the cyclic redundancy check (CRC) error check bits to the B-MCU. The S-MCU transitions to this state in two scenarios. The first scenario is when the S-MCU flash memory is full in the detection state (state A5). In this scenario, the S-MCU wakes up B-MCU to transfer the stored sensor data via I^2C. This is because the B-MCU has a large flash memory, 256 kB compared to 8 kB of S-MCU. The second scenario

is when the user requests data to be transferred from S-MCU to B-MCU via I^2C, before data readout through BLE.

State A8, S-MCU erase state:

This state allows the user to erase the temperature, pressure, and inertial measurement data stored in the flash memory of S-MCU to open up storage space for new measurements. This state is entered when the S-MCU flash memory is full during deployment or when the user chooses to erase the flash memory after transferring all the data to the B-MCU.

State A9, Error state:

This is the "catch-all" state which the S-MCU enters if the program should fail unexpectedly and stop execution. Once it enters this state, it needs to wait for the battery voltage to drop below V_L so that the system power is turned off. At that point, the S-MCU goes to State A1 and the battery can be recharged.

2.2.2 B-MCU Software State Diagram

The software state diagram for the B-MCU is shown in Figure 2.10. The B-MCU is powered on, initialized and moved into the Bluetooth connection state after initialization. In this state, it is ready to connect to the user via BLE and can perform functions determined and sent as commands by the user via BLE. It transitions to the state corresponding to the function to be performed. Functions involving B-MCU only, for example the battery check state (state B8) and the B-MCU erase state (state B6) will be performed directly after receiving command over BLE. For functions involving S-MCU, B-MCU transitions to I^2C transmit state (state B9) on receiving command for a specific function over BLE and sends this to the S-MCU via I^2C. The B-MCU is placed in the low power state (state B4) when the system is deployed or when the system is not in use. The functions of the individual states of B-MCU are explained below.

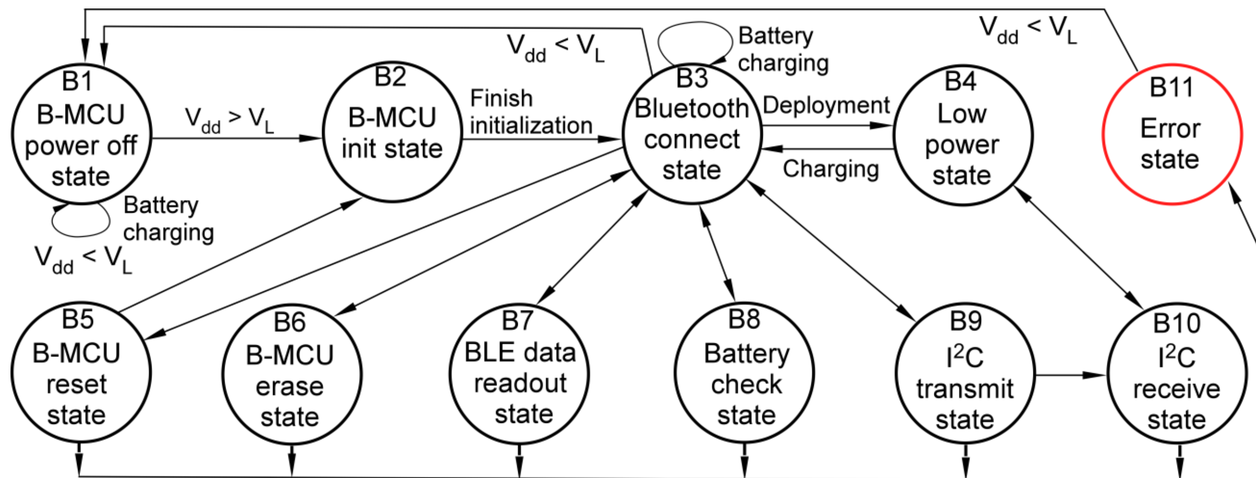

Figure 2.10: B-MCU State Diagram for ELM6.

State B1, B-MCU power off state:

This is the default state when a sensing program is not running and the battery is not being charged, and its voltage (V_{dd}) is below a certain threshold voltage, typically <2.4 V (V_L). The system typically enters this state after operations. The B-MCU remains off in this state. Data is retained in the B-MCU flash memory without loss.

State B2, B-MCU init state:

This is a transient state during which the B-MCU turns on and all global constants and variables are initialized or restored from the flash memory. Registers of pertinent B-MCU peripherals, e.g. I^2C, digital I/O, etc., are initialized for use in later operations. The radio is turned on briefly and the Bluetooth stack is initialized.

State B3, Bluetooth connect state:

This is a transitional state when the B-MCU advertises and waits for Bluetooth connection request from the client. Once connected to the client (external unit), the user can choose either to place it in low power state (state B4), reset B-MCU (state B5), erase B-MCU flash memory (state B6), transfer data via BLE (state B7), check system battery level (state B8), or transmit commands to S-MCU (state B9). These states are described below.

State B4, Low power state:

This is the state when the B-MCU is on but in shutoff mode to minimize power consumption. This is the state in which the B-MCU is placed when the system is deployed or when the system is not in use. A reset signal is needed to wake up the B-MCU from this state. There is no status information retained from the previous operation and the Bluetooth stack is reinitialized.

State B5, B-MCU reset state:

This state allows the user to manually reset the system should any unexpected behavior occur, such as a clock source oscillating at an unexpected frequency.

State B6, B-MCU erase state:

This state allows the user to erase the temperature, pressure, and inertial measurement data stored in the flash memory of B-MCU to open up storage space for new measurements.

State B7, BLE data readout state:

This is the state when the B-MCU transmits sensor data to the external unit. The B-MCU reads the stored data from its flash memory and sends them as data packets to the external unit through the BLE link. BLE uses cyclic redundancy check (CRC) error check bit and automatically corrects erroneous data packets by resending.

State B8, Battery check state:

This is the state when the B-MCU checks for the battery level and reports it to the user over BLE.

State B9, I^2C transmit state:

This is the state in which the B-MCU transmits various commands to the S-MCU via I^2C. First, the user communicates to the B-MCU via BLE the various commands that are to be sent to

the S-MCU. The B-MCU then transitions to this state and sends the commands to the S-MCU through the I^2C bus.

State B10, I^2C receive state:

This is the state in which the B-MCU receives sensor data from the S-MCU through the I^2C bus. The B-MCU is the slave and the S-MCU is the master for I^2C communication. In this state, the B-MCU receives data packets along with the cyclic redundancy check (CRC) error check bits and writes the received data to its flash memory. The B-MCU transitions to this state in two scenarios. The first scenario is when the S-MCU flash memory is full in the detection state (state A7). In this scenario, the S-MCU wakes up B-MCU to transfer the stored sensor data via I^2C. This is because the B-MCU has a large flash memory, 256 kB compared to 8 kB of S MCU. The second scenario is when the user requests data to be transferred from S MCU to B-MCU via I^2C, before data readout through BLE.

State B11, Error state:

This is the "catch-all" state which the system enters if the program should fail unexpectedly and stop execution. Once the system enters this state, it needs to wait for the battery voltage to drop below V_L so that the system power is turned off. At that point, the system goes to State 1 and the battery can be recharged.

2.2.3 I^2C Communication

The I^2C protocol is a standard communication protocol used to transfer data between two digital devices. The device which initiates the transfer, determines the I^2C clock frequency, and controls the I^2C bus is the master; the device which responds to the master is the slave. In this system, the S-MCU is the master and the B-MCU is the slave. The operation flow for I^2C communication is as follows: the S-MCU reads pressure, temperature, and inertial sensor data

stored in its flash memory and sends these to the B-MCU over the I^2C bus; the B-MCU receives the data over I^2C bus and writes the data to its flash memory.

I^2C communication is initiated by the S-MCU once the user requests for data transfer between the S-MCU and the B-MCU. Each I^2C slave has a 7-bit address that needs to be unique on the bus. The S-MCU initiates I^2C communication by sending a start bit, B-MCU address and a '0' or '1' bit; here '0' indicates 'write' and '1' indicates 'read'. Once the B-MCU acknowledges its address, the S-MCU sends a set of data bytes followed by cyclic redundancy check (CRC) bytes. The B-MCU then computes CRC for the data bytes it receives. If the CRC does not match, the B-MCU sends 'not acknowledge' (NACK) bit to the S-MCU and the S-MCU resends the data; if the CRC matches, the B-MCU sends 'acknowledge' (ACK) bit to the S-MCU and the S-MCU sends the next set of data bytes. This process continues till all the data is sent from the S-MCU to the B-MCU.

2.2.4 Issues Addressed During Development of B-MCU Software

There were a number of software-related issues (bugs) in the B-MCU development tool provided by the manufacturer. Some of the issues addressed are described in this section.

A. Issues related to I^2C communication code:

The B-MCU is expected to handle I^2C events in the following way: when the S-MCU requests the B-MCU for I^2C communication, the B-MCU generates an interrupt to break from its main program, serves the I^2C request by processing it through the I^2C interrupt handler, and then returns to the main program after serving the request. However, during software testing, it was found that although the B-MCU was able to receive all data packets as expected, it was not able to serve the interrupt by implementing the interrupt handler. This resulted in a hard fault in the B-MCU, leading it to implement the hard fault handler instead of the I^2C interrupt handler. This issue was resolved by initializing the Bluetooth stack before starting I^2C communication. Since

the B-MCU is a Bluetooth based MCU, the stack needs to be initialized in the code even though it is not directly related to I^2C communication.

B. Issues related to wake-up from low power mode:

To save energy, the B-MCU is placed in low power mode for most of the time when the system is powered on. It must be woken up by the S-MCU to perform two independent functions: 1) data transfer from the S-MCU to the B-MCU through I^2C, and 2) connection to the external unit via BLE. The B-MCU needs to differentiate these two causes of wake-up; therefore, two separate wake pins are necessary. This configuration was initially implemented following instructions in the datasheet. However, the software did not work and only one general purpose input output (GPIO) wake pin was functional. After communicating with the manufacturer engineers, a software bug in the MCU energy management module was identified, which prevented the usage of two different GPIO pins for wake-up. Hence, the software configuration was modified by using a single GPIO pin and configuring the reset pin to indicate the cause of wakeup.

C. Issues related to B-MCU development PCB:

A development PCB from the manufacturer was used to develop and test the software for the B-MCU. When the B-MCU was operated in low power mode using a regular procedure, it would stop being operational (bricked). This problem was resolved by manually erasing the flash memory using a special procedure.

To download software and test the B-MCU mounted on a protoboard, a Cortex debug connector was used to connect the development PCB to the protoboard. However, the latest firmware of the development PCB prevented downloading and debugging software into the B-MCU on the protoboard. This issue was resolved by downgrading the firmware of the development PCB to a lower version.

2.2.5 Bluetooth External Unit Software

The software for the Bluetooth external unit consists of graphical user interface (GUI) software and backend software for the Bluetooth module of RPi, both built using Python programming language (Python Software Foundation, Delaware, USA).

The GUI is shown in Figure 2.11. The GUI software is built using Tkinter package (Python Software Foundation, Delaware, USA) of Python language. The main window of the interface consists of six sections: 1) BLE connection control and status, 2) system information and status, 3) battery status, 4) S-MCU commands, 5) B-MCU commands, and 6) sensor data plots. The backend software for the Bluetooth module of RPi is built using the *pygatt* module (Python Software Foundation, Delaware, USA) of Python. A screenshot of the interface during communication with ELM6 is shown in Figure 2.12. The serial number of the system along with BLE connection status and system message are displayed in section (2). The list of available BLE devices nearby is displayed after scanning (Figure 2.12(b)). All unrecognized devices are displayed as “None”. The functions of each section in the GUI are described in Table 2.6.

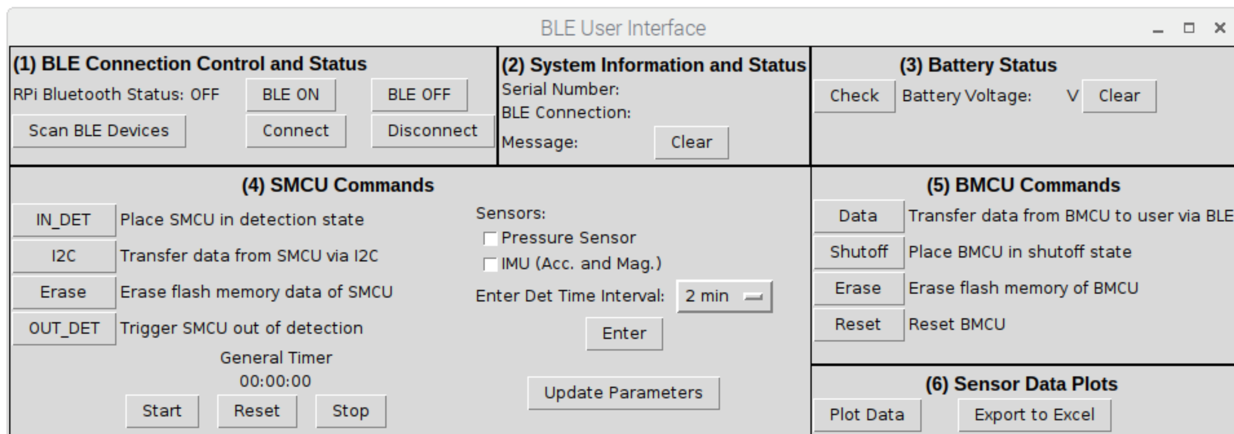

Figure 2.11: Graphical user interface of Bluetooth external unit.

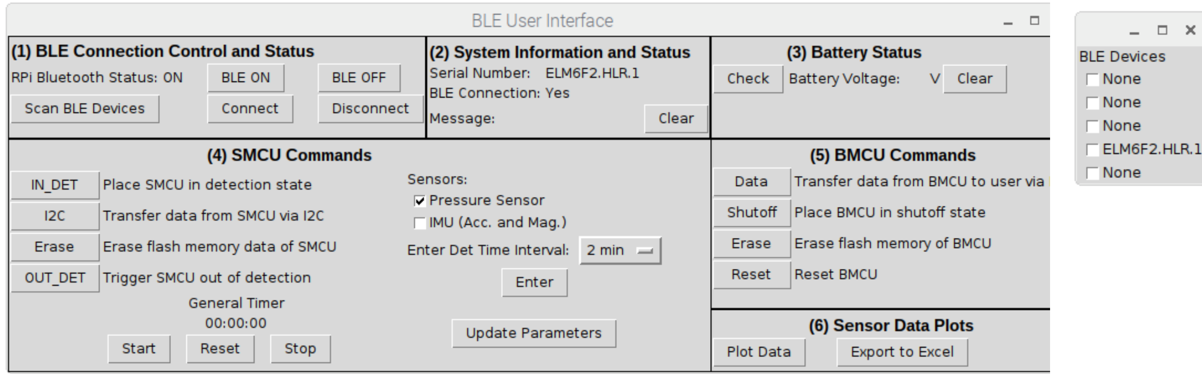

(a) (b)

Figure 2.12: Screenshot of interface during communication with ELM6. (a) The serial number of the system along with BLE connection status and system message are displayed in Section (2). (b) The list of available BLE devices nearby is displayed after scanning; unrecognized devices are displayed as “None”.

Table 2.6: List of sections with their functions on the GUI

No.	Section	Functions
1.	BLE Connection Control and Status	• Allows the user to turn on/off Bluetooth on RPi • Allows the user to scan available BLE devices nearby • Allows the user to select the device for BLE connection and establish/terminate connection
2.	System Information and Status	• Displays the serial number of the connected ELM6 system • Displays the status of BLE connection • Displays status of the system as a result of any command sent by the user. It contains “Clear” button to clear the message
3.	Battery Status	• Displays the battery voltage of the device
4.	S-MCU Commands	• Allows the user to communicate various commands to the S-MCU via the B-MCU • Allows user to select the sensors and choose the detection time interval • Contains a general timer to record the total time in which the system has been in detection state
5.	B-MCU Commands	• Allows the user to send commands to the B-MCU
6.	Sensor Data Plots	• Provides user the graphical plot of sensor data • Allows the user to export data into an excel sheet

2.3 System Integration and Fabrication

The system components are integrated on a flexible PCB and then folded into a stack to reduce the overall system volume. The flexible polyimide PCB is fabricated and assembled by a commercial PCB manufacturer. The polyimide used for the PCB is DuPont® Pyralux AP, which has a maximum elongation of >50% after curing. This elongation is enough for the board to fold 180°C without damaging the material and metal traces [Sui17]. All components (excluding the

pressure sensor) are assembled on the PCB using a commercial assembly service from the PCB manufacturer. The pressure sensor is assembled in-house using conductive Duralco 120 silver epoxy (Cotronics Corp). Figure 2.13 shows the PCB layout of the polyimide PCB. The overall length and width of unfolded PCB are 43.0 mm and 14.2 mm respectively. The PCB includes a top and a bottom metal layer.

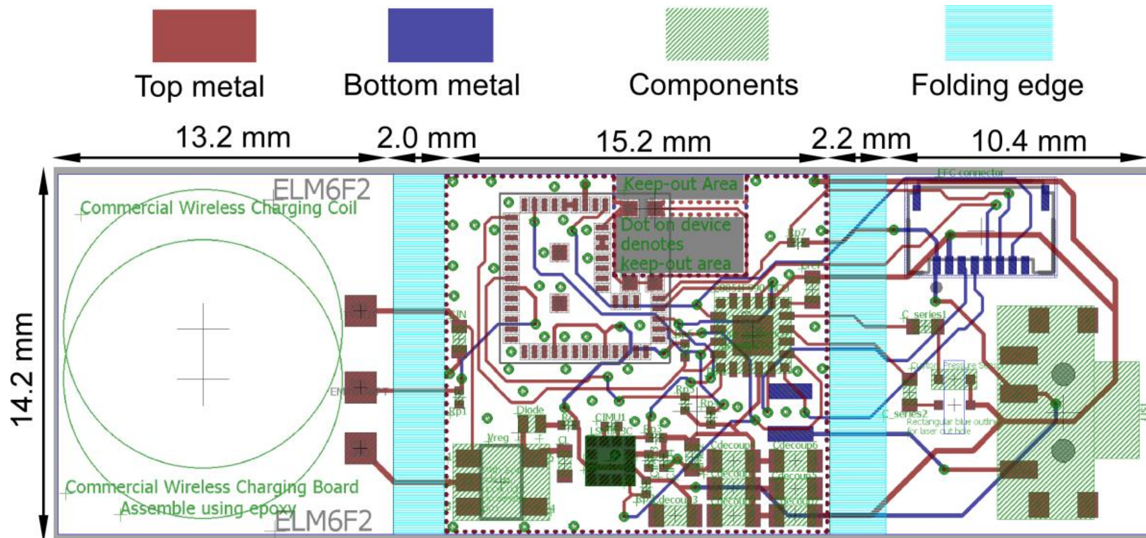

Figure 2.13: Layout of the foldable polyimide PCB (L×W: 43.0 mm ×14.2 mm).

The PCB can be used in an unfolded or folded arrangement. Figure 2.14(a) shows the configuration of the system stack after the polyimide PCB is folded. The folded stack contains five layers in total. The first layer is the receiver for wireless charging. The receiver coil is placed on top to permit wireless charging of the battery. The second layer is the sandwiched battery. The third layer is the charging circuit, two MCUs, IMU, and passive components. The fourth layer contains the slide switch and MEMS pressure sensor. An opening is cut on the PCB beneath custom pressure sensor so that the diaphragm is exposed to the exterior pressure. The fifth layer contains a surface mount connector, used to connect the MCU programming pins to an external debugger for programming the MCUs. The thickness of the polyimide PCB is 730 μm in the component area and 200 μm in the fold. An extra 508 μm 85N rigid stiffener is added to the

component area to further stabilize the components and prevent the soldered pins from breaking during the folding process. The overall designed stack size is 15.4×14.2×11.2 mm^3 (L×W×H). The PCB can be hermetically encapsulated to survive the high pressure and high temperature (HPHT) environment. The folded system can be encapsulated in a transparent polymer and packaged in a shell made up of a material compatible with RF communication such as ceramic, similar to the method described in [Ma16] (Figure 2.14(b)). The system can also be unfolded and then encapsulated in a polymer mold for protection as described in [Sui17] (Figure 2.14(c)). The polymer material helps transfer the external pressure to the pressure sensors with low attenuation.

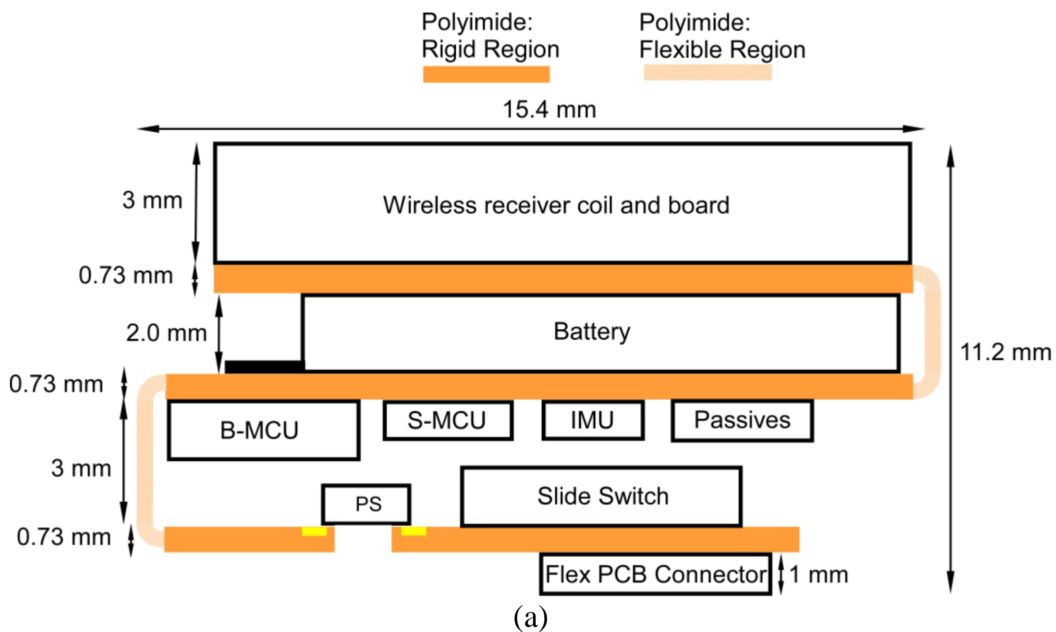

(a)

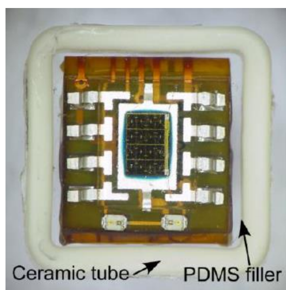

(b)

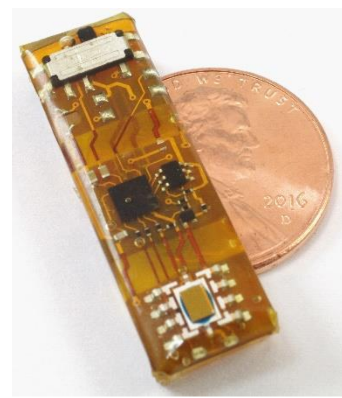

(c)

Figure 2.14: (a) Design of flexible PCB stack; (b) folded ELM2 PCB packaged in ceramic tube [Ma16]; (c) unfolded ELM3 PCB packaged in polymer mold [Sui17].

The photos of the manufactured ELM6 flexible PCB are shown in Figure 2.15. All components, including the wireless receiver board and coil are integrated on top of the PCB (Figure 2.15(a)), battery and flex PCB connector are integrated on the bottom side (Figure 2.15(b)). Major components labelled in the figure are detailed in Table 2.7.

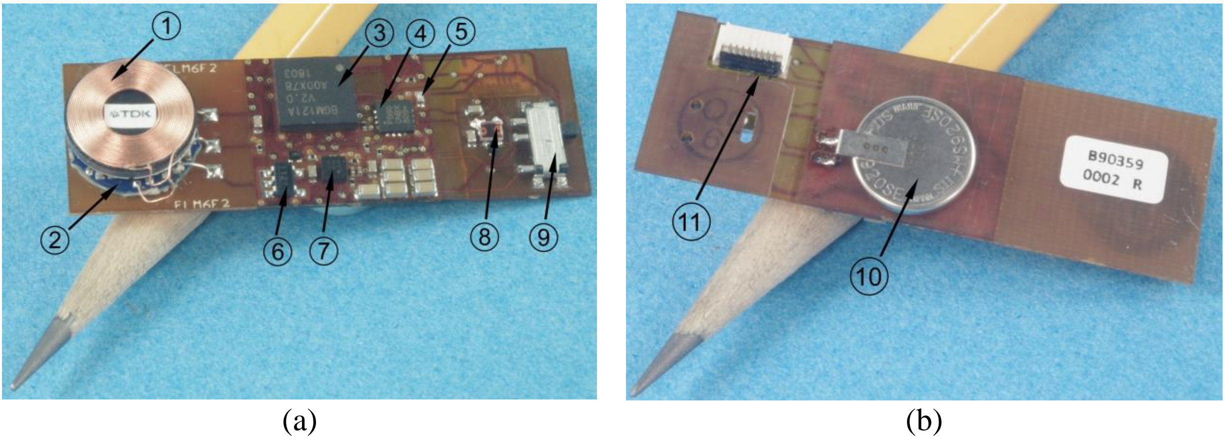

(a) (b)

Figure 2.15: Photos of the manufactured ELM6 flexible PCB: (a) top and (b) bottom view.

Table 2.7: Major components of ELM6 flexible PCB

No.	Component	Function
1.	Wireless receiver coil	Used for Qi charging
2.	Wireless receiver board	Receives power wirelessly using Qi protocol
3.	Bluetooth-microcontroller unit (B-MCU)	Receives sensor data from S-MCU and sends it to the Bluetooth external unit using the Bluetooth low energy (BLE) protocol
4.	Sensor-microcontroller unit (S-MCU)	Executes system functions including data acquisition, communication with IMU and B-MCU, data storage, etc.
5.	Reference capacitor	Capacitor with no pressure response and negligible temperature coefficients. The measured value is used for calibration purposes
6.	Voltage regulator	Used to regulate battery voltage
7.	Inertial measurement unit (IMU)	Consists of an accelerometer and a magnetometer and can be used for geolocation monitoring of the system
8.	Micromachined pressure sensor[2]	Custom fabricated sensor (HLR) for use up to 70 MPa (10.0 kpsi) static pressure
9.	Mechanical switch	Completely detaches the battery from the ELM6 circuit for increased shelf life. Switch is pictured in OFF position
10.	Battery	Lithium coin cell battery to power the system
11.	Debug connector	Used for programming the S-MCU and B-MCU

[2] Pressure sensor was assembled by Dr. Alexander Benken.

Table 2.8 summarizes the overall design parameters of the ELM6 system after integration. The electrical parameters were measured in the system characterization tests, which are explained in detail in Section 2.4.

Table 2.8: Overall design parameters of ELM6

Physical Parameters	
Unfolded PCB footprint	43.0 mm × 14.2 mm
Designed system stack size	15.4×14.2×11.2 mm^3
Integration topology	Polyimide flexible PCB
Electrical Parameters	
Upper limit of operating temperature	60ºC
Temperature resolution	0.5°C
Upper limit of operating pressure	10 MPa (1450 psi)
Pressure resolution	2 kPa (0.3 psi)
Acceleration range	±8 g
Acceleration resolution	0.244 mg/LSB
Magnetic field range	±16 gauss
Magnetic field resolution	0.580 mgauss/LSB
Battery max. voltage	3.1 V
Battery capacity & size	9 mAh Φ9.5 mm x 2.2 mm
BLE current peak (Data transfer, RT)	Rx: ≈13 mA and Tx: ≈11 mA
Peak system current (Standby, RT and 60ºC)	8.0 μA and 37.8 μA
Peak system current (Detection, RT and 60ºC)	93.3 μA and 129.5 μA
Peak system current (I^2C transfer, RT)	3.8 mA
Peak system current (S-MCU erase, RT)	3.5 mA
Peak system current (B-MCU erase, RT)	6.6 mA
Operating frequency	S-MCU: 32.768 kHz; B-MCU: 32.768 kHz (core), 38 MHz (BLE)
Total/data flash memory size	S-MCU: 8 kB/ 1.5 kB B-MCU: 256 kB/ 84 kB

2.4 Experimental Results

Tests of the ELM6 system were carried out in five stages: (a) Characterization of the system components and circuits; (b) Room temperature (RT) tests; (c) Pressure tests; (d) Temperature tests; (e) Combined pressure and temperature tests. Test results from (a), (b), (c), and (d) suggest that the system achieved all the intended functionalities for temperature, pressure, and inertial sensor measurement, wireless battery charging, low power operation, and wireless

communication. In step (b), the system lifetime was found to be >10 days when operated at room temperature with detection interval of 12 hours. In pressure test in step (c), the system was successfully tested by pressurizing it to 12 MPa and in temperature test in step (d), the system was successfully tested by ramping up the temperature to 65°C. In step (e), the system survived >1 h at up to 65°C and 12 MPa and reported the temperature and pressure data successfully.

2.4.1 Characterization of ELM6 Components and Circuits

The ELM6 system was characterized for full system functionality. The wireless charging of the system was characterized in two parts: the wireless power transfer between the transmitter and the receiver kits, and the wireless charging of the battery.

A. Wireless power transfer between transmitter and receiver

The wireless power transfer was verified between the transmitter and the receiver kits by powering the transmitter kit using a 5 V USB supply and aligning the receiver coil to the transmitter coil. The wireless power transfer was successfully verified between the transmitter and the receiver for a maximum distance of 2 mm between the coils.

B. Wireless charging of battery

The circuit for the wireless charging of MS920SE battery using constant voltage charging mode is shown in Figure 2.16(a). This circuit is a part of the overall circuit schematic (shown in Figure 2.2). A typical characteristic plot of the open circuit voltage (OCV) of a partially depleted MS920SE battery is shown in Figure 2.16(b). A stable OCV (>3 V) indicates that the battery is fully charged.

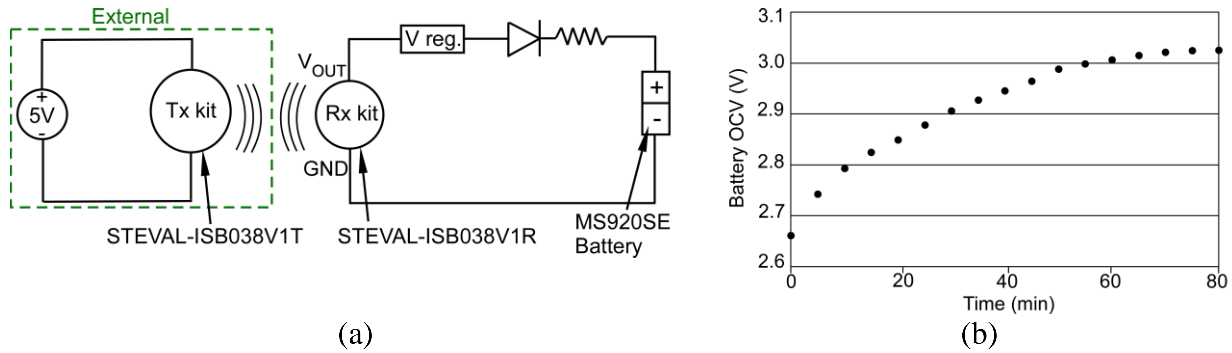

(a) (b)

Figure 2.16: ELM6 battery charging (a) circuit and (b) OCV plot.

C. B-MCU current characterization for BLE communication

The B-MCU current consumption during BLE communication was characterized as BLE communication is expected to consume the highest amount of current among all system functions. A detailed analysis of the current consumption of S-MCU along with other system components was carried out during the development previous ELM generations [Sui17].

The current consumption of B-MCU during BLE communication was experimentally measured at room temperature by sending data from the B-MCU. These tests were performed at room temperature to match to the intended application scenario where the user only needs the BLE communication after the system is retrieved from deployment for data readout.

The transient current of the B-MCU was measured using the readout circuit shown in Figure 2.17(b). The measurements were conducted with a DC power supply. The B-MCU current $I_{B\text{-}MCU}$ was converted to a voltage V_0 by a 1 Ω resistor R_S and amplified by an amplifier with a close loop gain of 68. The output voltage of the amplifier V_{sense} was recorded by an oscilloscope.

The measured transient current of the B-MCU during a typical BLE communication session is plotted in Figure 2.17(a). The BLE communication session typically consists of 3 modes that occur in sequence: advertising, handshaking, and data transfer. The plot of current consumption in each of the three modes is magnified and shown in Figs. 2.17(c)-(e), respectively, and is described below.

Advertising: B-MCU broadcasts advertising signals (i.e., an advertising event) approximately every 50 ms, resulting in repeating advertising peaks in the current plot. This continues until it receives a connection request from a client. During each adverting event, three frequency channels are used in series for sending the signal. There is one set of transmit (Tx) and receive (Rx) current peaks for each channel, resulting in a total of 6 peaks as shown in Figure 2.17(c). The measured transmit (Tx) current peak is 12.92 mA and receive (Rx) current peak is 13.52 mA. The total duration of a single advertisement event is 3 ms. Once the client responds to the advertising by sending a connection request, the B-MCU exits the advertising mode and transitions to the handshaking mode.

Handshaking: When the B-MCU (server) advertises, the client can request for connection by initiating the handshaking event. The client and server communicate back and forth during handshaking. The measured Tx current peak of the B-MCU is 11.88 mA and Rx current peak is 13.48 mA. The total duration of a single handshaking event is 2 ms, and this event can repeat several times depending on the communication settings.

Data Transfer: The data transfer mode follows the handshaking mode. The B-MCU sends data to the client during data transfer. The measured Tx current peak is 11.12 mA and Rx current peak is 12.94 mA. The total duration of a single data transfer event is 1.5 ms. This set of peaks occurs repetitively until all data transfer is complete.

D. Functional Tests

Functional characterization of proto-board implementations of the ELM6 system was used to validate the state machines. The I^2C communication was successfully tested between S-MCU and IMU; and between S-MCU and B-MCU. The Bluetooth functionality of the B-MCU was successfully verified; the battery voltage of ELM6 was accurately read out. The temperature, pressure, and inertial sensor data was successfully collected and readout using BLE.

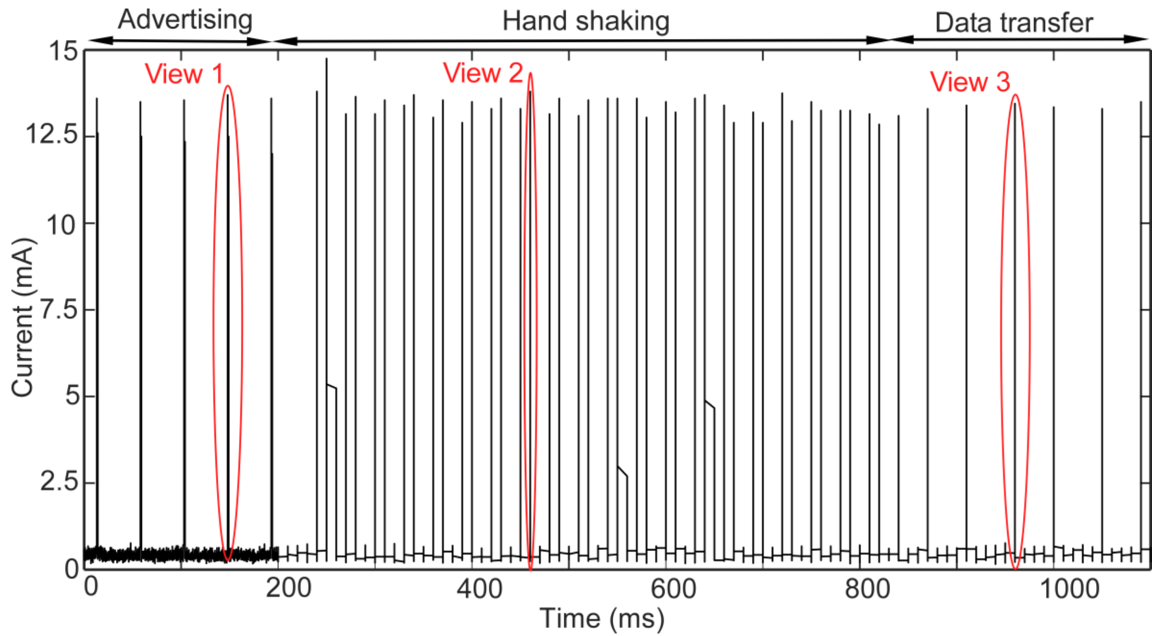

(a)

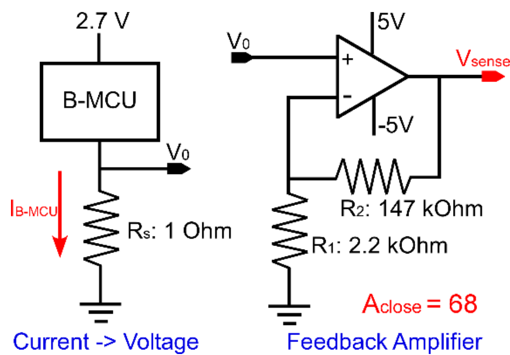

(b)

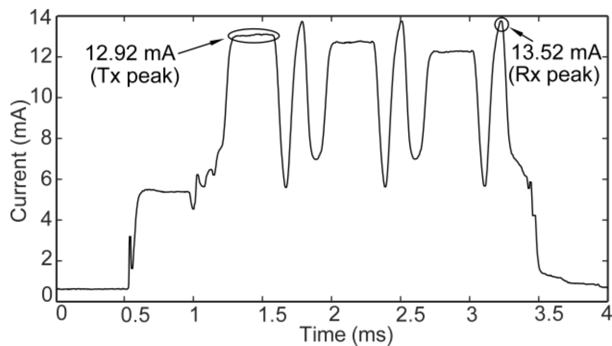

(c)

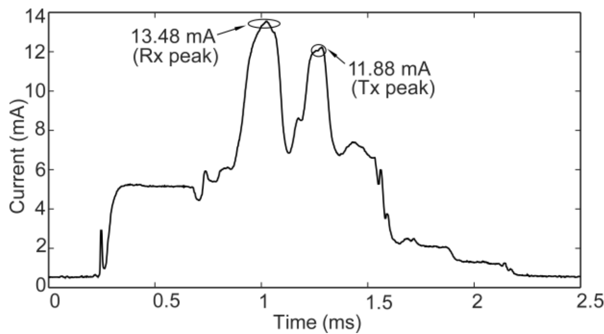

(d)

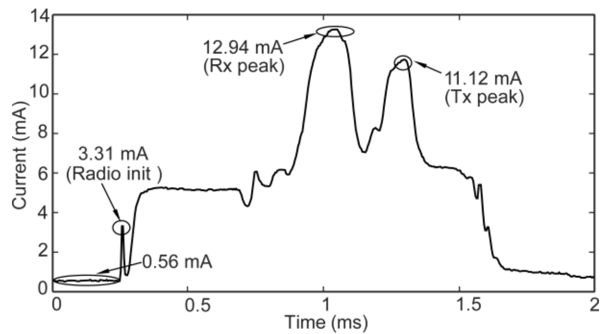

(e)

Figure 2.17: (a) Transient current consumption of B-MCU during BLE operation (b) Transient current measurement circuit (c) Magnified view during BLE advertising (View 1) (d) Magnified view during BLE handshaking (View 2) (e) Magnified view during BLE data transfer (View 3).

2.4.2 Room Temperature Tests of ELM6

Room temperature tests were conducted to verify full system functionality. Pressure, temperature, and inertial sensor data were successfully collected and read out for >24 hours with a detection time interval of 15 minutes.

The temperature and capacitance data recorded by ELM6 are shown in Figure 2.18(a). The reference capacitor is used for compensation of the offset in capacitance readout caused by the temperature effect of the S-MCU capacitance sensing module. The acceleration and magnetometer data recorded by ELM6 are shown in Figures 2.18(b) and 2.18(c) respectively. The system was turned upside down every 30 min for the first 2 hours, then at hour 8, hour 16, and hour 24. This is indicated by the Z-axis value of the acceleration in Figure 2.18(b).

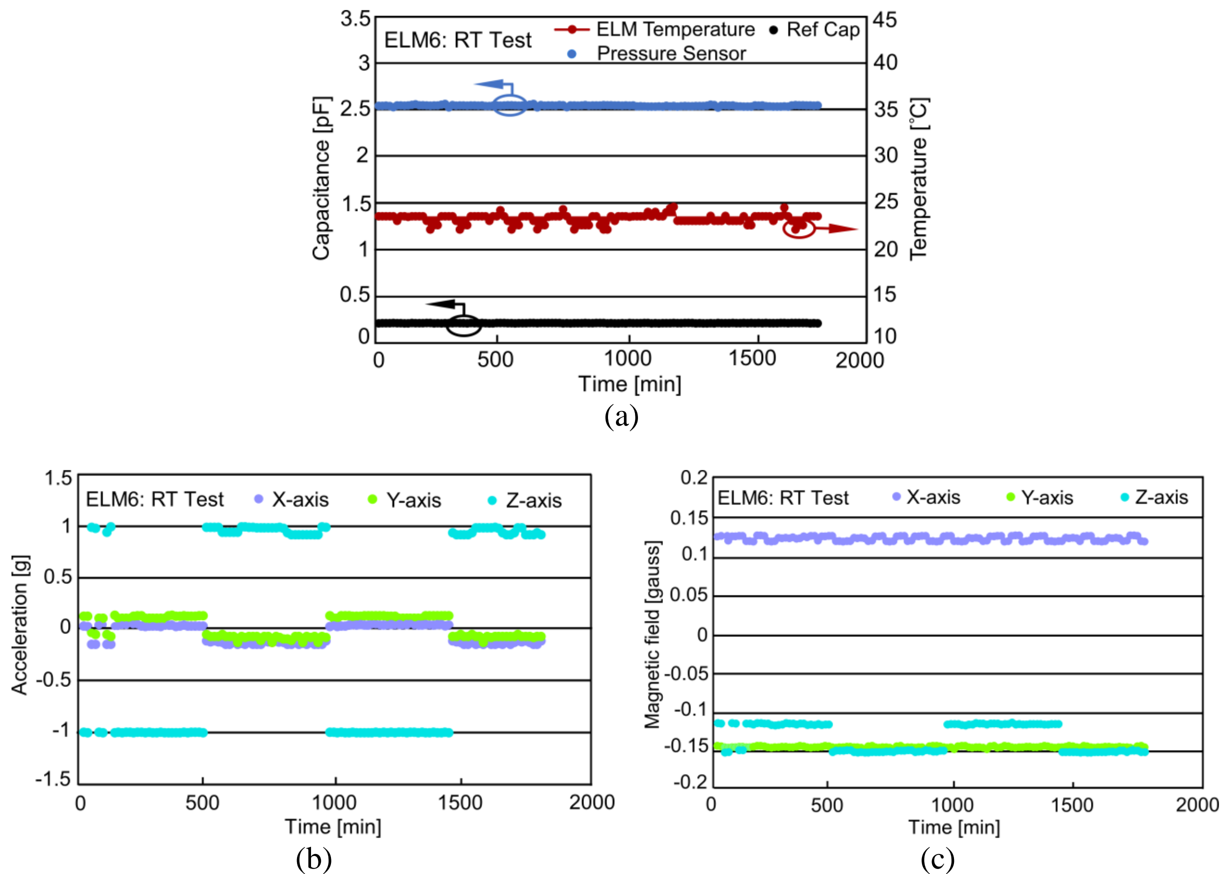

Figure 2.18: (a) Temperature (ELM Temperature) and capacitance (Pressure Sensor and Ref Cap); (b) Acceleration; and (c) Magnetic field data recorded by ELM6 during the room temperature test.

The system lifetime test of ELM6 was found to be >10 days at room temperature with a detection time interval of 12 hours. Since the system battery has a capacity of 9 mAh when the cut-off voltage is 2.4 V [Sei14], this suggests that the standby current of the system was 35 μA (neglecting the detection current as the system was in standby >99.9% of the time).

The temperature and capacitance data recorded by ELM6 during the lifetime test are shown in Figure 2.19(a). The acceleration and magnetometer data recorded by ELM6 are shown in Figures 2.19(b) and 2.19(c) respectively. The system was turned upside down every 24 hours. This is indicated by the Z-axis value of the acceleration in Figure 2.19(b).

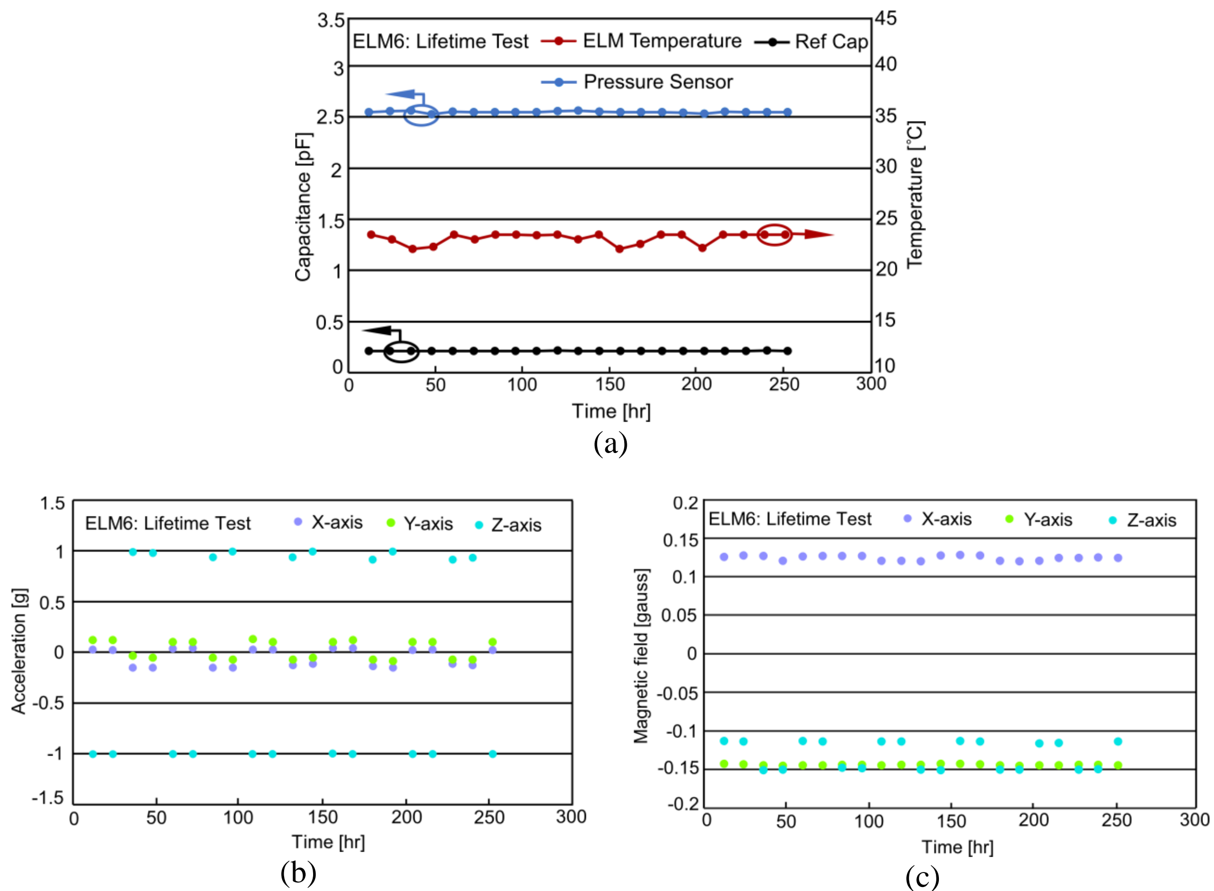

Figure 2.19: (a) Temperature and capacitance; (b) Acceleration; and (c) Magnetic field data recorded by ELM6 during the system lifetime test.

2.4.3 *Pressure Test of ELM6*

The pressure test was used to calibrate the pressure sensor of ELM6. The temperature and capacitance data recorded by the system during the pressure test are plotted in Figure 2.20(a). The pressure data was interpreted from the measured capacitances and temperature, using equation 2.1. It is a 3D polynomial that fits the temperature variation of the CDC module.

$$P_{interp} = b_1 + (b_2 \times T_{ELM}) + (b_3 \times \Delta C) + (b_4 \times \Delta C^2) + (b_5 \times \Delta C^3) + (b_6 \times T_{ELM} \times \Delta C) \quad (2.1)$$

where P_{interp} is the interpreted pressure, b_1 to b_6 are the calibration coefficients, T_{ELM} is the temperature recorded by ELM, and ΔC is the difference in capacitance recorded by the pressure sensor and the reference capacitor. The calibration coefficients are found based on least squares regression method to match the recorded capacitance data with the applied pressure. The temperature data recorded by ELM, interpreted pressure data recorded by ELM, and the tool pressure data are plotted in Figure 2.20(b). It is seen from this graph that the interpreted pressure matches very well with the tool pressure values. For the test, the system was placed inside a nylon bag filled with mineral oil and the bag was placed in a high pressure high temperature (HPHT) equipment from Applitech Consulting Corp. (Lancaster, PA, USA). The test was performed at pressure up to 12 MPa (1740 psi) for >20 minutes with data recorded every 2 minutes.

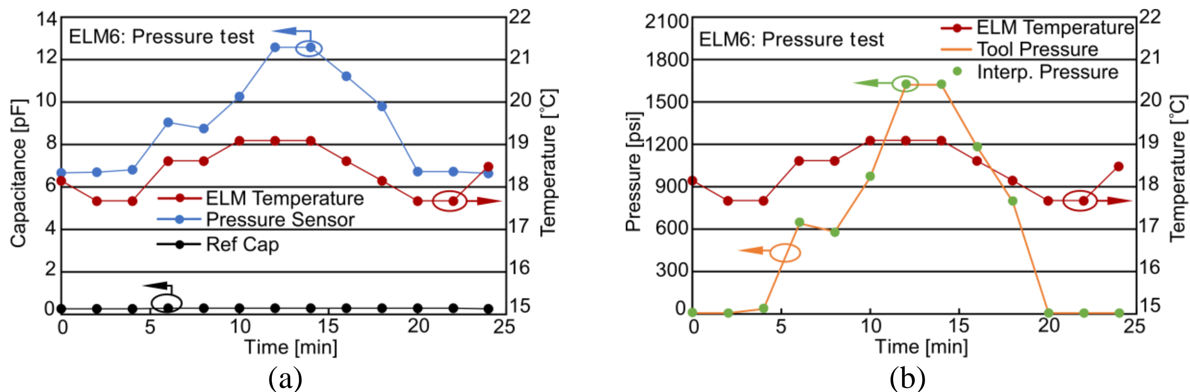

Figure 2.20: (a) Temperature (ELM Temperature) and capacitance (Pressure Sensor and Ref Cap) data recorded by ELM6 during pressure test; (b) temperature data and interpreted pressure data recorded by ELM6, and the tool pressure data during pressure test.

2.4.4 Temperature Test of ELM6

The temperature test was performed to ensure the integrity and functionality of the system electronics at high temperature. The system was successfully tested up to 65°C for >1 hour. The temperature data recorded by the system is plotted in Figure 2.21. For the test, the system was placed inside a high temperature oven and the temperature was ramped up to 65°C; the data was recorded with a time interval of 2 minutes.

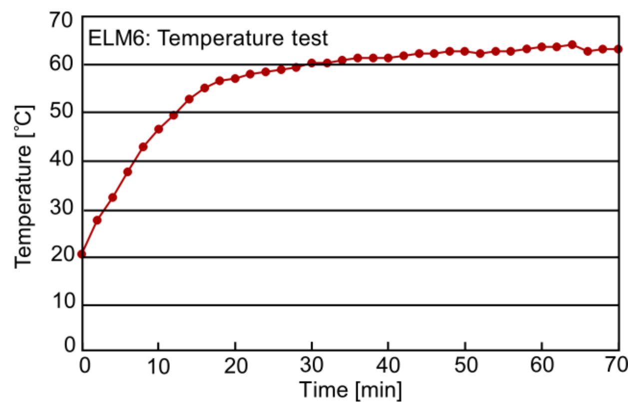

Figure 2.21: Temperature data recorded by ELM6 during HT test.

2.4.5 Combined Pressure and Temperature Test of ELM6

The ELM6 system was subjected to a combined pressure and temperature test in laboratory conditions that mimicked the pipeline environment. The system was successfully tested up to 12 MPa (1740 psi) and 62°C for >1 hour. The temperature and capacitance data recorded by the system are plotted in Figure 2.22(a). The temperature data recorded by ELM, interpreted pressure data recorded by ELM, and the tool pressure data are plotted in Figure 2.22(b). The calibration curve from the pressure test was used to interpret pressure and it matched the tool pressure (seen in Figure 2.22(b)). For the test, the system was placed inside a nylon bag filled with mineral oil and the bag was placed in HPHT equipment from Applitech Consulting Corp. (Lancaster, PA, USA). The test was performed at pressure up to 12 MPa (1740 psi) and temperature up to 62°C with data recorded every 2 minutes.

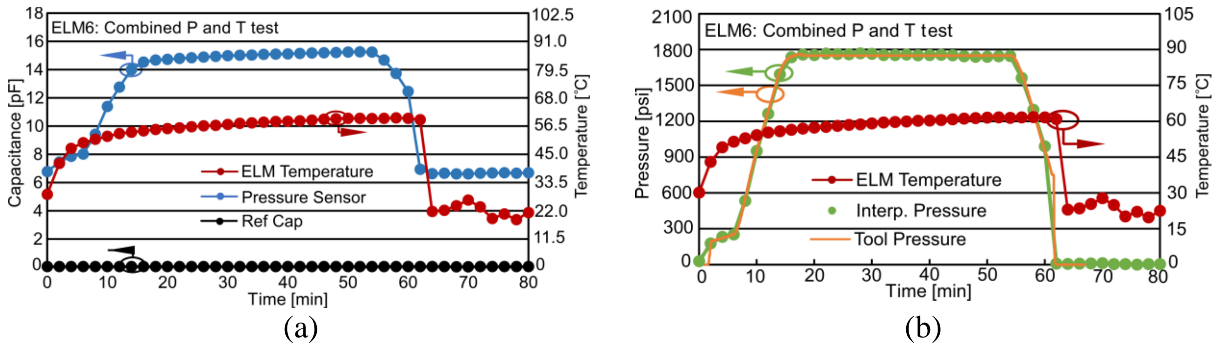

Figure 2.22: (a) Temperature (ELM Temperature) and capacitance (Pressure Sensor and Ref Cap) data recorded by ELM6; (b) temperature data recorded by ELM, interpreted pressure data recorded by ELM, and the tool pressure data.

2.5 Discussion and Summary

The ELM6 was developed for pipeline temperature, pressure, and inertial data logging at temperature up to 60°C and pressure up to 10 MPa, using commercial off-the-shelf electronics, MEMS pressure sensors and lithium-based batteries. The system used resonant inductive charging and RF based BLE protocol for communication. Capacitive MEMS pressure sensor with output capacitance change on the order of pF were integrated into the ELM6 system. The electronics of the system were integrated on a substrate and the designed folded stack size was $15.4 \times 14.2 \times 11.2$ mm^3. The system was successfully tested at up to 65°C and 12 MPa for more than 1 hour. It had a standby current of 8 µA at room temperature and the system lifetime was >10 days when operated at room temperature with detection time interval of 12 hours.

The microsystem can be hermetically encapsulated to survive the HPHT environment. The folded system can be encapsulated in a polymer such as silicone caulk and packaged in a shell made up of a material compatible with RF communication such as ceramic, similar to the method described in [Ma16]. The system can also be unfolded and then encapsulated in a polymer mold for protection as described in [Sui17]. The polymer material helps transfer the external pressure to the pressure sensors with low attenuation.

Power source is the main constraint factor for system lifetime at elevated temperature, particularly with the very limited system size. The MS920SE battery used in this work has a good battery capacity but will not be suitable for higher target temperatures. When a typical lithium battery is used at temperatures beyond specifications, the electrolyte inside the battery will degrade, adversely affecting the battery performance, reducing battery lifetime and causing chemical hazards such as leakage or explosion [Hen98, Dou12, Rob97]. Batteries based on alternative electrochemistry, such as lithium thionylchloride ($LiSOCl_2$) become appealing in applications demanding high temperatures for their outstanding performance at high temperature [Hen98]. Harvesting of mechanical, thermal or chemical energy may be used in systems with a rechargeable battery to supplement the limited battery capacity [She14].

The system size can be further decreased by using bare dies of the commercial components rather than using the packaged electronic chips. The individual electronic chips in the system currently are encapsulated in plastic packages with surface mount pads. The bare dies inside these packages have much smaller size. By estimation, replacing all packaged components with their bare die version would reduce the system size by at least 20% [Sui17].

Additional sensing capabilities such as chemical sensing can be integrated with the ELM to monitor different chemicals present in the pipeline. A chemical sensor could be added to the ELM in the form of a capacitive fringing field sensor patterned on the PCB. The capacitance of the sensor could be directly read by the C8051F990 MCU. The internal capacitance sensing module of this MCU has a minimal resolution of 1 fF and a maximum capacitance load of 500 pF [Sil11], which is adequate for incorporating most available capacitive sensors.

CHAPTER 3: Environmental Logging Microsystem for Downhole Monitoring

As noted in Chapter 1, the first goal is to investigate the system level design compromises, relationships between the building blocks, and overall performance limits under deployment conditions for autonomous microsystems. While Chapter 2 described an environmental logging microsystem (ELM6) developed for pipeline monitoring application, this chapter further describes a wireless autonomous environmental logging microsystem (ELM7) developed for downhole monitoring application.

In hydrofracturing processes used during oil and gas exploration, acquisition of well monitoring data such as temperature and pressure are necessary for increasing well efficiency, extending well life, increasing safety, and lowering the cost of operation [Cha12, Fin10, Wod11, Yu12]. Traditional means of wireline monitoring can only collect data near the wireline in the vertical segment of the wellbore [Ell07]. This leaves a need for data collection in horizontal wellbores and fractures, as well as deep into the reservoir.

Autonomous microsystems have a distinct advantage in being able to collect data throughout the entire wellbore by flowing a large number of systems into the wellbore using a fluid medium. The University of Tulsa and Saudi Aramco have developed a Φ7.5 mm system to monitor temperature and pressure in downhole environments [Yu12, Shi15]. The system was successfully operated in a wellbore for 1 hour at temperature up to 88°C and pressure up to 50 MPa. OpenField™ Technology have developed a pressure and temperature monitoring microsystem encased in a Φ50.8 mm spherical titanium shell that can flow in well pipes for downhole monitoring [Ope13].

For oil reservoirs that are typically 0.6-6 kilometers deep underground, the typical downhole environment can have an upper limit of ≥75ºC for temperature and ≥15 MPa for pressure [Cha12]. Therefore, the sensing targets for ELM7 include an upper limit for operating temperature of ≥75ºC and a preferred resolution of 0.1°C and an upper limit for operating pressure of ≥15 MPa and a preferred resolution of 0.5 kPa. This is in contrast with ELM6 described in Chapter 2, for monitoring oil and gas pipelines, in which the upper limit for operating temperature was 60°C and a preferred resolution of 0.5°C and the upper limit for operating pressure was 10 MPa and a preferred resolution of 2 kPa. Between deployments, the ELM7 should be able to accommodate wireless recharging of the battery as well as wireless communication with the external user. It should record inertial sensor data, limit memory usage, operate at low power, and accommodate re-usability of the PCB should the battery become non-functional. The system package should protect the system electronics from harsh environmental factors such as corrosive chemicals and abrasion and impact events while permitting the transfer of external pressure onto the ELM7 sensors and allowing wireless charging and wireless communication. An appropriate package integration method to address these challenges is described in Chapter 4.

The ELM7 uses resonant inductive charging and BLE communication for wireless charging and wireless communication, respectively. It uses the smallest suitable off-the-shelf electronic components that are assembled on a printed circuit board with a footprint of 5.6 cm^2. The ELM7 was successfully tested up to 85°C and up to 160°C for all elements excluding the battery. The limitation in this system is the incompatibility of the rechargeable battery at elevated temperature (>85°C). An environmental logging microsystem (ELM8) that uses large capacity primary battery rated for high temperature (125°C) has been proposed in Chapter 6. This system also utilizes improved power management circuit resulting in increased system lifetime.

3.1 System Hardware

The block diagram of ELM7 is shown in Figure 3.1. The microsystem consists of a BLE-MCU (B-MCU), a capacitance-to-digital converter (CDC), a wireless power receiver kit, an external wireless power transmitter kit, a charging circuit, a battery and a mechanical switch, MEMS pressure sensor, an inertial measurement unit (IMU), and an external Bluetooth module. Sensor data is collected and stored in B-MCU during deployment and wirelessly sent from the B-MCU to the external readout unit using the BLE protocol during data readout.

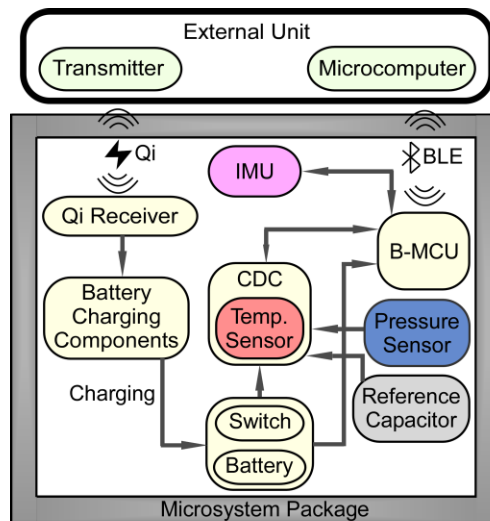

Figure 3.1: ELM7 block diagram.

The schematic of the system circuit for ELM7 is shown in Figure 3.2. A receiver chip and an external transmitter kit, along with charging components are used for wireless charging of the battery. The mechanical switch is used to conserve the battery power prior to packaging and deployment. The CDC is used to interface with the MEMS pressure sensor and the IMU using I^2C bus; it also provides temperature sensing using an internal circuit. The IMU consists of an accelerometer and a magnetometer and can be used for geolocation monitoring of the system. A reference capacitor is included to compensate for the temperature dependency of the CDC module. The B-MCU is used for wireless communication with the Bluetooth external unit using the BLE

protocol. During deployment, the sensor data is stored in the B-MCU. During data readout, this data is wirelessly sent from the B-MCU to the external readout unit using the BLE protocol.

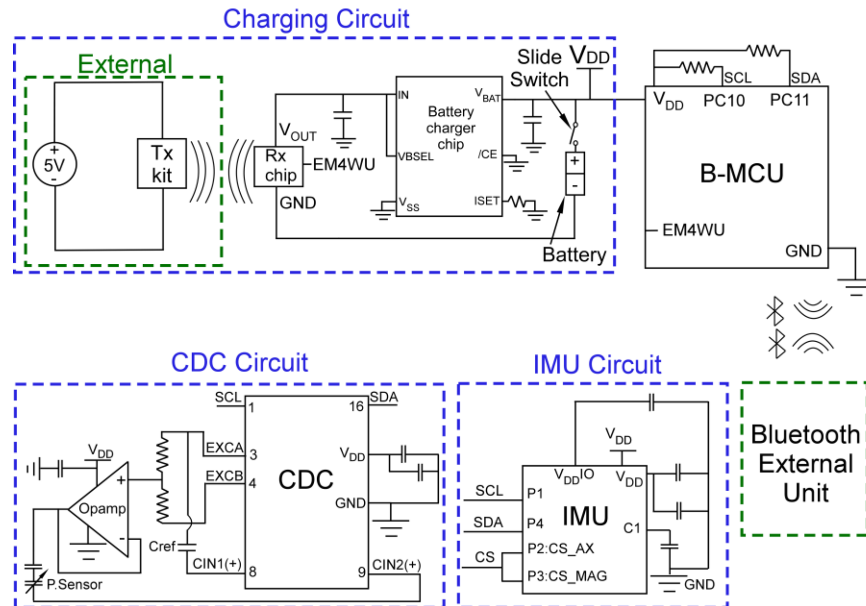

Figure 3.2: The circuit schematic of ELM7.

3.1.1 Component Selection

The general rules for selecting the components, listed in the sequence of preference, include small footprint, low power consumption, and integrated functionality. Table 3.1 summarizes the major components of the system circuit and their relevant features for the target application.

Table 3.1: Major system components

Component	Part No.	Footprint	Device Feature
Wireless charging transmitter kit	TYLT Vu-SOLO	85.0 mm × 85.0 mm	Follows Qi protocol
Wireless charging receiver chip	TI BQ51003	1.9 mm × 3.0 mm	Follows Qi protocol
Wireless charging receiver coil	TDK Corp. WR222230-26M8-G	Φ22.0 mm	2 layer, 27 μH
Battery	Tadiran TLI-1020A	Φ10.0 mm × 21.0 mm	4 V, 25 mAh capacity
Mechanical slide switch	C&K PCM12SM	8.3 mm × 5.0 mm	Single pole double throw switch
CDC	Analog Devices AD7746	5.1 mm × 6.4 mm	2 capacitive input channels, integrated temperature sensor
B-MCU	Silicon Labs BGM121	6.5 mm × 6.5 mm	2.5 μA deep sleep mode current, integrated antenna
IMU	STMicro LSM303C	2.0 mm × 2.0 mm	3-axis accelerometer, 3-axis magnetometer
Bluetooth external unit	RASPBERRY PI 3 STARTER KIT	167.6 mm × 124.5 mm	Raspberry Pi with integrated Bluetooth module

3.1.2 Charging Circuit Block

The charging circuit block includes an external transmitter kit (Tx kit) and a receiver chip (Rx chip) and coil for wireless power transfer, Tadiran TLI-1020A rechargeable lithium battery for energy storage, a decoupling capacitor, a battery charger chip to regulate the battery voltage and current, and a slide switch to avoid draining the battery during storage. A voltage value of 5 V is generated at the output of the Rx chip during wireless power transfer. This voltage is stepped down to 4.1 V by the voltage regulator. This results in a current flowing from the Rx chip, through the battery charger chip, into the battery for charging.

The wireless power transfer is achieved by using a transmitter kit (Figure 3.3(a)) and a receiver coil and chip (Figure 3.3(b)) as detailed in Table 3.1. Wireless power transfer of up to 2.5 W is achieved through a Φ22 mm coil on the receiver side and a Φ44 mm coil on the transmitter side. The receiver chip delivers the output power as a power supply with an output voltage of 5 V.

(a) (b)

Figure 3.3: (a) Transmitter kit and (b) receiver coil and chip for wireless charging of ELM7.

The TLI-1020A battery uses metallic lithium as its anode and thionyl chloride as its cathode. This battery has a capacity of 25 mAh and a volume of 2.0 cm^3. The specified operating temperature for the battery is -40°C to +85°C [Tad18]. A buffer capacitor of 4.7 μF is connected in parallel to the battery to accommodate any transient current need when the system operates in the active mode. A mechanical slide switch is added in series with the battery, which can break the power during storage and eliminate the standby current consumption. The system lifetime is

thus greatly extended during storage. The battery is charged using current/constant voltage (CCCV) charging method with a battery charging controller chip (BQ24083 from Texas Instruments). The output voltage and current of this chip can be configured to meet the battery charging conditions.

The battery is packaged with a quick connect connector (Figure 3.4). The ELM7 PCBs feature a battery connector port which is used for attaching the battery to the PCB through the quick connect connector. By attaching the battery to the PCB through a connector, the battery can be disposed when it cannot power the system and replaced with a fresh battery.

Figure 3.4: Tadiran Model TLI-1020A packaged with quick connect connector.

3.1.3 CDC Circuit Block

The pressure sensor integrated into the ELM7 is a custom microfabricated capacitive pressure sensor developed at the University of Michigan (as described in Section 2.1.6). The CDC chip integrated in to the ELM7 has a measurement range of ±4 pF around an adjustable offset of 0-17 pF; however, the sensor has a full-scale capacitance change up to 45 pF and offset capacitance up to 10 pF. Therefore, a range extension circuit is used between the capacitive pressure sensor and the CDC chip to increase its capacitance measurement range at the cost of reducing the capacitance resolution from 0.04 fF/code to 0.25 fF/code. When the sensor pressure response of

0.5 fF/kPa (3.3fF/psi) is combined with the CDC capacitance resolution of 0.25 fF/code, the average pressure resolution of the ELM7 becomes approximately 0.5 kPa (0.07 psi, 17 bit).

3.2 System Software

The software for the system has been developed to permit low power operation and limit memory usage. The typical operation flowchart for the system is shown in Figure 3.5. This provides the basis for the development of the system software. The B-MCU is initialized after power on. When the system is ready for deployment, it is placed in the detection state. In the detection state, B-MCU enters low power state to conserve power when no measurement is to be taken. At the end of the deployment, once the system is retrieved, it is charged and triggered out of the detection state by the user. When the data transfer is requested by the user, B-MCU reports the data to the user through the BLE link.

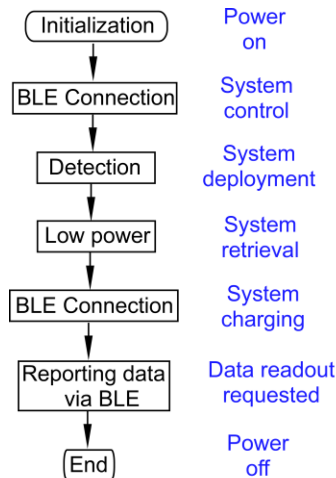

Figure 3.5: Typical operational flowchart for ELM7.

3.2.1 B-MCU Software State Diagram

The software state diagram for the B-MCU[3] is shown in Figure 3.6. The B-MCU is powered on, initialized, and moved into the Bluetooth connection state after initialization. In this

[3] B-MCU software was developed by Mr. Partha Dutta.

state, it is ready to connect to the user via BLE and can perform functions determined and sent as commands by the user via BLE. It transitions to the state corresponding to the function to be performed. The B-MCU is placed in the low power state (state B4) when the system is not in use. The functions of the individual states of B-MCU are explained below.

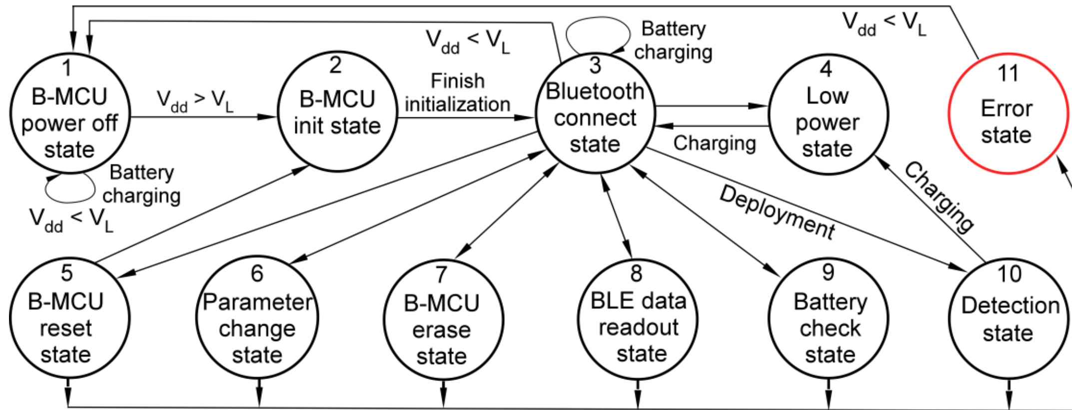

Figure 3.6: ELM7 state machine diagram.

State 1, B-MCU power off state:

This is the default state when a sensing program is not running and the battery is not being charged, and its voltage (V_{dd}) is below a certain threshold voltage, typically <2.4 V (V_L). The system typically enters this state after data collection when the battery is depleted. The B-MCU remains off in this state. Data is retained in the B-MCU flash memory without loss.

State 2, B-MCU init state:

This is a transient state during which the B-MCU turns on and all global constants and variables are initialized or restored from the flash memory. Registers of pertinent B-MCU peripherals (*e.g.* I^2C, digital I/O, etc.) are initialized for use in later operations. The radio is turned on briefly and the Bluetooth stack is initialized.

State 3, Bluetooth connect state:

This is a transitional state when the B-MCU advertises and waits for Bluetooth connection request from the client (external unit). Once connected to the client, the user can place the B-MCU in a new state such as the low power state (state 4), B-MCU reset state (state 5), parameter change

state (state 6), B-MCU erase state (state 7), BLE data readout state (state 8), battery check state (state 9), or detection state (state 10). These states are described below.

State 4, Low power state:

This is the state when the B-MCU is on but in shutoff mode to minimize power consumption. The B-MCU is placed in this state when the system is not in use. This is also the state the B-MCU goes into when transitioning from the detection state to the Bluetooth connect state. A reset signal is needed to wake up the B-MCU from this state. There is no status information retained from the previous operation and the Bluetooth stack is reinitialized.

State 5, B-MCU reset state:

This state allows the user to manually reset the system should any unexpected behavior occur, such as a clock source oscillating at an unexpected frequency.

State 6, Parameter change state:

The Bluetooth external interface can be used to set the testing parameters of ELM7. These parameters include detection time interval and sensor selection.

State 7, B-MCU erase state:

This state allows the user to erase the temperature, pressure, and inertial measurement data stored in the flash memory of B-MCU to permit collection and storage of new measurements.

State 8, BLE data readout state:

This is the state when the B-MCU transmits sensor data to the external unit. The B-MCU reads stored data from its flash memory and sends them as data packets to the external unit through the BLE link. BLE uses CRC and automatically corrects erroneous data packets by resending.

State 9, Battery check state:

This state reports the current battery level to the user over BLE.

State 10, Detection state:

This is the state that is triggered before deploying the ELM7 system in the environment of interest for data collection. In detection state, the system remains in low power state, only waking up at the prescribed detection interval (as set in state 6) to measure data and store it in flash, then re-entering the low power state (Figure 3.7). The system will repeat this process until either the battery dies, or flash memory is filled. If flash memory is filled, the system will exit detection state and enter a permanent low power state. Collected data will be conserved in this case.

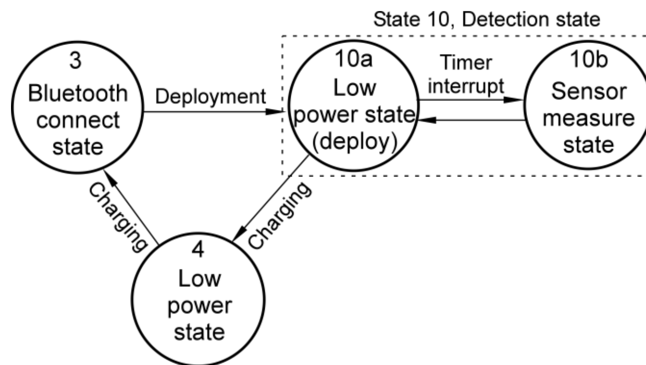

Figure 3.7: Diagram of sub-states for state 10, detection state.

State 11, Error state:

This is the "catch-all" state which the system enters if the program should fail unexpectedly and stop execution. Once the system enters this state, it needs to wait for the battery voltage to drop below V_L so that the system power is turned off. At that point, the system goes to State 1 and the battery can be recharged and the system re-initialized.

3.2.2 Bluetooth External Unit Software

The software for the Bluetooth external unit consists of graphical user interface (GUI) software and backend software for the Bluetooth module of RPi, both built using Python programming language.

The GUI is shown in Figure 3.8. The GUI software is built using Tkinter package of Python language. The main window of the interface consists of five sections: 1) BLE connection

control and status, 2) system information and status, 3) B-MCU commands, 4) battery status, and 5) sensor data plots. The functions of each section are described in Table 3.2.

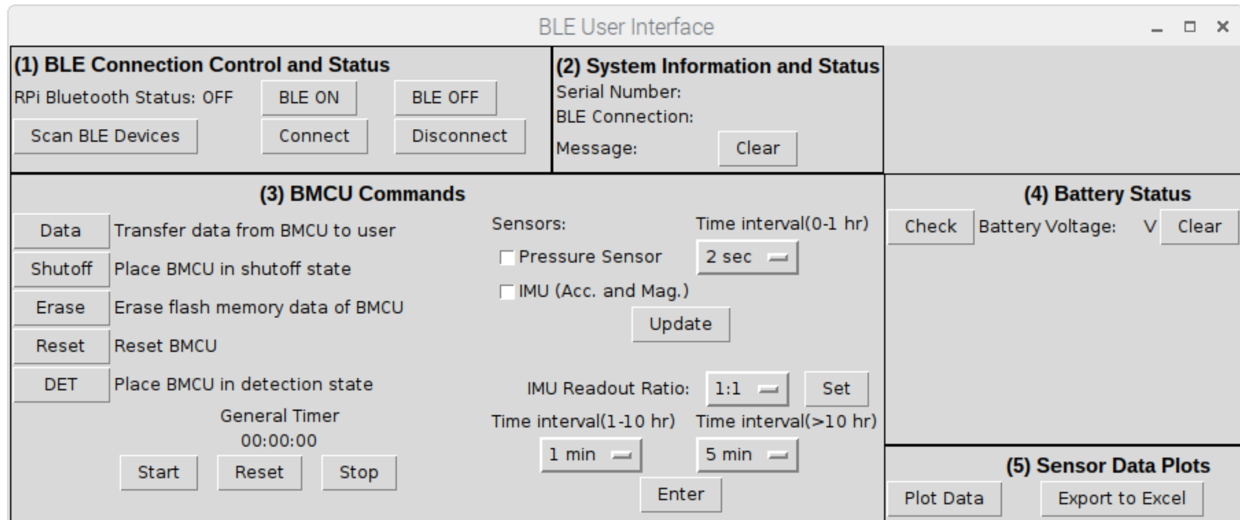

Figure 3.8: Graphical user interface of Bluetooth external unit.

Table 3.2: List of sections with their functions on the GUI

No.	Section	Functions
1.	BLE Connection Control and Status	• Allows the user to turn on/off Bluetooth on RPi • Allows the user to scan available BLE devices nearby • Allows the user to select the device for BLE connection and establish/terminate connection
2.	System Information and Status	• Displays the serial number of the connected ELM7 system • Displays the status of BLE connection • Displays the status of the system as a result of any command sent by the user. It contains a "Clear" button to clear the message
3.	B-MCU Commands	• Allows the user to send commands to the B-MCU • Allows the user to select the sensors, to choose the detection time interval, and to set the IMU readout ratio. The IMU readout is relative to the chosen detection interval for temperature and pressure • Contains a general timer to record the total time in which the system has been in detection state
4.	Battery Status	• Displays the battery voltage of the device
5.	Sensor Data Plots	• Provides user the graphical plot of sensor data • Allows the user to export data into an excel sheet

The backend software for the Bluetooth module of RPi is built using the *pygatt* module of Python. A screenshot of the interface during communication with ELM7 is shown in Figure 3.9(a). The serial number of the system along with BLE connection status and system message are

displayed in Section (2). The list of available BLE devices nearby is displayed after scanning (Figure 3.9(b)). All unrecognized devices are displayed as “None”.

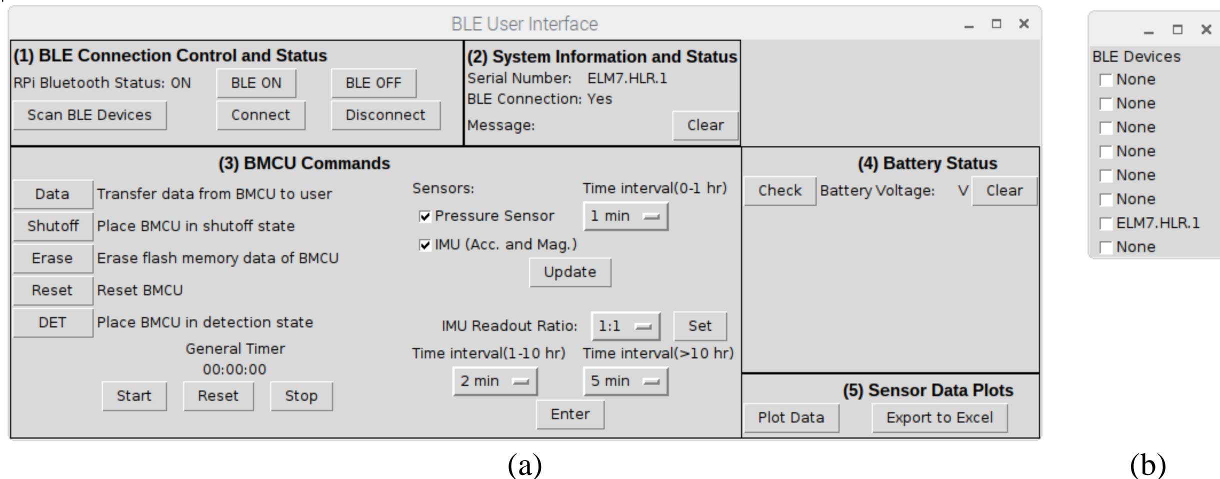

Figure 3.9: Screenshot of interface during communication with ELM7. (a) The serial number of the system along with BLE connection status and system message are displayed in Section (2). (b) The list of available BLE devices nearby is displayed after scanning; unrecognized devices are displayed as “None”.

3.3 System Integration and Fabrication

The system components are integrated on a PCB within the needed form factor to meet the density requirements of the packaged microsystem. The PCB is fabricated and assembled by a commercial PCB manufacturer. All components (excluding the pressure sensor) are assembled on the PCB using a commercial assembly service from the PCB manufacturer. The pressure sensor is assembled in-house using conductive Duralco 120 silver epoxy. Figure 3.10 shows the layout of the PCB. The PCB is circular in shape with a diameter of 26.7 mm to fit within the package. The Bluetooth module (B-MCU) is placed near the top edge and the top edge of the PCB is made flat to prevent shielding of the Bluetooth antenna.

The photos of the manufactured ELM7 PCB are shown in Figure 3.11. All components are integrated on top of the PCB (Figure 3.11(a)) and wireless receiver coil is integrated on the bottom side (Figure 3.11(b)). The receiver coil is placed on the bottom side to minimize the separation distance with the transmitter coil and thereby provide wireless charging of the packaged

ELM7 system. An opening is cut on the PCB beneath the custom pressure sensor so that the diaphragm is exposed to the exterior pressure, which would be transferred through the packaging elements. The CDC module is placed closed to the pressure sensor to reduce parasitic elements. The battery connector port is placed at a top corner of the PCB to minimize the overall cable length after connecting the battery and folding the cable. Major components labelled in the figure are detailed in Table 3.3.

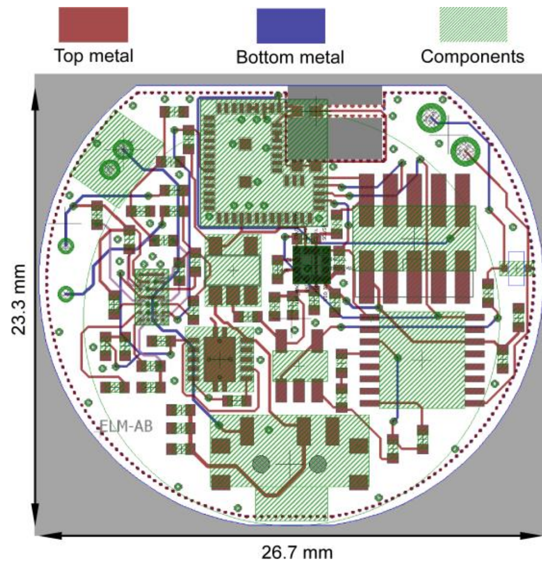

Figure 3.10: Layout of the ELM7 PCB (diameter: 26.7 mm).

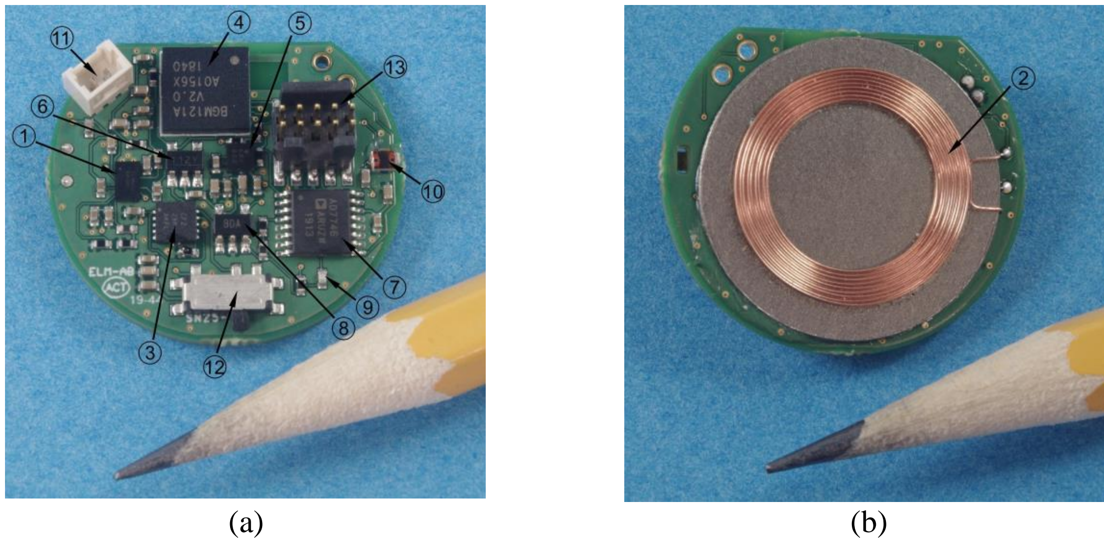

(a) (b)

Figure 3.11: Photos of the manufactured ELM7 PCB: (a) top and (b) bottom view.

Table 3.3: Major components of ELM7 PCB

No.	Component	Function
1.	Wireless receiver chip	Receives power wirelessly using Qi protocol
2.	Wireless receiver coil	Used for Qi charging
3.	Battery charging chip	Used to regulate charging of battery
4.	Bluetooth-microcontroller unit (B-MCU)	Stores sensor data and communicates with the Bluetooth external unit using the BLE protocol
5.	Inertial measurement unit (IMU)	Consists of an accelerometer and a magnetometer; can be used for geolocation monitoring of the system
6.	Voltage regulator	Used to regulate battery voltage
7.	Capacitance to Digital Converter (CDC)	Used to interface with MEMS pressure sensor; provides temperature sensing using an internal circuit.
8.	Operational Amplifier	Used for selecting the capacitive range
9.	Reference capacitor	Capacitor with no pressure response and negligible temperature coefficients. The measured value is used for calibration purposes
10.	Micromachined pressure sensor[4]	Custom fabricated sensor (HLR) for use up to 70 MPa (10.0 kpsi) static pressure
11.	Battery connector port	Used for connecting the battery to the PCB
12.	Mechanical switch	Completely detaches the battery from the ELM7 circuit for increased shelf life. Switch is pictured in OFF position
13.	Debug connector	Used for programming the B-MCU

Figure 3.12 shows the photo of battery connected to the PCB through battery connector port. The battery is detachable from the system PCB. Table 3.4 summarizes the overall design parameters of the ELM7 system after integration. The electrical parameters were measured in the system characterization tests, which are explained in detail in Section 3.4.

[4] Pressure sensor was assembled by Dr. Alexander Benken.

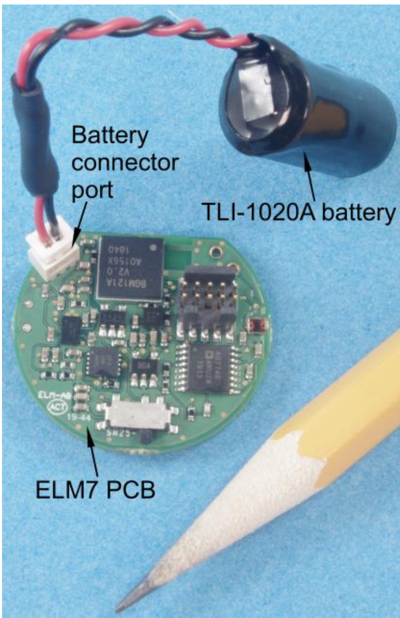

Figure 3.12: Photo of TLI-1020A battery connected to ELM7 PCB.

Table 3.4: Overall design parameters of ELM7

Physical Parameters	
PCB diameter	26.7 mm
Electrical Parameters	
Upper limit of operating temperature (with battery)	≥75ºC
Upper limit of operating temperature (without battery)	≤160ºC
Temperature resolution	0.1ºC
Upper limit of operating pressure	≥15 MPa (2175 psi)
Pressure resolution	0.5 kPa (0.07 psi)
Acceleration range	±8 g
Acceleration resolution	0.244 mg/LSB
Magnetic field range	±16 gauss
Magnetic field resolution	0.58 mgauss/LSB
Battery max. voltage	4.1 V
Battery capacity & size	25 mAh Φ10 mm x 21 mm
BLE current peak (Data transfer, RT)	Rx: ≈13 mA; Tx: ≈11 mA
Peak system current (Detection, RT)	4.2 mA
Peak system current (Detection, 100°C)	5.0 mA
Peak system current (Detection, 160°C)	6.7 mA
Operating frequency	32.768 kHz (core) 38 MHz (Bluetooth)
Total/data flash memory size	256 kB/ 84 kB

3.4 Experimental Results

Tests of the ELM7 system were carried out in two stages: (a) Characterization of the system components and circuits and (b) temperature tests. Test results from (a) suggest that the system achieved all the intended functionalities for temperature, pressure, and inertial sensor measurement, wireless battery charging, low power operation, and wireless communication. In temperature tests in step (b), the system was successfully tested at temperature up to 85°C and up to 160°C for all elements excluding the battery.

3.4.1 Characterization of ELM7 Components and Circuits

The ELM7 system was characterized for full system functionality. The wireless charging of the system was characterized in two parts: the wireless power transfer between the transmitter and the receiver kits, and the wireless charging of the battery.

A. Wireless power transfer between transmitter and receiver

The wireless power transfer was verified between the transmitter and the receiver kits by powering the transmitter kit using a 5 V USB supply and aligning the receiver coil to the transmitter coil. The wireless power transfer was successfully verified between the transmitter and the receiver for a maximum distance of 8 mm between the coils.

B. Wireless charging of battery

The circuit for the wireless charging of TLI-1020A battery used in ELM7 is shown in Figure 3.13(a). This circuit is a part of the overall circuit schematic (shown in Figure 3.2). A typical characteristic plot of the open circuit voltage (OCV) of a partially depleted TLI-1020A battery is shown in Figure 3.13(b). A stable OCV (>4.0 V) indicates that it is fully charged.

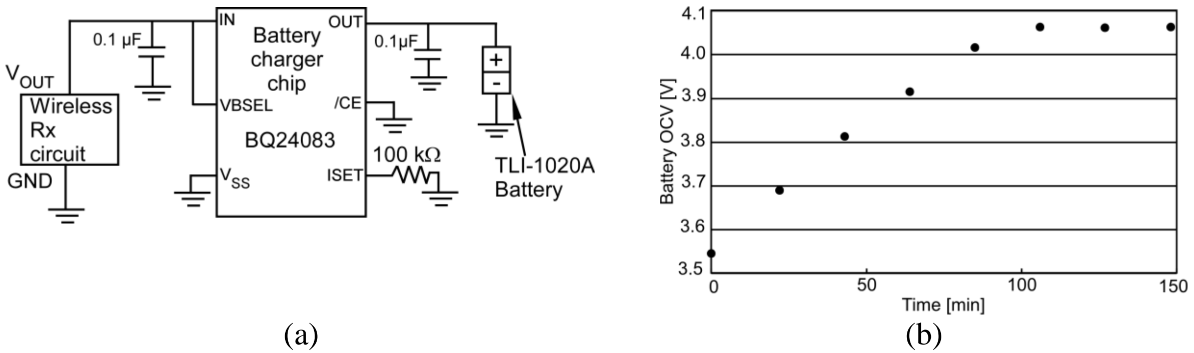

(a) (b)

Figure 3.13: ELM7 battery charging (a) circuit and (b) OCV plot.

C. Detection mode current characterization

The current consumption of the ELM7 system in detection mode at different temperatures is shown in Figure 3.14. The current increases from 25°C to 160°C by ≈60%.

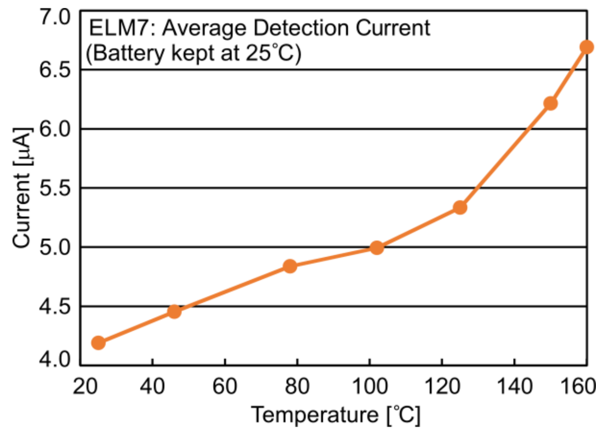

Figure 3.14: Detection mode current variation with temperature.

D. Functional Tests

Functional characterization of proto-board implementations of the ELM7 system was used to validate the state machine. The I^2C communication was successfully tested between B-MCU and IMU; and between B-MCU and CDC module. The Bluetooth functionality of the B-MCU was successfully verified; the battery voltage of ELM7 was accurately read out. The temperature, pressure, and inertial sensor data was successfully collected and readout using BLE.

The test results showed that the proto-board system achieved all its intended functionality for temperature, pressure, and inertial data measurements, battery voltage measurement, wireless data communication, and all other system functions.

3.4.2 *Temperature Tests of ELM7*

Temperature tests were performed to ensure the integrity and functionality of the system electronics at high temperature. The entire ELM7 system was successfully tested up to 85°C for >2 hours. The temperature data recorded by the system is plotted in Figure 3.16.

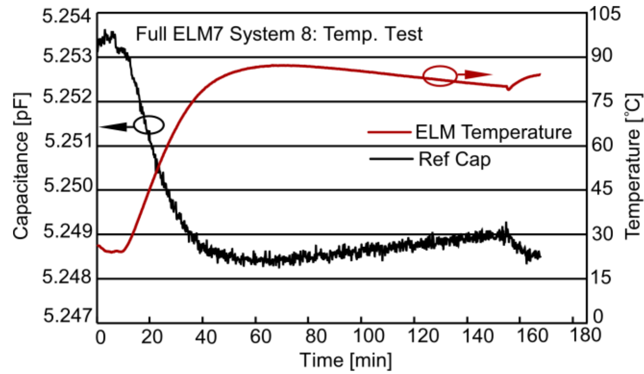

Figure 3.15: Temperature data recorded by the full ELM7 system.

The ELM7 PCB was successfully tested up to 160°C for >3 hours with battery placed at room temperature. The battery was placed at room temperature since the Tadiran TLI-1020A battery used in this system is only rated up to 85°C [Tad18]. The temperature data recorded by the system is shown in Figure 3.17.

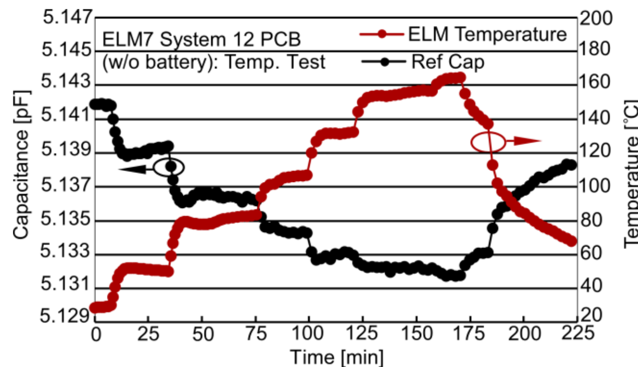

Figure 3.16: Temperature data recorded by ELM7 with battery at room temperature.

3.5 Discussion and Summary

The ELM7 was developed for downhole temperature, pressure, and inertial data logging at temperature ≥75ºC and pressure ≥15 MPa, using commercial off-the-shelf electronics, MEMS pressure sensors and lithium-based batteries. The system used resonant inductive charging and RF based BLE protocol for communication. Capacitive MEMS pressure sensor with output capacitance change on the order of pF were integrated into the ELM7 system. The electronics of the system were integrated on a PCB within the needed form factor to meet the density requirements of the packaged microsystem. An opening was cut on the PCB beneath the pressure sensor to expose the diaphragm to the exterior pressure, transferred through the packaging elements. The receiver coil was placed on the bottom side of the PCB to enable wireless charging of the packaged ELM7 system. The system was successfully tested at temperature up to 85°C and up to 160°C for all elements excluding the battery.

The ELM7 has several software features that provide high system versatility. It has the capability of variable sensor data acquisition rates because of the need to record more data points during and right after deployment and a smaller number of data points thereafter. Additional features such as variable bandwidth for the IMU can be implemented by turning the IMU off for some portion of the time, thus increasing the lifetime of the system by reducing the power consumption and data storage space. The IMU can also be programmed to operate in "burst" mode instead of "single reading" mode for recording accelerometer and magnetometer data. This causes the IMU to be active with high bandwidth for short periods of time and provides more usability for the IMU data. Additionally, battery monitoring of the deployed system can be implemented through B-MCU software to record the current battery level. This can be helpful as writing with depleted battery can sometimes corrupt the flash memory.

The high temperature of the downhole environment presents a major challenge to the electronics of the ELM. Silicon-based CMOS transistors, which are the building blocks of modern digital computing and control electronics, have leakage currents that increase exponentially with temperature [Sui17]. For a regular CMOS transistor, there are three main leakage paths: reverse biased PN junction leakage, subthreshold leakage, and gate leakage. Among these paths, the reverse biased PN junction leakage current has the highest dependence on temperature [Roy03]. The electronic chips fabricated using standard CMOS technology are not optimized for high temperature operation. Specialized electronics for temperatures well above 200°C use technologies such as trench isolation, silicon-on-insulator (SOI) substrates, and other variations of the standard CMOS process [Wat12]. Silicon carbide electronics also have excellent high temperature performance but can of use only after the scale of integration has been significantly advanced [Yan13].

Batteries at the millimeter-centimeter scale that provide enduring high temperature operation are required for long term downhole monitoring. The commercially available coin batteries used in previous ELMs use manganese silicon lithium chemistry [Sei14]. They have a rated temperature range only up to 60°C, and their performance is degraded significantly at higher temperatures. Batteries based on lithium thionylchloride ($LiSOCl_2$) become appealing for oil field applications due to outstanding performance at high temperature [Hen98]. Rechargeable batteries based on this chemistry that have been developed by Tadiran Batteries have been used for ELM7. However, they have a rated temperature range up to 85°C, and their performance is degraded significantly at higher temperatures. Non-rechargeable batteries based on $LiSOCl_2$ chemistry have also been developed by Tadiran Batteries with operating temperature range up to 125°C. These would suite for downhole monitoring with temperature up to 125°C.

CHAPTER 4: Flow-Compatible Package for ELM for Downhole Monitoring

As noted in Chapter 1, the second goal is to investigate a package integration approach to permit deployment, retrieval, and reusability of downhole sensing microsystems. Toward that end, this chapter describes an approach of encapsulating ELM7 in a flow-compatible package[5].

For oil reservoirs that are typically 0.6-6 kilometers deep underground, the typical downhole environment can have an upper limit of ≥75ºC for temperature, ≥15 MPa for pressure, and salinity range of 5-15% (50,000-150,000 ppm) [Cha12]. In some cases, hydrogen sulfide is also present in the downhole fluids. The density of downhole fluid is between 1.0 g/cc and 1.3 g/cc [Bab18, Lia18]. The exterior packaged system size is limited by the size of the well bore, typically no more than 40 mm diameter. The package integration approach must permit transfer of external pressure and temperature to the sensors while protecting the electronics from the harsh environment during deployments; between deployments it must allow wireless charging and wireless communication, and in certain situations it must also allow the removal of the package and reusability of the system hardware. These goals are achieved by designing the ELM7 electronics, power source, and sensors to fit within a flow-compatible package designed to operate within oil well bores. This requires proper positioning of the components on the PCB. The ELM7 electronics should be integrated within the needed form factor to meet the density requirements of the packaged microsystem. Based on the above considerations, the design targets for the system

[5] The packaging effort was led by Dr. Alex Benken.

package include an upper limit for operating temperature of ≥75ºC, an upper limit for operating pressure of ≥15 MPa, packaged system size ≤25 cm^3, and packaged system density ≤1.2 g/cc.

Previous generations of ELM (ELM1, ELM2, and ELM3) were packaged to protect the microsystem against the harsh downhole environment factors including high temperature, high pressure, various chemicals, abrasion, and impact. The packages also provided physical coupling to the environment and allowed optical charging and communication. The ELM1 PCB was folded into a stack and placed in a stainless-steel package with a sapphire lid [Ma15]. A parylene layer was coated on the outer surface of the package for anti-corrosive protection. The ELM2 PCB was folded into a stack and encapsulated in a stainless-steel tube, which provided impact and abrasion tolerance [Ma16]. The tube was filled with a transparent polymer to allow optical charging and communication of the system. The filler polymer material also helped to transfer the external pressure to the pressure sensors with low attenuation. The ELM3 PCB was encapsulated in a transparent polymer mold for anti-corrosion protection [Sui17]. Packaged ELM2 and ELM3 systems were tested in a brine well at a depth up to 1235 m with temperature up to 70°C and pressure up to 10 MPa. Researchers at the University of Tulsa and Saudi Aramco demonstrated a polymer packaging method by encapsulating a Φ7.5 mm system to monitor temperature and pressure in downhole environments [Yu12, Shi15]. The system was operated in a wellbore for 1 hour at temperature up to 88°C and pressure up to 50 MPa. However, its small size may limit battery lifetime and a high density may limit recovery rate. OpenField™ Technology have developed a pressure and temperature monitoring microsystem encased in a Φ50.8 mm spherical titanium shell that can flow in well pipes for downhole monitoring [Ope13]. However, its large size may prevent it from being used in smaller wellbores.

In this work, the package is a molded fluoroelastomer rubber with a low bulk density filler material. This rubber provides sufficient chemical and mechanical protection, is sufficiently pliable enough to permit pressure transmission, and is transparent to wireless RF signals for power and data transfer. Furthermore, the filler material allows pressure to be transmitted, maintain a low system density, and permit reusability of the system hardware. The packaged systems had a volume of ≈25 cm^3 and a density of 1.2 g/cc. Active microsystems with temperature, pressure, and inertial sensors were encapsulated in these packages, and successfully tested in laboratory conditions tested up to 85°C and 41.5 MPa for more than 4 days. The packaged systems were also successfully tested in field deployment conditions in an operational oil well to a depth of 1290 m.

4.1 Package Design and Fabrication

The package is custom injection molded using Viton™, a fluoroelastomer with a high temperature and chemical resistance [Dup19]. The package is designed to be density matched to the fluidic environment of the well bore, permitting a free-flow deployment method. The size of the package is determined by the size of the well bore in which these systems are to be inserted. The shape of the package is designed to permit it to more easily flow within the well bore and to prevent it from becoming lodged or stuck during deployment. It consists of two molded parts: domed cylindrical molded tube and molded tube cap, with diameter of 30 mm and height of 35 mm. The system electronics and battery are secured inside a high temperature thermoplastic (Wrightlon® 7400) bag filled with non-conductive oil and placed into the package, (Figure 4.1). The package is filled with low bulk density cenospheres to reduce effective density and permit pressure transfer to the system. Viton, cenospheres, and oil act as a cushion against damage to further protect the electronics during high impact events. The two Viton parts are sealed together

with Fluorodyn™ caulk (Thermodyn Corporation, Houston, TX, USA). The size and density of all the components are given in Table 4.1. The final system density is 1.2 g/cc.

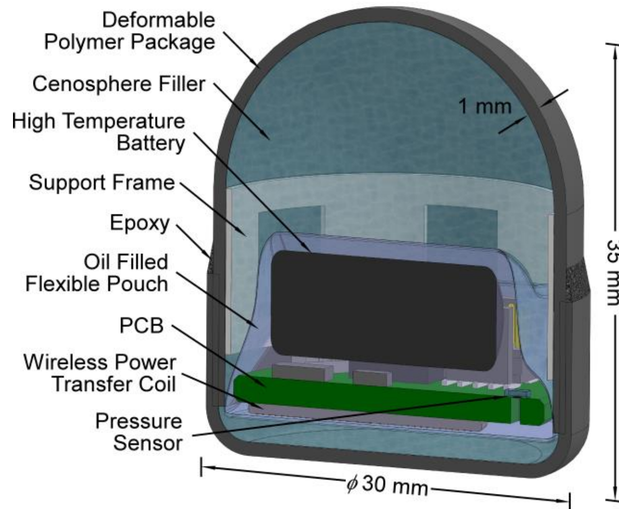

Figure 4.1: Design of ELM7 molded Viton package with system components.

Table 4.1: Size and density information of ELM7 packaged system components

Components	Density	Volume
Viton	2.00 g/cc	6.0 cm^3
ELM7 PCB	1.80 g/cc	1.5 cm^3
Battery, TLI-1020A	2.60 g/cc	2.0 cm^3
Cenospheres	0.35 g/cc	As Needed

Figure 4.2 shows the photos of fabricated components. Figure 4.2(a) shows photo of injection molded Viton domed cylindrical tube and tube cap. The photo of ELM7 PCB and battery secured inside a high temperature thermoplastic bag filled with non-conductive oil is shown in Figure 4.2(b). Figure 4.2(c) shows the photo of fully packaged ELM7 systems. The packaged systems have a volume of <25 cm^3, maximum package diagonal of 39.5 mm, and density of <1.2 kg/m^3.

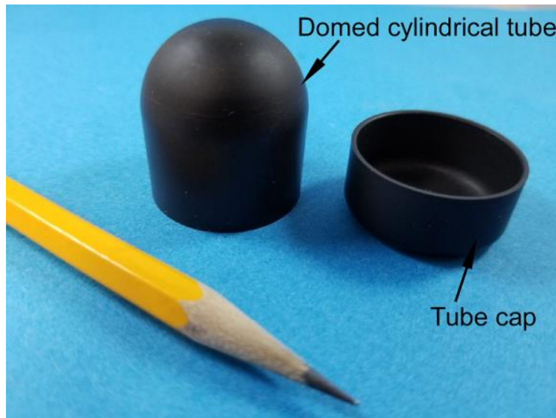

(a)

(b)

(c)

Figure 4.2: Photos of (a) injection molded Viton domed cylindrical tube and tube cap; (b) ELM7 PCB and battery secured inside a high temperature thermoplastic bag filled with non-conductive oil; (c) fully packaged ELM7 systems.

4.2 Packaged ELM Test Results

System testing was conducted in both laboratory and field settings. Laboratory testing validated system performance at temperatures and pressures of up to 85ºC and 41.5 MPa (6,000 psi). Field testing was completed to validate system performance in the target environment by deploying microsystems into an operation oil well to a depth of 1,290 m. The systems successfully measured and recorded temperature, pressure, and inertial data, matching expected conditions in the well during deployment.

4.2.1 Laboratory testing of ELM7 systems

The ELM7 systems were subjected to combined HPHT tests to ensure functionality under conditions which would meet or exceed expected environments in the oil well borehole. Packaged microsystems with a fully charged battery were triggered into the detection state and inserted into the chamber of an HPHT tool (Applitech Consulting Corp., Lancaster, PA, USA) filled with mineral oil. The tool was then activated to achieve the desired target values of temperature and pressure. At the conclusion of the test, the systems were retrieved from the tool and interrogated with the external microcomputer to transfer the collected data.

While many tests were performed on the microsystems, a test to a maximum temperature of 85°C and pressure of 41.5 MPa (6,000 psi) spanning >96 hours is shown in Figure 4.3(a). At the conclusion of the test, the system successfully transmitted its data to the external unit and no leakage or deformation in the package was observed. In Figure 4.3(a), the data retrieved from the system are plotted, showing the measured temperature (Temperature), pressure applied by the tool (Tool Pres.), capacitance measured from the pressure sensor (Pres. Sens.), and capacitance measured from the reference capacitor (Ref. Cap.). These same data are plotted in Figure 4.3(b), but only for hours 96.0 – 96.7 for enhanced clarity.

Using the temporally correlated tool and system data, coefficients were fit to a calibration polynomial, given in equation 4.1 (same as equation 2.1),

$$P_{sys} = b_1 + (b_2 \times T_{sys}) + (b_3 \times \Delta C) + (b_4 \times \Delta C^2) + (b_5 \times \Delta C^3) + (b_6 \times T_{sys} \times \Delta C) \quad (4.1)$$

where P_{sys} is the interpreted pressure, b_1 to b_6 are the calibration coefficients, T_{sys} is the temperature recorded by CDC, and ΔC is the difference in capacitance recorded by the pressure sensor and the reference capacitor. The calibration coefficients are found based on least squares regression method. This equation was used to transform the capacitance of the pressure sensor

and reference capacitor and recorded temperature to applied pressure. The calibration data was stored for each microsystem and used to interpret the recorded data during the field trails. The measured temperature, interpreted pressure data of the microsystem (Interp. Pres.), and the tool pressure (Tool Pres.) data are plotted in Figure 4.3(c) showing a good match between the tool and microsystem pressure values.

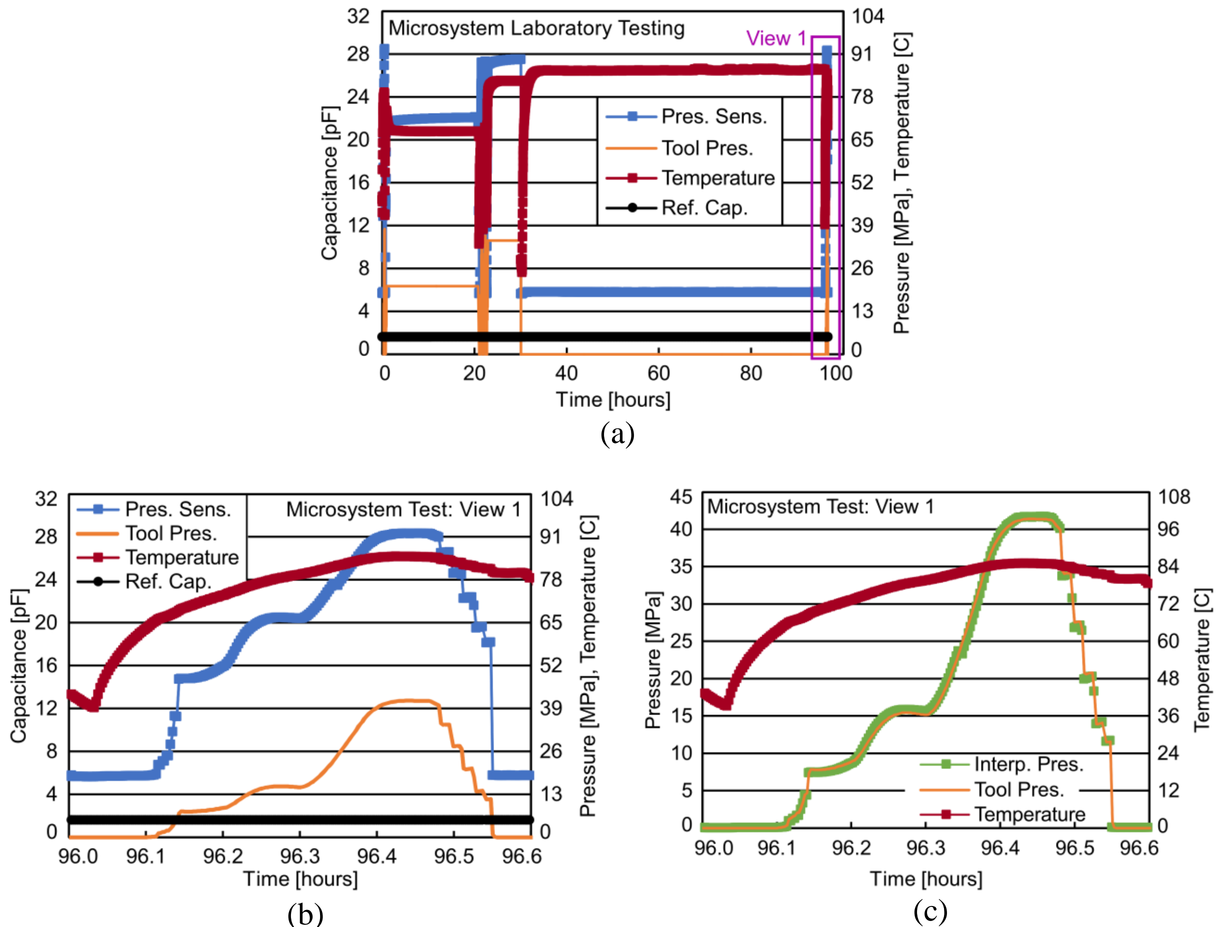

Figure 4.3: Laboratory testing of fully packaged ELM7 system at HPHT for (a) 96-hour duration, (b) enhanced view of full test at maximum pressure and temperature, and (c) enhanced view of test showing interpreted microsystem pressure using calibration equation as given in (4.1).

4.2.2 Downhole testing of ELM7 systems

Field tests were performed on encapsulated ELM7 systems by Total S.A. (Paris, France) in an operational oil well in the Democratic Republic of the Congo (Africa) to demonstrate the functionality of the systems in a wellbore environment. The systems were placed into a wireline

basket (Figure 4.4) and lowered into the wellbore. Free-flow deployment was not utilized for this initial field trial to ensure microsystem recovery. Reference readings were provided by a commercial instrument located at a depth of 1,290 m in the well. The systems were lowered into the well to a maximum depth of 1,290 m and then returned to the surface for interrogation.

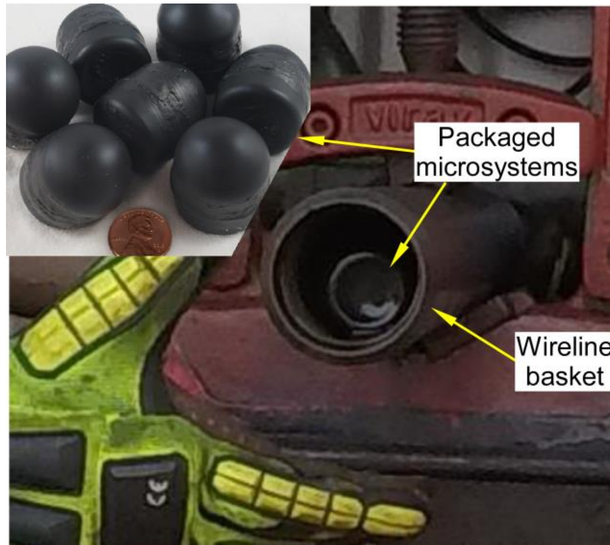

Figure 4.4: Photos of a packaged microsystem inside a wireline basket captured by Total S.A. during field tests in an operational oil well and fully packaged microsystems (inset).

Recorded data from a microsystem is shown in Figure 4.5(a). The pressure was interpreted using calibration data obtained from laboratory testing of the microsystem. The highest temperature and pressure recorded by the system was 65°C and 7 MPa (1,015 psi), Figure 4.5(b). The microsystem data matches well with the commercial instrument when collocated at the maximum depth of 1,290 m, indicating that the package permitted transfer of external pressure and temperature to the sensors. The system also recorded the acceleration and magnetic field data, shown in Figure 4.6(a) and Figure 4.6(b).

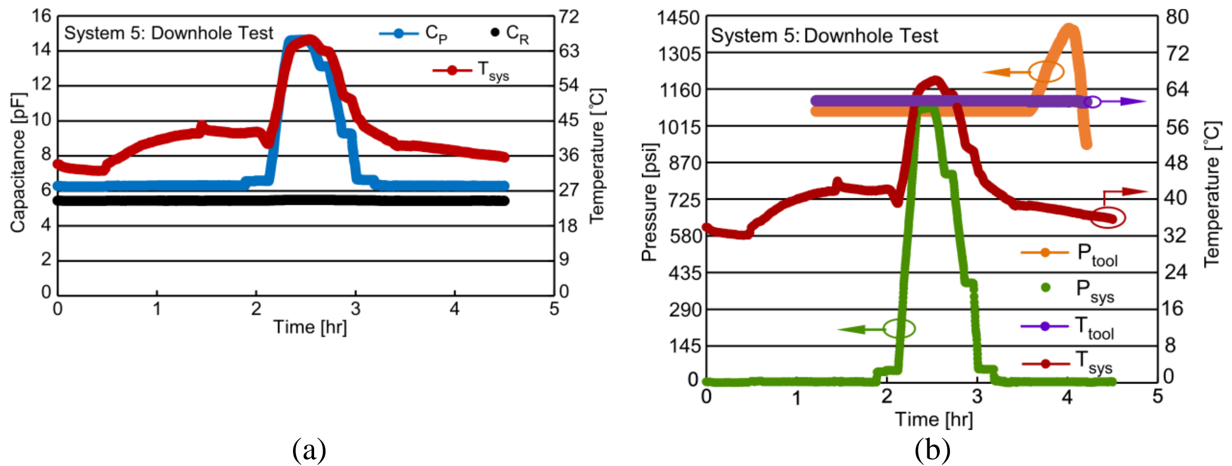

(a) (b)

Figure 4.5: Results from downhole functional oil well test. (a) Capacitance (C_P and C_R) and temperature (T_{sys}) recorded by the system. (b) Pressure (P_{tool}) and temperature (T_{tool}) reported by a commercial pressure and temperature gauge at a well depth of 1290 m, and the interpreted pressure (P_{sys}) and system temperature (T_{sys}) based on data recorded by the system.

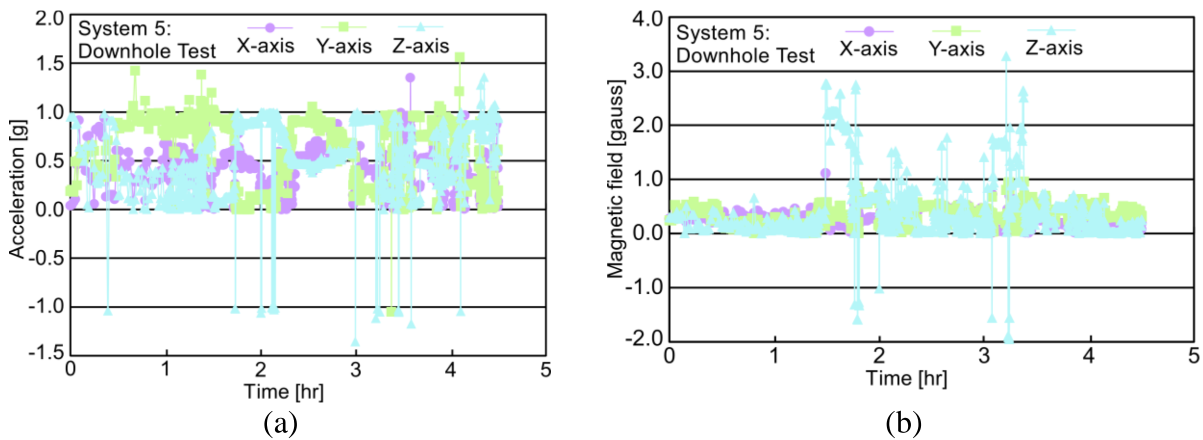

(a) (b)

Figure 4.6: Results from downhole functional oil well test. (a) Acceleration and (b) Magnetic field in X, Y, and Z axes data recorded by the system.

Table 4.2 summarizes the overall design and performance parameters of the system. The system was successfully tested and recorded temperatures up to 85°C with a resolution of 0.1°C, pressures up to 41.5 MPa (6,000 psi) with a resolution of 0.5 kPa (0.08 psi), demonstrating an operation lifetime of more than 4 days at these temperature and pressure values.

Table 4.2: Design and performance parameters of the ELM7 system

Parameter	Value
Packaged system volume	25 cm^3
Package dimensions	Φ30 x 35 mm^3 (Max. diagonal: 39.5 mm)
Packaged system density	≈1.2 kg/m^3
Exterior package material	Fluoroelastomer Viton™ rubber
Max. tested temperature	85°C
Temperature resolution	0.1°C
Range of custom pressure sensor	0 – 70 MPa (10,000 psi)
Avg. pressure sensor response	0.5 fF/kPa (3.3 fF/psi)
Max. tested pressure of microsystem	41.5 MPa (6,000 psi)
Pressure resolution of microsystem	0.5 kPa (0.08 psi)
Inertial sensing (LSM303C)	Accelerometer and magnetometer
Acceleration range	±8 g
Magnetic field range	±16 gauss
Operating lifetime @ 85°C	>4 days

4.3 Discussion and Summary

In this work, the package integration approach was developed for encapsulating ELM7 for downhole monitoring. The microsystem permitted free-flow operation due to a sufficiently small form factor (≈25 cm^3) and density matching (1.2 kg/m^3) to that of the fluid within a wellbore. The package integration approach accommodated wireless recharging of the battery with the Qi protocol and wireless Bluetooth communication with an external unit. It was able to provide chemical and mechanical protection of the electronics while also permitting sensor and RF communication and reusability and reclamation of the system hardware.

Pressures up to 41.5 MPa (6,000 psi), temperatures up to 85°C, and inertial (acceleration and magnetic field) data were successfully recorded in a laboratory setting, demonstrating an operation lifetime of more than 4 days. These combined HPHT tests ensured full functionality of the microsystems under conditions which exceeded expected environments in the oil well borehole.

The microsystems were successfully tested in the field, conducted by deployment of microsystems into an operational oil well to a depth of 1,290 m. Temperature, pressure, and inertial data were recorded, matching expected conditions in the downhole environment during deployment. To our knowledge, this was the first successful demonstration of autonomous microsystem deployment into an operational oil well in which data was successfully collected.

Additional sensing modalities can be integrated into the microsystem, including acoustic and chemical sensors. For increased operating temperature range, the microsystem could use a battery rated for higher temperatures to permit deployment into harsher environments.

CHAPTER 5: High Capacity Rechargeable Nickel-Zinc Microbatteries

As noted in Chapter 1, the third goal is to investigate a scalable fabrication method for incorporating microbatteries within autonomous microsystems. Toward that end, this chapter describes the design, fabrication, and characterization of Nickel-Zinc microbatteries.

Battery miniaturization is necessary to keep pace with the advances in microsystem technologies [Che11]. The size of the microsystem is often determined by the size of its power source, which is typically the largest component in the microsystem [Alb08]. For example, the system volume of a micro-air vehicle (cyborg beetle) without the battery was 3 mm^3, while the battery volume was 110 mm^3 [Sat08]. In another example, a swallowable microelectronic pill for remote biomedical measurements had a system volume of 0.5 mm^3 without the battery, while the battery volume was 1200 mm^3 [Joh04]. Integration of the power source within the microsystem package is usually a challenge, particularly for applications with a constraint on the size of the microsystem.

There is a demand for high performance miniature power sources which could enable new microsystems, particularly autonomous microsystems [Koe97]. Such microsystems typically need rechargeable batteries that have dimensions on the scale of 1–10 mm^3 [Bat00]. This size includes all the battery components and associated packaging. Although Li-ion batteries are appealing in terms of energy density, cyclability and high-temperature performance, Ni-Zn batteries have benefits like high power density and good cyclability. Additionally, Ni-Zn batteries utilize low-cost materials that are easy to handle and are more environmentally benign.

Batch mode fabrication of 3D Ni-Zn batteries was reported in [Cha07]. Deep reactive-ion-etching (DRIE) was used to create an array of deep holes in the silicon mold. Electroplating was used to fill the mold with Ni and Zn battery materials. The silicon mold was removed by etching to obtain arrays of interdigitated nickel and zinc post electrodes. Nickel hydroxide was electrochemically deposited on each Ni post of the array to obtain functional 3D Ni-Zn microbatteries. These batteries had a typical area of 0.25 cm^2, and a capacity density of 0.0025 mAh/cm^2. They could last only for six cycles due to the formation of Zn dendrites in KOH electrolyte.

Standard microfabrication procedures like electroplating and electron-beam (e-beam) evaporation were used to batch fabricate microscopic Ni-Zn batteries in [Hum01]. The batteries had a side-by-side cell design. A zinc seed layer was deposited using e-beam evaporation and the zinc anode was electroplated and patterned on top of this. The cathode consisted of nickel oxy-hydroxide (NiOOH) which was electrodeposited on a nickel current collector. The electrolyte used was 20 wt% KOH saturated with zinc oxide. The sidewalls of these batteries were made from a light-sensitive epoxy. These batteries had a typical footprint of 0.02 cm^2, and a capacity of approximately 0.389 mAh/cm^2.

The researchers in [Iwa05] built Ni-Zn battery using polymer hydrogel electrolyte. They used a commercially available nickel positive electrode, a polypropylene spacer, and electrodeposited zinc electrode on carbon paper. The electrolyte was prepared from cross-linked potassium poly(acrylate) and KOH solution. This hydrogel electrolyte was superior to aqueous KOH electrolyte by restraining the formation of zinc dendrites and thereby improve the battery performance. These batteries had a specific capacity of 100 mAh/g.

In this work, a facile approach for batch mode fabrication of rechargeable Ni-Zn microbatteries is presented. Micro electro discharge machining (μEDM) is used to define arrays of cavities in foils of Ni and Zn. The cathode and electrolyte materials are incorporated using a self-aligned damascene method. The fabricated batteries have a footprint of ≈0.048 cm^2, a nominal voltage of 1.7 V, an energy density of approximately 2.28 mWh/cm^2, a maximum power of 1.45 mW with an average power density of 26.88 mW/cm^2. These batteries provide sufficient power and energy density for millimeter-scale autonomous microsystems that are being actively developed for environment sensing applications [Hum01]. A battery integration method for autonomous microsystems has been proposed in Chapter 6.

5.1 Ni-Zn Battery Chemistry

The Ni-Zn batteries use nickel oxyhydroxide (NiOOH) as the cathode, zinc (Zn) as the anode, and aqueous potassium hydroxide (aq.KOH) as the electrolyte. When the batteries are charged, nickel (II) hydroxide is oxidized to nickel (III) oxyhydroxide and zinc (II) hydroxide is reduced to metallic zinc (0). When the batteries are discharged, nickel (III) oxyhydroxide is reduced to nickel (II) hydroxide and metallic zinc (0) is oxidized to zinc (II) hydroxide. The electrochemical reactions are as follows:

(1) Discharge

Cathode:

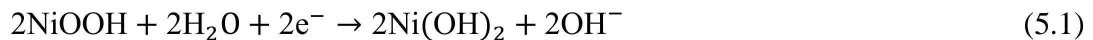

$$2NiOOH + 2H_2O + 2e^- \rightarrow 2Ni(OH)_2 + 2OH^- \quad (5.1)$$

Anode:

$$Zn + 2OH^- \rightarrow Zn(OH)_2 + 2e^- \quad (5.2)$$

Overall reaction:

$$2NiOOH + 2H_2O + Zn \rightarrow 2Ni(OH)_2 + Zn(OH)_2 \quad (5.3)$$

(2) Charge

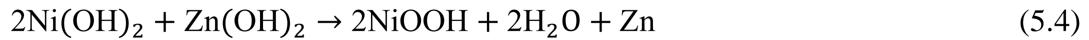

$$2Ni(OH)_2 + Zn(OH)_2 \rightarrow 2NiOOH + 2H_2O + Zn \quad (5.4)$$

The Ni-Zn battery reactions are represented in Figure 5.1. Solid lines represent the discharging reaction and broken lines represent charging reaction.

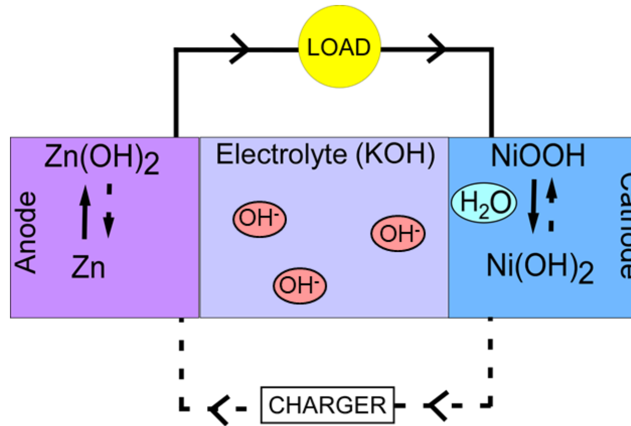

Figure 5.1: Representation of Ni-Zn battery reactions.

5.2 Microbattery Design

Figure 5.2 illustrates the design of the new microbattery that is amenable to batch mode fabrication in an array. This is a stacked electrode design and is chosen over side-by-side design as it provides better performance [Hum01]. Nickel oxyhydroxide (NiOOH) is used as the cathode and nickel foil as the positive current collector. Zinc foil is used for both the anode and the negative current collector. Polymer gel electrolyte is used as the electrolyte in this work because it prevents dendritic growth on zinc electrode surfaces during charge-discharge cycles. This leads to improved cycle performance compared to cells using KOH aqueous solution as an electrolyte [Iwa05]. There is no special separator required for nickel-based battery configurations [Hum01].

The nickel foil is 250 μm thick and has 150 μm deep cavities for filling the active cathode material. A 250 μm thick acrylic adhesive tape is used as an insulating middle layer and has perforations to accommodate the gel electrolyte. The final layer is a 250 μm thick Zn foil which has 100 μm deep recesses to accommodate the overflow of the electrolyte. The size of individual

battery is 2.2 mm × 2.2 mm × 0.75 mm with an active material area of 1.96 mm^2. The battery is self-packaged as the insulating tape serves as the battery sidewall. The design specifications of the microbatteries are summarized in Table 5.1.

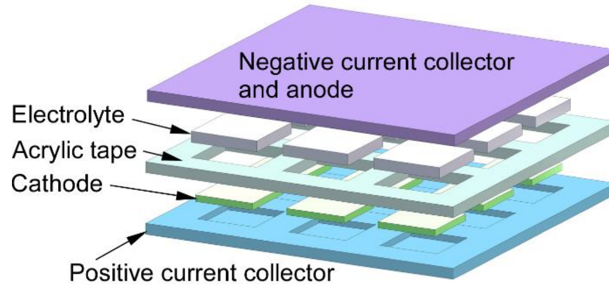

Figure 5.2: Design of microbattery for batch mode fabrication (3×3 array illustrated).

Table 5.1: Design Specifications of Ni-Zn microbatteries

Parameter	Value
Ni foil thickness	250 μm
Cathode thickness	150 μm
Zn foil thickness	250 μm
Tape thickness	250 μm
Cathode (Active material) area	1.96 mm^2
Array area	156.25 mm^2
Cell area	4.84 mm^2
Battery size	2.2×2.2×0.75 mm^3

5.3 Microbattery Fabrication

The fabrication process of the battery array is illustrated in Figure 5.3. The Ni and Zn foils were first machined by micro electrodischarge machining (μEDM), a process that is applicable to any conductive material. This machining process can be used in serial or batch mode [Tak02]. The machined Ni foil was attached to a glass carrier using wax for ease of handling in subsequent steps. The details on μEDM fabrication technology are presented in Appendix A of this dissertation.

The cathode paste was prepared by mixing $Ni(OH)_2$ powder (active material), cobalt powder (conductive material) and polyvinyl alcohol (binder solution) with a ratio of 10:1:6 by weight [Do04]. The $Ni(OH)_2$ powder will be oxidized into NiOOH during the initial battery

charging cycles. The cobalt powder was used as an additive to improve the ion conductivity of the cathode; this powder reacts with $Ni(OH)_2$ and forms the conductive CoOOH during the charging process [Bro97]. The cavities in the Ni foil were filled with cathode paste using a self-aligned damascene method. This method involved spreading the paste on the foil surface and then driving a squeegee across the foil surface to fill the cavities with the paste.

An acrylic adhesive tape patterned using a high throughput, low power laser cutting tool was aligned and attached to the Ni foil. This tape separates the current collectors as an insulating middle layer. It also serves as the battery sidewall, eliminating the need for a separate packaging process. The details on laser cutting technique are presented in Appendix A of this dissertation.

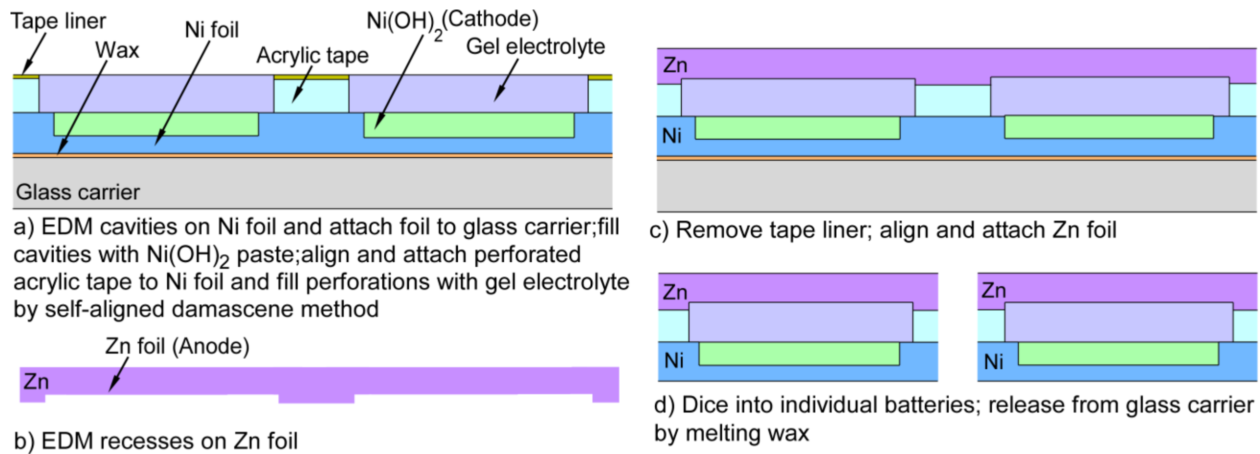

Figure 5.3: Fabrication process flow for an array of Ni-Zn microbatteries.

Polymer gel electrolyte was prepared by dissolving polyacrylic acid in 8 M KOH aqueous electrolyte with a weight ratio of approximately 1:200 and stirring the mixture until a homogenous gel was formed [Gai11]. Perforations in the tape were filled with this gel electrolyte using the self-aligned damascene method noted above. Subsequently, the Zn foil was aligned and attached to the stack. The recesses formed in the Zn foil by μEDM help reduce the overflow of electrolyte during this attachment. Finally, the array was cut into individual batteries using a dicing saw and then released from the glass carrier by melting the underlying wax.

5.3.1 *Micro Electro Discharge Machining of Ni and Zn Foils*

The nickel and zinc foils were machined using µEDM (SmalTec^{TM} EM203). This process was selected because it has high machining precision, especially useful to create cavities and recesses for accommodating the battery materials. A rotating tungsten electrode wire of 300 µm diameter was used as the cutting tool.

Photos of the machined Ni and Zn foils are shown in Figure 5.4(a) and (b) respectively. The machining of the two foils involved three steps each. For the Ni foil, the first step was to create nine 150 µm deep cavities in 250 µm thick foil. The distance between any two adjacent cavities was determined based on the individual battery size and the width required for dicing. The second step was to through-machine two dicing crosses on the foil which were later used for alignment during the assembly of the battery stack. In the final step, the entire foil (7.5 mm $\times$ 7.5 mm) was released to obtain the required dimension of the foil for the array. Similar procedure was followed to machine Zn foil. The depth of the cavities for Zn foil was 100 µm.

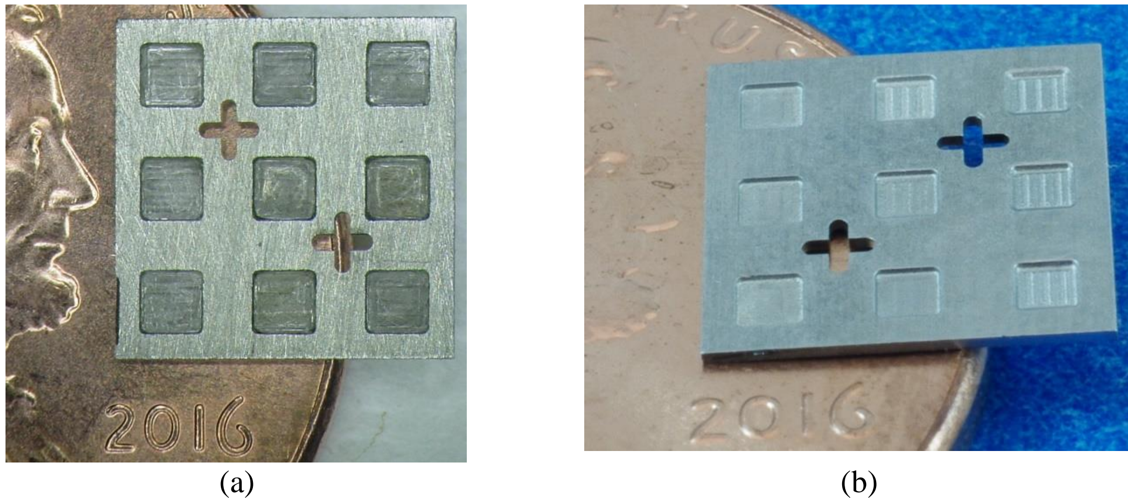

(a) (b)

Figure 5.4: Photos of (a) µEDM cavities in Ni foil (b) µEDM recesses in Zn foil.

5.3.2 *Laser Cutting of Acrylic Tape*

The acrylic adhesive tape was patterned and vector cut using a CO_2 laser (50 W Epilog Laser). The depth of the cut in Z-axis is determined by the setting for the laser's power, speed,

and frequency. The three parameters for vector cutting of the acrylic tape were optimized. The optimized speed was 50%, power was 50% and frequency was 2500 Hz. The photo of the patterned tape is shown in Figure 5.5. Through perforations were created in the tape to accommodate the gel electrolyte.

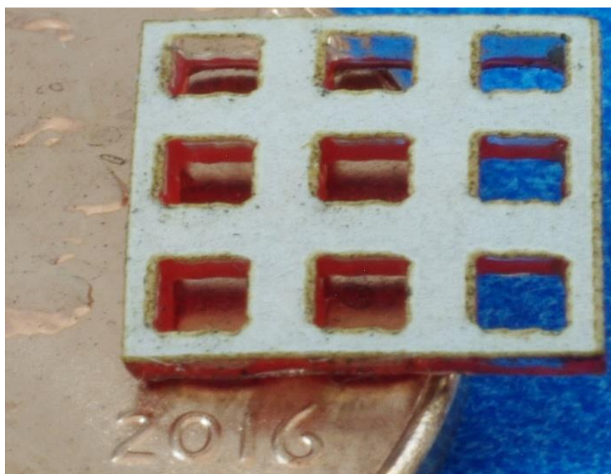

Figure 5.5: Photo of perforations in acrylic adhesive tape.

5.3.3 Fabricated Microbatteries

The assembled array was cut into individual batteries using a dicing saw (ADT 00777-1063-010-T04). The dicing parameters were optimized for the battery stack. The optimized feed rate was 0.5 mm/sec, spindle speed was 20,000 rpm, and it was cut in two passes. The photo of an array of fabricated microbatteries after dicing is shown in Figure 5.6. The microbatteries were released from the glass carrier by melting the underlying wax.

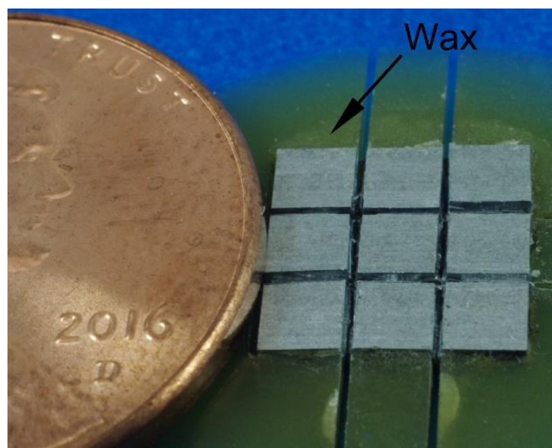

Figure 5.6: Photo of an array of fabricated microbatteries after singulation.

The batteries are cathode limited as the theoretical capacity of the zinc electrode is several times that of nickel oxyhydroxide electrode. The theoretical capacity of a Ni-Zn microbattery is calculated based on the mass of nickel hydroxide ($Ni(OH)_2$) used and the theoretical specific capacity of $Ni(OH)_2$. The theoretical specific capacity of $Ni(OH)_2$ is 289 mAh/g [Che99]. The mass of $Ni(OH)_2$ is calculated from its density and volume. The density of $Ni(OH)_2$ is 4.1 g/cm^3 [Che99]. The volume of $Ni(OH)_2$ calculated from its area and thickness is 0.294 mm^3. The estimated mass of $Ni(OH)_2$ is 1.205 mg. Equation 5.5 is used to calculate the theoretical capacity. The theoretical capacity of a Ni-Zn microbattery is estimated to be 346.8 μAh.

$$Theoretical\ capacity = Theoreticel\ specific\ capacity\ \times Mass \qquad (5.5)$$

5.4 Experimental Results

The fabricated batteries were tested by charging and discharging with constant current using the BT2043 battery test instrument from Arbin Instruments, LLC (College Station, TX, USA). Figure 5.7 shows the measured capacity of 3 batteries in 10 cycles of charging and discharging. These batteries were fabricated in the same 3×3 battery array. The nine batteries from this array were all tested and assigned battery ID B1-9. As shown in the figure, the batteries could be charged and discharged for at least ten cycles at charge/discharge rates of 0.1 C (i.e. 10%

of the calculated theoretical capacity per hour), which corresponds to a current of 34.6 µA based on the theoretical capacity of 346 µAh for the battery in this work. For all cycles, the charge time was 2 hours and the discharge was stopped when the battery voltage dropped to 1.2 V.

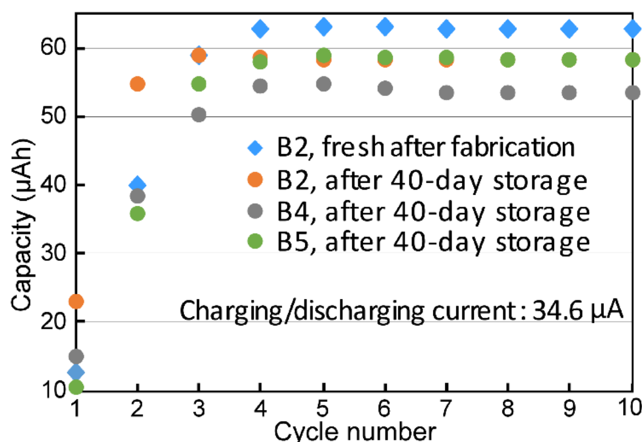

Figure 5.7: Measured capacity by cycle number for three different battery samples.

The formation reaction occurred in the batteries for the initial 3 charge/discharge cycles. During this process, $Ni(OH)_2$ in the cathode was oxidized into NiOOH. This oxidation caused the battery capacity to increase during the initial 3 cycles. The charge/discharge properties of the battery were stabilized after the 3rd cycle and thus the battery capacity remained stable. Figure 5.7 also shows the comparison of the capacity of the batteries B2, B4 and B5. B2 was tested both immediately after the fabrication and after 40 days of storage at room temperature. The capacity reduced by <7% after 40 days in storage. The capacity reduction was due to the partial conversion of α-$Ni(OH)_2$ to β-$Ni(OH)_2$ during storage [Che99]. B4 and B5 were tested after 40 days of storage. The capacity of these two batteries was comparable to that of B2 after the storage. Figure 5.8 shows the charge/discharge curves for the sixth cycle for B2 tested immediately after fabrication. As the battery was being discharged, the battery voltage decreased continuously, typical of a Ni-Zn battery. A voltage regulation chip can be used with the battery to obtain a constant output voltage if necessary. The maximum capacity was 63.16 µAh, corresponding to an energy density of approximately 2.28 mWh/cm^2.

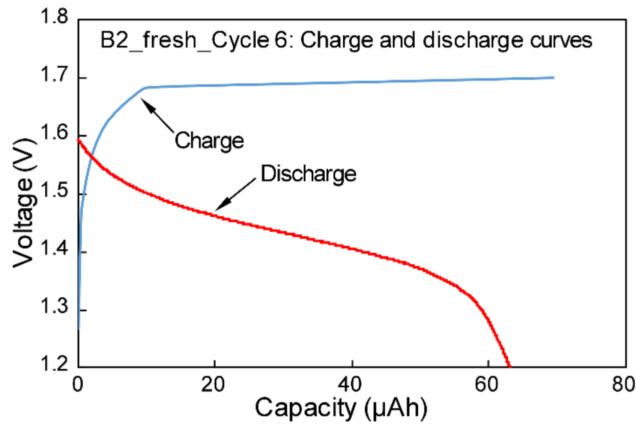

Figure 5.8: Measured charge/discharge curves for the 6th cycle of B2 tested immediately after fabrication.

Figure 5.9 shows the capacity curves for the battery B5 which was discharged in multiple cycles with an increasing C-rate from 0.1 C to 2.88 C (corresponding to a discharging current ranging from 34.68 µA to 1 mA). For all cycles, charging was performed at the current level of 0.1 C, and discharge was stopped when the battery voltage dropped to 1.2 V. The decrease in capacity with increasing discharge current is expected, which is partly caused by larger internal resistance at higher current. The discharge at 1 mA current lasted for approximately 38 seconds. This gives a maximum power of 1.45 mW and an average power density of 26.88 mW/cm^2, which is sufficient to power many autonomous microsystems [Hum01]. The performance characteristics of the microbatteries are summarized in Table 5.2.

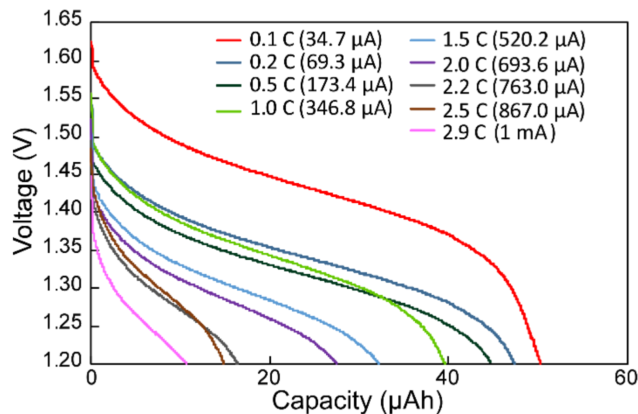

Figure 5.9: Discharge voltage curves at various discharge currents.

Table 5.2: Specifications of Ni-Zn microbatteries

Chemistry	Nickel-zinc
Nominal voltage	1.7 V
Measured capacity	≤63.16 μAh
Capacity density	≤1.31 mAh/cm^2
Energy density	≤2.28 mWh/cm^2
Max. discharge current tested	1 mA
Maximum power @1 mA	1.45 mW
Average power density @1 mA	26.88 mW/cm^2

5.5 Discussion and Summary

The process described in this paper is attractive because: 1) the nickel, zinc and the acrylic tape are commercially available in the necessary forms; 2) the electrolyte does not require an oxygen-free environment, which increases the ease of manufacturing; 3) the battery does not require a separate negative current collector as the zinc foil serves as both the anode material and the negative current collector; 4) the cathode and electrolyte materials are integrated using a self-aligned damascene method, without the need of specialized equipment for lithography and thin film deposition typically used in other microbattery development.

Several challenges were addressed to successfully implement this process. These include the lack of adequate adhesion between the tape and the Ni foil, the proper preparation and handling of the battery cathode and electrolyte materials in a way that would not degrade the performance of the fabricated battery, and a proper dicing procedure for the hybrid stack of metal foils at such a small footprint.

Table 5.3 shows a comparison of various Ni-Zn microbatteries published in the literature. The energy density of the batteries presented in this work is substantially superior to previously reported Ni-Zn microbatteries, providing an additional benefit to this process. The superior energy density is attributable to the structural design and material choices. In particular, the dimensions and material choices of the cathode and electrolyte are significant contributing factors.

Table 5.3: Comparison of this work with other published work on Ni-Zn microbatteries in literature

Work	Typical process used	Cell area (cm^2)	Capacity density (normalized by cell area) (mAh/cm^2)
This work	Self-aligned damascene method	0.048	1.31
3-D Ni-Zn microbatteries [Cha07]	Micromolding of high aspect ratio electrodes using DRIE-etched holes in Si substrate; electroplating of electrode materials	0.25	0.0025
Microscopic Ni-Zn batteries [Hum01]	Electron beam evaporation; electroplating and photolithography patterning of current collectors	0.02	0.389
Ni-Zn battery with polymer hydrogel electrolyte [Ika05]	Electrodeposition; not batch mode	-	- (Specific capacity: 100 mAh/g)
Ni-Zn battery with hybrid hydrogel electrolyte [Ino14]	Paste electrodes; not batch mode	-	- (Capacity: 5 mAh)

In Ni-based rechargeable batteries, the battery capacity is generally limited by the NiOOH electrode [Bro97]. To increase the battery energy density, it is necessary to increase the energy density of NiOOH electrode. Powdered NiOOH with smaller crystallite size is expected to provide better electrode characteristics such as lower overpotential and higher capacity [Che99].

The use of gel electrolytes in batteries is typically helpful in improving reliability, safety, flexibility and processability [Ika05]. The polyacrylic acid in the polymer gel electrolyte used in this work suppresses the dissolution and diffusion of $Zn(OH)_4^{2-}$ ions in the alkaline solution. In contrast, in aqueous alkaline electrolyte, $Zn(OH)_4^{2-}$ ions are highly soluble and the transport of these ions results in the shape change of the zinc electrode, leading to poor charge–discharge characteristics.

Powdered Co^{2+} was used as an additive in the cathode in this work. The utilization of $Ni(OH)_2$ with additives of Ca^{2+}, Co^{2+} and Zn^{2+} was compared at 25°C, and Co^{2+} was found to have better utilization than Zn^{2+}, which is in turn better than Ca^{2+} [Har02]. The Co^{2+} additive forms conductive CoOOH during the charging process, thus leading to higher utilization. Utilization is defined as the ratio of the actual discharge capacity to the theoretical discharge capacity. For

applications requiring higher temperatures, such as 60˚C, it was shown that the nickel hydroxide electrode containing Ca^{2+} provided the highest utilization because it could provide the largest difference between the potential of oxygen evolution and the oxidation potential [Har02]. Therefore, for applications requiring wider temperature ranges, Ca^{2+} should be used instead of Co^{2+} as the additive in the cathode. Adding the Zn^{2+} additive is optional; it could improve the cycle life of the battery as it could help reduce the formation of γ-NiOOH. γ-NiOOH is one of the four observed phases of a nickel hydroxide electrode: β-$Ni(OH)_2$, β-NiOOH, γ-NiOOH, and α-$Ni(OH)_2$ [Bod66]. Volume expansion of the nickel hydroxide electrode occurs when the phase changes from β-NiOOH to γ-NiOOH [Sin98] and this expansion increases the electrode resistance for charging-discharging at high rates.

This work describes a batch fabrication approach for planar microbatteries that utilizes low cost materials and methods while still delivering high performance. Multiple 3×3 arrays of Ni-Zn microbatteries were successfully fabricated. The process also allows scaling-up for manufacturing large arrays of microbatteries. The fabricated batteries have a typical footprint of ≈0.048 cm^2 and a capacity of ≈63 μAh, providing sufficient power and energy density for many millimeter-scale autonomous microsystems. For example, these microbatteries are suitable to be used in a hybrid micropower supply for autonomous microsystems [Har02]. Such hybrid power supplies would include an energy scavenging device, rechargeable microbatteries and control/interface circuitry, and could potentially provide the benefits of long lifetime and reduced system size.

CHAPTER 6: Conclusions and Future Work

This chapter summarizes the efforts of investigating critical elements of system design and package integration for environmental sensing autonomous microsystems, specifically for pipeline monitoring and downhole monitoring applications. Then, major contributions to the microsystems field are listed. Future work regarding (i) environment logging microsystem for downhole operation up to 125°C and (ii) battery integration method for autonomous microsystems is proposed.

6.1 Summary and Major Contributions

This dissertation advances the technology of the environmental logging microsystem (ELM) platform to enable its use for applications such as pipeline monitoring and downhole monitoring.

Towards the first specific goal of investigating the system level design compromises and overall performance limits for autonomous microsystems, environmental logging microsystems (ELM6 and ELM7) were developed for pipeline monitoring and downhole monitoring applications, respectively. For monitoring oil and gas pipelines, 1) the system was required to achieve temperature logging up to 60°C and a preferred resolution of 0.5°C, pressure logging up to 10 MPa and a preferred resolution of 2 kPa, and inertial data logging; 2) the system size was required to be restricted to centimeter scale to permit monitoring of small diameter pipelines; 3) the system power consumption had to be low; 4) between deployments, the system required to accommodate wireless recharging of the battery as well as wireless communication with the external user. Keeping these targets in mind, the ELM6 was designed to achieve temperature,

pressure, and inertial data logging using smallest suitable off-the-shelf electronic and battery components compatible with assembly on a flexible PCB. It used resonant inductive charging and BLE protocol for communication. The designed system stack size was 15.4×14.2×11.2 mm^3. The system was successfully tested at up to 65°C and 12 MPa. It had a standby current of 8 µA at room temperature and the system lifetime was >10 days when operated at room temperature with detection interval of 12 hours.

For downhole monitoring, 1) the design targets included an upper limit for operating temperature of ≥75ºC and a preferred resolution of 0.1°C, an upper limit for operating pressure of ≥15 MPa and a preferred resolution of 0.5 kPa; 2) between deployments, the system required to accommodate wireless recharging of the battery as well as wireless communication with the external user; 3) the system had to record inertial sensor data, limit memory usage, operate at low power, and be able to re-use PCB should the battery become non-functional. The ELM7 achieved temperature, pressure, and inertial data logging using the smallest suitable off-the-shelf electronic components assembled on a PCB with a footprint of 5.6 cm^2. Qi protocol based wireless charging and BLE communication protocol were implemented for this system. The ELM7 was successfully tested up to 85°C and up to 160°C for all elements excluding the battery.

Towards the second specific goal of investigating a package integration approach to permit deployment, retrieval, and reusability of downhole sensing microsystems, ELM7 was encapsulated in a flow-compatible package. The package integration approach needed to: 1) protect the system electronics from harsh environmental factors such as corrosive chemicals and abrasion and impact events while permitting the transfer of external pressure onto the ELM7 sensors; 2) allow wireless charging and wireless communication; 3) allow maintaining a density of less than 1.2 g/cc; 4) enable the retrieval and reusability of the system hardware when the package was unsealed and

opened. These goals were achieved by designing the ELM7 electronics, power source, and sensors to fit within a flow-compatible package designed to operate within oil well bores. This required the proper positioning of the pressure sensor, wireless charging coil, and BLE MCU on the PCB. Based on the above considerations, the design targets for the system package were an upper limit for operating pressure of ≥15 MPa, an upper limit for operating temperature of ≥75ºC, packaged system size ≤25 cm^3, and packaged system density ≤1.2 g/cc. The package was custom injection molded using Viton™, a high temperature tolerant and high chemical resistance material. The ELM7 PCB along with battery, were secured inside a high temperature thermoplastic bag filled with non-conductive oil and placed into the package. The package was then filled with low bulk density cenospheres to reduce the effective density and permit pressure transfer to the ELM. The packaged systems had a volume of <25 cm^3 and density <1.2 g/cc. Active microsystems with temperature, pressure, and inertial sensors were encapsulated in these packages, and successfully tested in laboratory conditions tested up to 85°C and 41.5 MPa for more than 4 days. The microsystems were also successfully tested in the field, conducted by deployment of microsystems into an operational oil well to a depth of 1,290 m. Temperature, pressure, and inertial data were recorded, matching expected conditions in the downhole environment during deployment. To our knowledge, this was the first successful demonstration of autonomous microsystem deployment into an operational oil well in which data was successfully collected.

Table 6.1 summarizes the features of ELM6 and ELM7 developed in this work along with the previous generations of ELM (ELM1, ELM2, and ELM3). ELM6 was developed for pipeline monitoring and the remaining ELMs were developed for downhole monitoring application.

Table 6.1: Summary of all the generations of ELM

Features	ELM1	ELM2	ELM3	ELM6	ELM7
P logging	No	Yes	Yes	Yes	Yes
P range (psi / MPa)	-	7200 / 50	7200 / 50	10,000 / 70	10,000 / 70
P resolution (psi / kPa)	-	0.3 / 2	0.3 / 2	0.3 / 2	0.07 / 0.5
T logging	Yes	Yes	Yes	Yes	Yes
T range (ºC) (operated)	25 to 125	25 to 125	25 to 125	25 to 60	25 to 85
T resolution (ºC)	0.5	0.5	0.5	0.5	0.1
IMU	No	No	No	Yes	Yes
Acc. dynamic range (g)	-	-	-	±8 g	±8 g
Acc. resolution	-	-	-	0.244 mg/LSB	0.244 mg/LSB
Mag. dynamic range (gauss)	-	-	-	±16 gauss	±16 gauss
Mag. resolution	-	-	-	0.58 mgauss/LSB	0.58 mgauss/LSB
Communication	LED	LED	LED	BLE	BLE
Power switch & improved manufacturing	No	No	Present	Present	Present
Battery recharging	Optical	Optical	Optical	Resonant inductive (Qi)	Resonant inductive (Qi)
Battery max. voltage	3.1 V	3.1 V	3.1 V	3.1 V	4.1 V
MCU operating frequency	32.768 kHz	32.768 kHz	32.768 kHz	32.768 kHz (core) 38 MHz (BLE)	32.768 kHz (core) 38 MHz (BLE)
Active current	150 μA @125ºC	150 μA @125ºC	150 μA @125ºC	BLE: 13 mA (Rx) 11 mA (Tx) @RT	6.2 mA (det.) @150ºC
Standby current	12 μA @125ºC	12 μA @125ºC	12 μA @125ºC	8 μA @RT	-
Max stored data points (all sensors active)	1270	1270	1270	4664	4200
Integration topology	Polyimide flexible PCB	Polyimide flexible PCB	Polyimide flexible PCB	Polyimide flexible PCB	FR4 rigid PCB
Designed PCB stack size	6.5×6.3×4.5 mm^3	6.5 × 6.5 × 5.8 mm^3	8.8 × 8.6 × 7.2 mm^3	15.4×14.2×11.2 mm^3	5.6 cm^2 (footprint)
Packaging topology	Stainless steel shell with sapphire lid	Stainless steel tube filled with polymer	Polymer mold	-	Viton tube filled with cenospheres
Packaged system size	8.9×8.9×6.85 mm^3	9.5×9.5×6.5 mm^3	29 × 8.8 × 3.0 mm^3	-	≈25 cm^3
Lifetime (Days)	0.5 @125ºC	1 @125ºC	1 @125ºC	>10 @25ºC	>4 @85ºC

Towards the last specific goal of investigating a scalable fabrication method for incorporating microbatteries within autonomous microsystems, a batch mode fabrication process for high capacity rechargeable nickel-zinc microbatteries was developed. Micro electro discharge machining (µEDM) was used to define arrays of cavities in foils of Ni and Zn. The cathode and electrolyte materials were incorporated using a self-aligned damascene method. The fabricated batteries had a footprint of ≈0.048 cm^2, a nominal voltage of 1.7 V, a typical capacity of ≈63 µAh corresponding to an energy density of approximately 2.28 mWh/cm^2, a maximum power of 1.45 mW with an average power density of 26.88 mW/cm^2. These batteries can provide sufficient power and energy density for millimeter-scale autonomous microsystems that are being actively developed for environment sensing applications.

System Highlights

A. Wireless autonomous microsystems for environmental logging applications

- a. System state machine for low power operation
- b. Resonant inductive charging (Qi) and RF communication (BLE)
- c. Temperature, pressure, and inertial sensing
- d. Demonstrated operation up to 60°C and 12 MPa (ELM6) and 85°C (ELM7)

B. Packaged microsystems for downhole sensing application

- a. Flow-compatible package to permit deployment, retrieval, and reusability of downhole sensing microsystems
- b. Demonstrated operation up to 85°C and 41.5 MPa for >4 days in lab conditions
- c. Demonstrated operation in operational oil well to a depth of 1,290 m

C. Scalable fabrication method for microbatteries.

- a. Facile batch mode process for nickel-zinc microbatteries
- b. Structural design and materials for cathode and electrolyte provide superior energy density of the batteries

6.2 Future Work

This dissertation provides the path forward for research work in broadly three areas: (i) microsystem design and integration; (ii) microsystem package integration; and (iii) microbatteries. The various aspects of the microsystems presented in Chapters 2 and 3, including wireless charging, power management, sensing, and communication can be adapted for sensing microsystems for medical, consumer, industrial, and several other applications. An environmental logging microsystem (ELM8) for downhole operation up to 125°C is proposed in Section 6.2.1. The features of the packaging approach presented in Chapter 4, including flow-compatibility, physical coupling to the environment, and reusability of the system hardware can be adapted for harsh environment sensing microsystems for marine, automotive, and other applications. The microbatteries presented in Chapter 5 can be used for microsystems that are being actively developed for health and wellness, as well as environmental applications. A 3D functional microsystem package with embedded microbatteries is proposed in Section 6.2.2.

6.2.1 Environment Logging Microsystem for Downhole Operation up to 125•C

As discussed in Chapter 3, the limitation of ELM7 was the incompatibility of the rechargeable battery at elevated temperature (>85°C). The rechargeable battery had a rated temperature range up to 85°C [Tad18] and operating it beyond the temperature specification would significantly degrade the battery performance and reduce the battery life. The electronics and sensors of the system, however, were demonstrated to operate up to 160°C. As described in Chapter 1, for oil reservoirs that are typically 0.6-6 kilometers deep underground, the typical downhole environment temperature is ≥75ºC and pressure is ≥15 MPa [Cha12]. The proposed ELM8 could use a large capacity primary battery rated for higher temperatures (125°C) to power the system during deployment and Qi wireless power transfer to power the system during data

transfer or when the battery is depleted. This system can utilize an improved power management circuit to further reduce the standby current and improve system lifetime.

6.2.2 Battery Integration Method for Autonomous Microsystems

As discussed in Chapter 5, integration of the power source within the microsystem package is usually a challenge, particularly for applications with a constraint on the size of the microsystem. The Ni-Zn microbatteries developed in Chapter 5 provide sufficient power and energy density for millimeter-scale autonomous microsystems that are being actively developed for applications such as environment sensing. A 3D functional microsystem package with embedded microbatteries has been proposed here.

The package consists of a 3D printed shell, four Ni-Zn batteries, an outer connector copper foil, and an inner connector copper foil (Figure 6.1(a)). The batteries are connected in parallel to provide sufficient capacity to power the entire system. The outer connector foil connects the positive terminals of the batteries electrically and the inner connector foil provides electrical connection to the negative terminals. The connector foils have pads situated on the bottom surface of the shell that are used to make electrical connection with the system PCB (Figure 6.1(b)). The package shell structure contains cavities for embedding the batteries and recesses to accommodate the connector foils (Figure 6.2(a)). The connector foils will be obtained by patterning a planar copper foil using μEDM and folding the patterned foil into a loop. Both the foils will contain four battery contact pads and one system PCB contact pad. The outer connector foil will be assembled inside the 3D printed package shell, followed by batteries and then the inner connector foil.

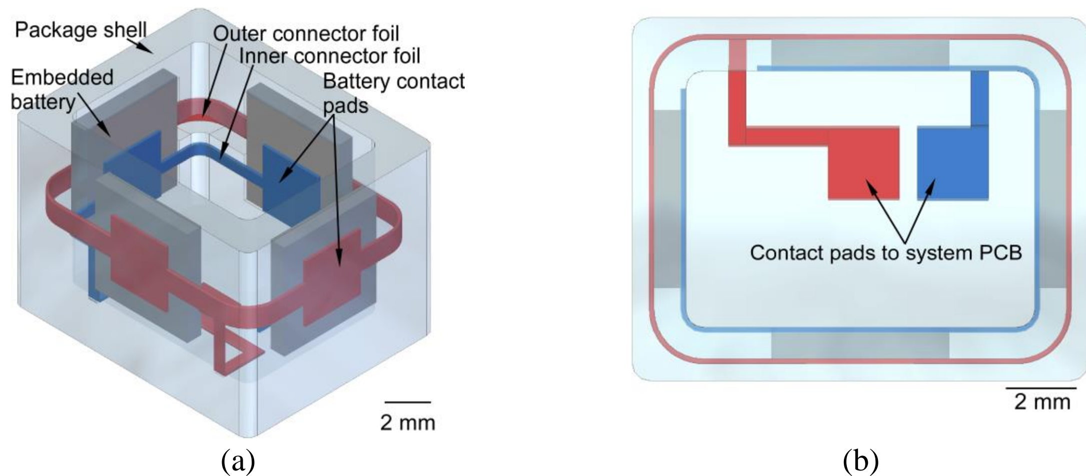

Figure 6.1: (a) Overall package design including batteries, connector foils, and 3D printed shell. (b) Top-down view of the overall package.

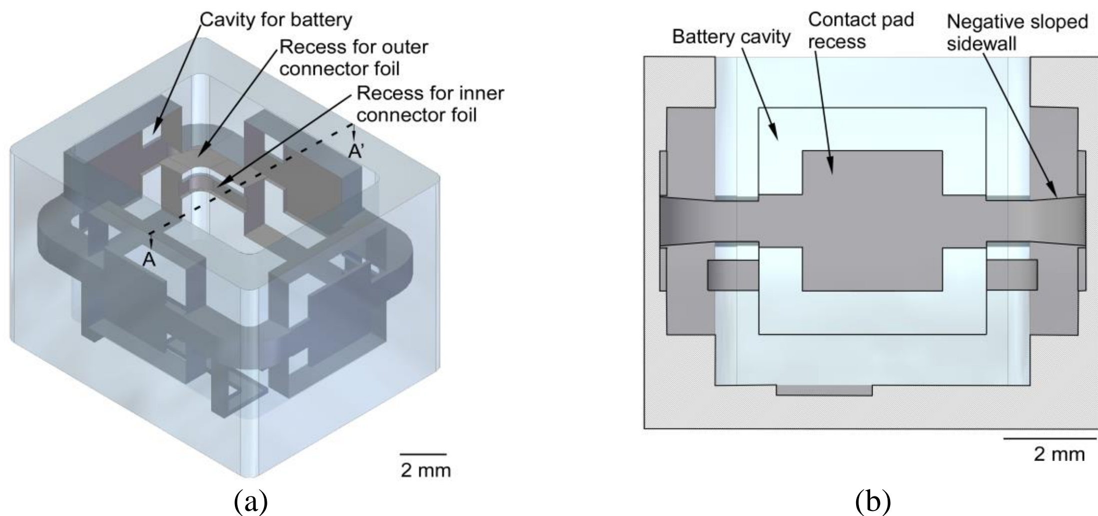

Figure 6.2: (a) Model of the 3D printed package shell; (b) cut-off view (AA') indicating the design features in the 3D printed package shell.

The batteries can be connected in series or in parallel to configure either the total capacity or net voltage based on the application. The dimensions of the batteries can be scaled with the fabrication approach described in Chapter 5, and dimensions of the package shell can be scaled without any additional cost due to the use of mask-less digital process of additive manufacturing. The rapid prototyping 3D printing method combined with the facile battery fabrication and integration approach will provide a high throughput and low-cost option for functional packaging of sensing microsystems for various applications.

APPENDIX A: Relevant Technologies

Micro electro-discharge machining (µEDM) and laser cutting are the non-traditional fabrication technologies used in this work. µEDM enables fabrication in sub-millimeter size through an electro-thermal process. Laser cutting utilizes a laser to cut materials, resulting in high quality, dimensionally accurate cuts. These technologies can be implemented in batch mode and can therefore potentially increase fabrication throughput.

A1.1. Micro Electro Discharge Machining (µEDM)

Electro-discharge machining (EDM) is an electro-thermal based non-traditional machining process, where electrical energy is used to generate electrical spark and material removal mainly occurs due to the thermal energy of the spark. It is mostly used to machine hard metals that are difficult to be machined by other methods. Micro electro-discharge machining (µEDM) is its miniature version which complements other MEMS processes. It is applicable to conductors as well as semi-conductors. µEDM was first demonstrated by Kurafuji and Masuzawa in 1967 when they machined a 9 µm hole in 50 µm thick cemented carbide alloy [Kur68]. The µEDM process utilizes an electrode (tool) and the material to be machined (sample or workpiece). It removes the unnecessary volume of the workpiece by repetitively generating fine discharge sparks between the electrode and the sample. The pulse discharge timing is controlled by a resistance–capacitance (RC) circuit. Dielectric oil or deionized (DI) water are usually used to as the fluid to flush away metal debris generated during machining.

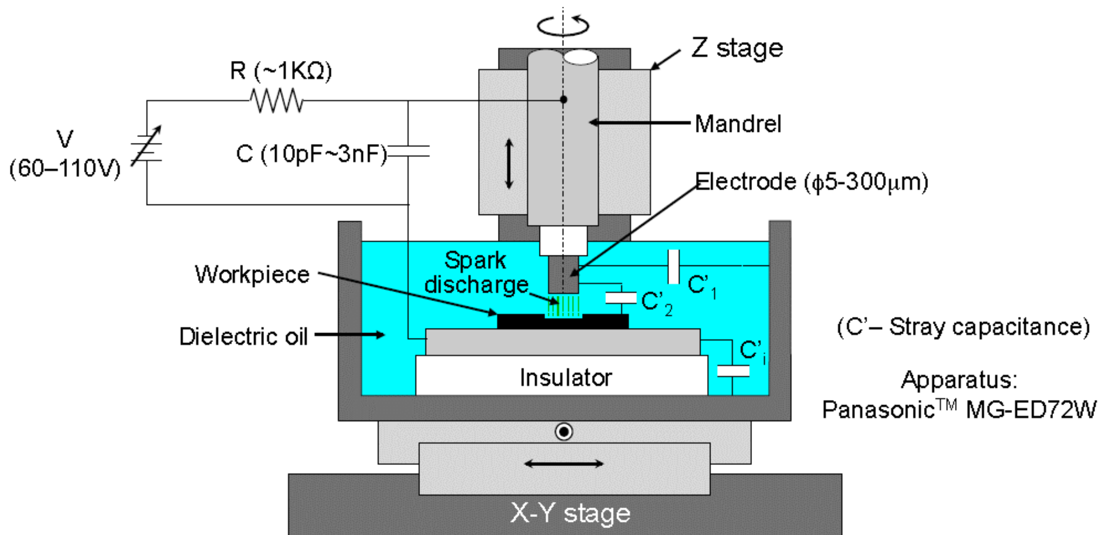

Figure A.1: Schematic drawing of the basic setup of μEDM unit [Tak02].

In traditional μEDM, the tool is a wire which is rotated and continuously fed into the workpiece. Rotating the electrode prevents it from depositing onto the workpiece during machining and facilitates in removing the debris. It is continuously fed to compensate for the tool wear. The diameter of the wire is small and is formed by a method known as wire electro-discharge grinding (WEDG). The discharge gap and the diameter of the wire define the minimum cavity size. Discharge gap as low as 1 μm was achieved in [Mas90]. Discharge energy affects the machining speed and the surface finish of the machined workpiece. Higher discharge energy leads to higher machining speed but produces rougher workpiece surface.

Traditional μEDM uses single electrodes and is basically a serial fabrication method; hence it has limited throughput. There will also be a variation in the electrode shape between electrodes. There has been work done to enable batch mode μEDM through electrode arrays to increase the machining throughput. LIGA process was used to make copper electrode arrays and fabricate thirty-six WC-Co gears with 300 μm outer diameter and 70 μm thickness in parallel within 15 min [Tak02]. High-aspect-ratio silicon microstructures with fine feature sizes formed by deep reactive-ion etching (DRIE) were used as cutting electrodes in batch mode to precisely micromachine metal

alloys such as stainless steel [Li13]. Minimum feature size of 7 μm, aspect ratio up to 3.2, and machining rate up to 5 μm/min in feature depth were demonstrated.

A1.2. Laser Cutting

Laser cutting is a non-contact process which utilizes a laser to cut materials, resulting in high quality, dimensionally accurate cuts. The process works by directing the laser beam through a nozzle to the workpiece. A combination of heat and pressure creates the cutting action. The material melts, burns, vaporizes, or is blown away by a jet of gas, leaving an edge with a high-quality surface finish.

The depth of the cut in Z-axis is determined by the setting for the laser's power, speed, and frequency. These three parameters are different for different materials. Thinner materials that are easier to cut through, like paper, require less power to cut and must use a slower speed and frequency to ensure the heat of the laser does not cause the material to burn. Thicker, denser materials, like wood, require higher power, speed, and frequency settings and absorb more heat from the laser before burning. There are two types of cuts that can be made to any material: raster cuts and vector cuts. Raster cuts are less powerful cuts made to engrave the surface of the material. Vector cuts are the more powerful cuts that completely cut through the material.

References

[Aky02] I.F. Akyildiz, W. Su, Y. Sankarasubramaniam, and E. Cayirci, "Wireless Sensor Networks: A Survey," *Computer Networks* 38, pp. 393–422, 2002.

[Al98] S. F. Al-sarawi, D. Abbott, and P. D. Franzon, "A Review of 3-D Packaging Technology," *IEEE Transactions on Components, Packaging, and Manufacturing Technology – Part B*, Vol. 21, No. 1,1998.

[Alb08] F. Albanoa, Y.S. Lin, D. Blaauw, D.M. Sylvester, K.D. Wise, and A.M. Sastry, "A fully integrated microbattery for an implantable microelectromechanical system," *J. Power Sources,* 185(2), pp. 1524-1532, 2008.

[All03] R. Allan, "MEMS Gaining Acceptance Despite Technical Challenges," *Electronic Design*, vol. 51, pp. 23-26, 2003.

[Arm11] A. Armutlulu, Y. Fang, S. H. Kim, C. H. Ji, S. A. Allen, and M. G. Allen, "A MEMS-Enabled 3D Zinc–Air Microbattery with Improved Discharge Characteristics Based on a Multilayer Metallic Substructure," *J. Micromech. Microeng*. 21, 104011, 2011.

[Asp17] G. Aspar, B. Goubault, O. Lebaigue, J-C. Souriau, G. Simon, L. Di Cioccio, and Y. Bréchet, "3D Printing as a New Packaging Approach for MEMS and Electronic Devices," *IEEE 67th Electronic Components and Technology Conference*, pp. 1071-1079, 2017.

[Bab18] M. B. Babenkov, "Temperature of rock formation and fracturing fluid during the hydraulic fracturing process," *IOP Conf. Series: Earth and Environ. Science* 193, 012076, 2018.

[Bas16] H. Basaeri, D. B. Christensen, and S. Roundy, "A Review of Acoustic Power Transfer for Bio-Medical Implants," *Smart Mater. Struct.*, 25, 123001, 2016.

[Bat00] J.B. Bates, N.J. Dudney, B. Neudecker, A. Ueda, and C.D. Evans, "Thin-film lithium and lithium-ion batteries," *Solid State Ionics*, 135, pp. 33–45, 2000.

[Ben19] A. C. Benken, *A High-Yield Microfabrication Process for Sapphire Substrate Pressure Sensors with Low Parasitic Capacitances and 200°C Tolerance*, Ph.D. dissertation, Univ. Michigan, An Arbor, MI, USA, 2019.

[Blu15] *Bluetooth*, https://en.wikipedia.org/wiki/Bluetooth, accessed on Nov. 28, 2015.

[Boc89] Boca Raton, *CRC Handbook of Chemistry and Physics*, 70th Edition, R. C., Ed., CRC Press, p. D-221, 1989.

[Bod66] H. Bode, K. Dehmelt, and J. Witte, *Electrochim. Acta*, 11, 1079-1087, 1966.

[Bra09] C. S. Branch, “Limits of Human Exposure to Radiofrequency Electromagnetic Energy in the Frequency Range from 3 kHz to 300 GHz,” *Safe Code* 6, 2009.

[Bro97] J. Brown and M. Klein, “Design factors for a super high energy density Ni-MH battery for military uses,” *12th Annual Battery Conference on Application and Advances*, pp. 33-36, Jan. 1997.

[Can15] G. Canavese, L. Scaltrito *et al.*, “A Novel Smart Caliper Foam Pig for Low-Cost Pipeline Inspection – Part A: Design and Laboratory Characterization,” *Journal of Petroleum Science and Engineering,* 127, pp. 311–317, 2015.

[Cha07] F. Chamran, Y. Yeh, H. Min, B. Dunn, and C. Kim, “Fabrication of high-aspect-ratio electrode arrays for 3D microbatteries,” *IEEE/ASME J. Microelectromechanical Systems*, 16(4), pp. 844-852, 2007.

[Cha18] *Wi-Charge*, http://www.wi-charge.com/technology/, accessed on Nov. 28, 2018.

[Cha12] D. Chapman and W. Trybula, “Meeting the challenges of oilfield exploration using intelligent micro and nano-scale sensors,” in *12th IEEE International Conference on Nanotechnology*, Birmingham, UK, 2012.

[Che11] G. Chen, H. Ghaed, R. Haque, M. Wieckowski, Y. Kim, G. Kim, D. Fick, D. Kim, M. Seok, K.D. Wise, D. Blaauw, and D. Sylvester, “A cubic-millimeter energy-autonomous wireless intraocular pressure monitor,” *Intl. Solid-State Circuits Conference*, San Francisco, pp. 310-312, 2011.

[Che99] J. Chen, D.H. Bradhurst, S.X. Dou, and H.K. Liu, “Nickel hydroxide as an active material for the positive electrode in rechargeable alkaline batteries,” *J. Electrochemical Society*, 146(10), pp. 3606-12, 1999.

[Cho17] M. Choi, Y. Sui, I.H. Lee, R. Meredith, Y. Ma, G. Kim, D. Blaauw, Y. B. Gianchandani, and T. Li, *Autonomous Microsystems for Downhole Applications: Design Challenges, Current State, and Initial Test Results*, *Sensors*, 17, 2190, Sep. 2017.

[Coo46] R. Cooper, “The Electrical Properties of Salt-Water Solutions Over the Frequency Range 1-4000 Mc/s”, *The Journal of the Institution of Electrical Engineers*, March 1946.

[Den10] A. Denisov, and E. Yeatman, “Ultrasonic vs. inductive power delivery for miniature biomedical implants,” *Proc. Int. Conf. Body Sens. Netw.*, pp. 84–89, June 2010.

[Do04] J. Do, S. Yu, and S. Cheng, “Preparation and characterization of thick-film Ni/MH battery,” *Biosensors and Bioelectronics*, 20(1), pp. 61-67, 2004.

[Dou12] D. Doughty and E.P. Roth, "A General Discussion of Li Ion Battery Safety," *The Electrochemical Society Interface*, Vol. 21, No. 2, pp. 37-44, Jun. 2012.

[Dup19] *Dupont*, https://www.dupont.com/, accessed on Nov. 20, 2019.

[Elk16] M. Elkhodr, S. Shahrestani, and H. Cheung "Emerging Wireless Technologies in the Internet of Things: A Comparative Study," *International Journal of Wireless & Mobile Networks*, Vol. 8, No. 5, Oct. 2016.

[Ell07] D. Ellis and J. Singer, *Well Logging for Earth Scientists*, Springer, 2007.

[Esp14] D. Espalin, D. W. Muse, E. MacDonald, and R. B. Wicker, "3D Printing Multifunctionality: Structures with Electronics*," The International Journal of Advanced Manufacturing Technology*, Vol. 72, pp. 963-978, 2014.

[Fai16] F. K. Shaikh, and S. Zeadally, "Energy Harvesting in Wireless Sensor Networks: A Comprehensive Review," *Renewable and Sustainable Energy Reviews*, 55, pp 1041-1054, 2016.

[Far17] M. F. Farooqui, M. A. Karimi, K. N. Salama, and A. Shamim "3D-Printed Disposable Wireless Sensors with Integrated Microelectronics for Large Area Environmental Monitoring," *Adv. Mater. Technol.*, 2, 1700051, 2017.

[Fin10] J. Finger and D. Blankenship, "Handbook of best practices for geothermal drilling," *Sandia Nat. Labs*., Albuquerque, NM, USA, and Livermore, CA, USA, Dec. 2010.

[Fle08] R. Fletcher and M. Chandrasekaran, "Smartball^{TM} - A New Approach in Pipeline Leak Detection," *7th International Pipeline Conference*, Alberta, Canada, 2008.

[Flo17] P. F. Flowers, C. Reyes, S. Ye, M. J. Kim, and B. J. Wiley, "3D printing electronic components and circuits with conductive thermoplastic filament," *Additive Manufacturing*, 18, pp. 156–163, 2017.

[Fun06] G. Fung, W. P. Backhaus, S. McDaniel, and M. Erdogmus, "To pig or not to pig: the marlin experience with stuck pig," *Proceedings of Offshore Technology Conference (OTC)*, Houston, Texas, USA, pp. 1-7, May 2006.

[Gai11] A.M. Gaikwad, G.L. Whiting, D.A. Steingart, and A.C. Arias, "Highly flexible, printed alkaline batteries based on mesh-embedded electrodes," *Adv. Mater.*, 23, pp. 3251-55, 2011.

[Gai13] A.M. Gaikwad, D.A. Steingart, T.N. Ng, D.E. Schwartz, and G.L. Whiting, "A Flexible High Potential Printed Battery for Powering Printed Electronics," *Appl. Phys. Lett.* 102, 233302, 2013.

[Ghe18] R.A. Gheorghiu and V. Iordache, "Use of Energy Efficient Sensor Networks to Enhance Dynamic Data Gathering Systems: A Comparative Study between Bluetooth and ZigBee," *Sensors* 18, 1801, Jun 2018.

[Gia07] Y.B. Gianchandani, O. Tabata, and H. Zappe, *Comprehensive Microsystems: Fundamentals, Technology, and Applications*, Elsevier, 3 volumes, 2100 pages, Nov. 2007.

[Gil05] K. Gilleo, *MEMS/MOEM Packaging: Concepts, Designs, Materials and Processes*, New York, NY, USA: McGraw Hill Professional, 2005.

[Har02] J.N. Harb, R.M. LaFollette, R.H. Selfridge, and L.L. Howell, "Microbatteries for self-sustained hybrid micropower supplies," *J. Power Sources*, 104(1), pp. 46-51, 2002.

[Hea08] M. Healy, T. Newe, and E. Lewis, "Wireless Sensor Node Hardware: A Review," *IEEE Sensors Conference*, pp.621-624, 2008.

[Hen98] D. Hensley, M. Milewits, and W. Zhang, "The Evolution of Oil Field Batteries*," Oil Field Review*, vol. 10, no. 3, pp. 42-57, Oct. 1998.

[Hsu00] T-R. Hsu, "Packaging Design of Microsystems and Meso-Scale Devices," *IEEE Transactions on Advanced Packaging*, vol. 23, no. 4, pp. 596-601, 2000.

[Hum01] P. Humble, J. Harb, and R. LaFollette, "Microscopic nickel-zinc batteries for use in autonomous microsystems," *J. Electrochemical Society*, 148(12), pp. A1357-1361, 2001.

[Huy09] B. Huyghe, J. Vanfleteren, and J. Doutreloigne, "Design of Flexible, Low-Power and Wireless Sensor Nodes for Human Posture Tracking Aiding Epileptic Seizure Detection," *IEEE Sensors Conference*, pp.1963-1966, 2009.

[Ino14] H. Inouea, S. Tomita, E. Higuchi, J. Tsai, and M. Chiku, "Construction of all-solid-state nickel-zinc rechargeable cell with hybrid hydrogel electrolyte," *ECS Transactions*, 61(27), pp. 229-235, 2014.

[ISM18] *ISM Band*, https://en.wikipedia.org/wiki/ISM_band, accessed on Apr. 1, 2018.

[Iwa05] C. Iwakura, H. Murakami, S. Nohara, N. Furukawa, and H. Inoue, "Charge–discharge characteristics of nickel/zinc battery with polymer hydrogel electrolyte," *J. Power Sources*, 152, pp. 291-4, 2005.

[Joh04] E. Johannessen, L. Wang, L. Cui, T. Tang, M. Ahmadian, A. Astaras, S.W. Reid, P.S. Yam, A.F. Murray, B.W. Flynn, S.P. Beaumont, D.R. Cumming, and J.M. Cooper, "Implementation of multichannel sensors for remote biomedical measurements in a microsystems format," *IEEE Trans. Biomed. Eng*., 51(3), pp. 525-535, 2004.

[Jun03] E. Jung, "Packaging Options for MEMS Devices," *MRS Bulletin*, Jan. 2003.

[Ken93] J. L. Kennedy, "Oil and Gas Pipeline Fundamentals," 2nd ed., *PennWell Books*, 1993.

[Kim15] J. Kimionis, M. Isakov, B. S. Koh, A. Georgiadis, and M. M. Tentzeris, “3D-Printed Origami Packaging with Inkjet-Printed Antennas for RF Harvesting Sensors,” *IEEE Transactions on Microwave Theory and Techniques*, Vol. 63, No. 12, Dec. 2015.

[Kli11] M. Kline, I. Izyumin, B. Boser, and S. Sanders, "Capacitive power transfer for contactless charging," *2011 Twenty-Sixth Annual IEEE Applied Power Electronics Conference and Exposition*, Fort Worth, TX, pp. 1398-1404, 2011.

[Koe97] P. Koeneman, I. Busch-Vishniac, and K. Wood, “Feasibility of micro power supplies for MEMS,” *IEEE/ASME J. Microelectromechanical Systems*, 6(4), pp. 355-362, 1997.

[Kup05] R.B. Kuprewicz, “Observations on the Application of Smart Pigging on Transmission Pipelines,” *OPS’s Inline Inspection Public Meeting,* Sep 2005.

[Kur68] H. Kurafuji and T. Masuzawa, "Micro-EDM of cemented carbide alloys," *Japan Society of Electrical-Machining Engineers*, vol. 2, no. 3, pp. 1-16, 1968.

[Lau10] J. H. Lau, C. K. Lee, C. S. Premachandran, and Y. Aibin, *Advanced MEMS Packaging*, New York, NY, USA: McGraw-Hill, 2010.

[Lee09] S-H. Lee, *Wafer-Level Packaging for Environment-Resistant Microsystems*, Ph.D. dissertation, Univ. Michigan, An Arbor, MI, USA, 2009.

[Lei14] W. Lei and L. Jing, “Compatible Hybrid 3D Printing of Metal and Nonmetal Inks for Direct Manufacture of End Functional Devices,” *SCIENCE CHINA Technological Sciences*, Vol. 57, No. 11, pp. 2089-2095, Nov 2014.

[Li13] T. Li, Q. Bai, and Y. B. Gianchandani, "High precision batch mode micro-electro-discharge machining of metal alloys using DRIE silicon as a cutting tool," *Journal of Micromechanics and Microengineering,* vol. 23, no. 9, p. 095026, 2013.

[Li17] T. Li, Y. B. Gianchandani, Y. Sui, and R. Meredith, *Environmental Logging System*, U.S. Patent 15, 410,724; issued July 20, 2017.

[Lia18] T. Liang, L. Shao, E. Yao, J. Zuo, X. Liu, B. Zhang, and F. Zhou, “Study on Fluid-Rock Interaction and Reuse of Flowback Fluid for Gel Fracturing in Desert Area,” *Geofluids*, 8948961, 9 pp., 2018.

[Lif14] V. A. Lifton, G. Lifton, and S. Simon, “Options for Additive Rapid Prototyping Methods (3D Printing) in MEMS Technology,” *Rapid Prototyping Journal*, Vol. 20, 5, pp. 403-412, 2014.

[Lin15] B. Ray, “ZigBee vs. Bluetooth: A Use Case with Range Calculations,” *LinkLabs Blog*, Aug. 2015.

[Lip13] H. Lipson, M. Kurman, *Fabricated: The New World of 3D Printing*, John Wiley & Sons, Hoboken, NJ, USA, 2013.

[Liu12] Z. Liu and Y. Kleiner, “State-of-the-Art Review of Technologies for Pipe Structural Health Monitoring,” *IEEE Sensors Journal*, 12, pp. 1987-92, 2012.

[Lop12] A. J. Lopes, E. MacDonald, and R. B. Wicker, “Integrating Stereolithography and Direct Print Technologies for 3D Structural Electronics Fabrication,” *Rapid Prototyping Journal*, Vol. 18, No. 2, pp. 129-143, 2012.

[Lu16] X. Lu, P. Wang, D. Niyato, D. I. Kim, and Z. Han, “Wireless Charging Technologies: Fundamentals, Standards, and Network Applications,” *IEEE Communications Surveys & Tutorials*, Vol. 18, No. 2, Second Quarter 2016.

[Ma15] Y. Ma, Y. Sui, T. Li, and Y. B. Gianchandani, “A Submillimeter Package for Microsystems in High-Pressure and High-Salinity Downhole Environments,” *Journal of Microelectromechanical Systems*, Vol. 24, No. 4, Aug 2015.

[Ma16] Y. Ma, *Packaging Technologies for Millimeter Scale Microsystems in Harsh Environment Applications*, Ph.D. dissertation, Univ. Michigan, An Arbor, MI, USA, 2016.

[Mar15] C. Marchand, “How to Prevent Leakage or Environmental Damage,” *International Electrotechnical Commission News*, May 2015.

[Mas90] T. Masaki, K. Kawata, and T. Masuzawa, "Micro electro-discharge machining and its applications," *Proc. IEEE Micro Electromechanical Systems: An Investigation of Microstructures, Sensors, Actuators, Machines and Robots*, Napa Valley, CA, Feb. 1990, pp. 21-26.

[Naj03] Khalil Najafi, "Micropackaging Technologies for Integrated Microsystems: Applications to MEMS and MOEMS," Proc. SPIE 4979, *Micromachining and Microfabrication Process Technology VIII*, 15 Jan 2003.

[Nat05] M. Nathan, D. Golodnitsky, V. Yufit, E. Strauss, T. Ripenbein, I. Shechtman, S. Menki, and E. Peled, “Three-Dimensional Thin-Film Li-Ion Microbatteries for Autonomous MEMS,” *Journal of Microelectromechanical Systems*, Vol. 14, No. 5, pp 879-885, Oct 2005.

[Ope13] *Smartball Flowable Pressure and Temperature Micro-recorder*, Openfield Technology, Versailles, France, 2013.

[Ota16] H. Ota, S. Emaminejad *et al.*, “Application of 3D Printing for Smart Objects with Embedded Electronic Sensors and Systems,” *Adv. Mater. Technol.*,1, 1600013, 2016.

[Par17] J. F. Parker, C. N. Chervin, I. R. Pala, M. Machler, M. F. Burz, J. W. Long, and D. R. Rolison, “Rechargeable Nickel–3D Zinc Batteries: An Energy-Dense, Safer Alternative to Lithium-Ion,” *Science* 356, pp 415–418, April 2017.

[Pik13] J.H. Pikul, P.V. Braun, and W.P. King, “High Power Primary Lithium Ion Microbatteries,” *J. Phys.: Conf. Ser.* 476, 012087, 2013.

[Pir14] P. Pirzadeh, K.L. Lesage, and R.A. Marriott, "Hydraulic Fracturing Additives and the Delayed Onset of Hydrogen Sulfide in Shale Gas," *Energy Fuels* 28, pp. 4993-5001, 2014.

[Ras20] *Raspberry Pi 3 Model B*, https://www.raspberrypi.org/products/raspberry-pi-3-model-b/, accessed on Jul. 17, 2020.

[Ray15] B. Ray, "A Bluetooth & ZigBee Comparison for IoT Applications," *LinkLabs,* Oct. 2015.

[Rob97] A.D. Robertson, A.R. West, and A.G. Ritchie, "Review of Crystalline Lithium-ion Conductors Suitable for High Temperature Battery Applications," *Solid State Ionics*, vol. 104, no. 1, pp. 1-11, Dec. 1997.

[Roe13] M. G. L. Roes, J. L. Duarte, M. A. M. Hendrix, and E. A. Lomonova, "Acoustic Energy Transfer: A Review," *IEEE Transactions on Industrial Electronics*, Vol. 60, No. 1, Jan 2013.

[Roy03] K. Roy, S. Mukhopadhyaym, H. Mahmoodi-Meimand, "Leakage Current Mechanisms and Leakage Reduction Techniques in Deep-submicrometer CMOS Circuits," *Proceedings of the IEEE*, vol. 91, no. 2, pp. 305-327, Feb. 2003.

[Sad14] A. M. Sadeghioon, N. Metje, D. N. Chapman, and C. J. Anthony, "Smart Pipes: Smart Wireless Sensor Networks for Leak Detection in Water Pipelines," *J. Sens. Actuator Netw.,* 3, pp. 64-78, 2014.

[Sat08] H. Sato, C. Berry, B. Casey, G. Lavella, Y. Yao, J. V. Brooks, and M. Maharbiz, "A cyborg beetle: Insect flight control through an implantable, tetherless microsystem," *IEEE Intl. Conf. Micro Electro Mechanical Systems*, pp. 164-7, 2008.

[Sei14] *Micro Battery Product Catalogue*, Seiko Instruments Inc., Chiba, Japan, 2014.

[Ser15] H. R. Seren, X. Zhao, C. Chen, C. Wang, and X. Zhang, "Enabling a Microfluidic RFID Readout System via Miniaturization and Integration," *Journal of Microelectromechanical Systems*, vol. 24, no. 2, pp. 395-403, Apr. 2015.

[She14] S. Sherrit, H. Lee, P. Walkemeyer, J. Hasenoehrl, J. Hall, T. Colonius, L. Tosi, A. Arrazola, N. Kim, K. Sun, and G. Corbett, "Flow Energy Piezoelectric Bimorph Nozzle Harvester," *Proceedings of the SPIE*, vol. 9057, Apr. 2014.

[She16] C. Shen, Y. Guo, H. M. Oubei, T. K. Ng *et al.*, "20-Meter Underwater Wireless Optical Communication Link with 1.5 Gbps Data Rate," *Optics Express*, Vol. 24, No. 22, 2016.

[Shi15] Z. Shi, Y. Chen, M. Yu, S. Zhou, N. Al-Khanferi, "Development and Field Evaluation of a Distributed Microchip Downhole Measurement System," *SPE Digital Energy Conference and Exhibition*, The Woodlands, Texas, Mar. 2015.

[Sil11] *C8051F99x-C8051F98x Datasheet*, Silicon Laboratories, Austin, Texas, 2011.

[Sil19] *BGM121/BGM123 Blue Gecko Bluetooth SiP Module Datasheet*, Silicon Laboratories, Austin, Texas, 2019.

[Sin98] D. Singh, “Characteristics and Effects of γ-NiOOH on Cell Performance and a Method to Quantify It in Nickel Electrodes,” *J. Electrochemical Society*, 145 (1), 1998.

[Stm14] *LSM303C Datasheet*, STMicroelectronics, Jun. 2014.

[Sui17] Y. Sui, *Low Power Autonomous Microsystem for Oil Well Logging Applications*, Ph.D. dissertation, Univ. Michigan, An Arbor, MI, USA, 2017.

[Sun13] K. Sun, T. Wei, B. Y. Ahn, J. Y. Seo, S. J. Dillon, and J. A. Lewis, “3D Printing of Interdigitated Li-Ion Microbattery Architectures,” *Adv. Mater.*, 25, pp 4539–4543, 2013.

[Tad18] *Tadiran Lithium Batteries Product Catalogue*, Tadiran Batteries, Germany, 2018.

[Tak02] K. Takahata and Y. B. Gianchandani, "Batch mode micro-electro-discharge machining," *IEEE/ASME J. Microelectromechanical Systems*, vol. 11, no. 2, pp. 102-110, 2002.

[Tre01] C. J. Trench, “How Pipelines Make the Oil Market Work –Their Networks, Operation and Regulation,” *Memorandum for Association of Oil Pipelines and American Petroleum Institute's Pipeline Committee*, Dec. 2001.

[Tum01] R. R. Tummala, *Fundamentals of Microsystems Packaging*, McGraw-Hill: New York, 2001.

[Vel17] N. Vellaluru, Y.B. Gianchandani, and T. Li, “Facile Batch Mode Process for High Capacity Rechargeable Nickel-Zinc Microbatteries,” *IEEE International Conference on Solid State Sensors, Actuators, and Microsystem (Transducers)*, Kaohsiung, Taiwan, Jun. 2017, 4 pp.

[War01] B. Warneke, M. Last, B. Liebowitz, and K. S. J. Pister, "Smart Dust: communicating with a cubic-millimeter computer," *Computer*, Vol. 34, No. 1, pp. 44-51, 2001.

[Wat12] J. Watson and G. Castro, “High-temperature Electronics Pose Design and Reliability Challenges,” *Analog Dialogue*, Vol. 46, Apr. 2012.

[WiF15] *Wi-Fi*, https://en.wikipedia.org/wiki/Wi-Fi, last accessed on Nov. 28, 2015.

[Wis09] K. D. Wise, "Wireless integrated microsystems: Wearable and implantable devices for improved health care," *International Conference on Solid-State Sensors, Actuators and Microsystems (Transducers)*, Denver, CO, pp. 1-8, 2009.

[Wod11] S. Wodin-Schwartz, M.W. Chan, K.R. Mansukhani, A.P. Pisano, and D.G. Senesky, “MEMS sensors for down-hole monitoring of geothermal energy systems,” in *Proceedings of the ASME 2011 5th International Conference on Energy Sustainability*, Washington, DC, USA, 2011.

[Wu15] S-Y. Wu, C. Yang, W. Hsu, and L. Lin, "3D-Printed Microelectronics for Integrated Circuitry and Passive Wireless Sensors," *Microsystems & Nanoengineering*, 1, 2015013, 2015.

[Yan13] J. Yang, "A Harsh Environment Wireless Pressure Sensing Solution Utilizing High Temperature Electronics," *Sensors*, vol. 13, no. 3, pp. 2719-2734, Mar. 2013.

[Yu12] M. Yu, S. He, Y. Chen, N. Takach, P. LoPresti, S. Zhou, and N. Al-Khanferi, "A Distributed Microchip System for Subsurface Measurement," *SPE Annual Technical Conference and Exhibition*, San Antonio, Texas, Oct. 2012.

[Zho17] N. Zhou, C. Liu, J.A. Lewis, and D. Ham, "Gigahertz Electromagnetic Structures via Direct Ink Writing for Radio-Frequency Oscillator and Transmitter Applications," *Adv. Mater.*, 29, 15, 2017.

[Zig15] *ZigBee*, https://en.wikipedia.org/wiki/ZigBee, last accessed on Nov. 28, 2015.